Methodology for the Design and Predictive Control of Active Solar Windows with Radiant Floor Heating in Perimeter Zones

John Hill

A Thesis

in

The Department

of

Building, Civil and Environmental Engineering

Presented in Partial Fulfillment of the Requirements

for the Degree of Master of Applied Science (Building Engineering) at

Concordia University

Montreal, Quebec, Canada

June 2023

CONCORDIA UNIVERSITY

School of Graduate Studies

This is to certify that the thesis is prepared

By: John Hill

Entitled: Methodology for the Design and Predictive Control of Active Solar Windows with Radiant Floor Heating in Perimeter Zones

and submitted in partial fulfillment of the requirements for the degree of

Master of Applied Science (Building Engineering)

complies with the regulations of the University and meets the accepted standards with respect to originality and quality.

Signed by the final Examining Committee:

_____ Chair

Dr. Hua Ge

_____ Examiner

Dr. Hua Ge

_____ Examiner

Dr. Leon Wang

_____ Supervisor

Dr. Andreas Athienitis

Approved by: _____

Dr. Mazdak Nik-Bakht, Graduate Program Director

Department of Building, Civil and Environmental Engineering

July 3rd, 2023 _____

Dr. Mourad Debbabi, Dean

Gina Cody School of Engineering and Computer Science

Abstract

Methodology for the Design and Predictive Control of Active Solar Windows with Radiant Floor Heating in Perimeter Zones

John Hill

This study presents a model for designing and controlling energy-positive facades with radiant floor heating in perimeter zones of commercial buildings. The model integrates bifacial semi-transparent photovoltaic windows, motorized venetian blinds, and hydronic radiant floor heating systems. These components are modeled to optimize energy performance within occupant comfort constraints during the heating season. By implementing near-optimal control strategies for room air temperature setpoints, blind tilt angles, and controlled lighting loads, the perimeter zones achieve improved energy flexibility, efficiency, and thermal and visual comfort. Key design variables such as slab thickness, window-to-wall ratio, and packing factor were analyzed parametrically to determine optimal ranges when subjected to near-optimal control strategies. To evaluate the effectiveness of different control strategies, a specially designed and instrumented test-room at the Future Buildings' Lab (FBL) was used as a case study. Balancing energy performance with occupant comfort is crucial, as prioritizing one aspect may compromise the other. The combined control of these systems demonstrates enhancements in both energy performance and occupant comfort across various design scenarios. By implementing near-optimal control of the room air setpoint and the blind tilt angle the heating efficiency can improve by 39.6%, the BEFIP was 94.8% and 96.8% in the morning and evening peak periods, all while maintaining occupant comfort on a cloudy and mild day in the heating season. The addition of active solar windows further improves the energy flexibility of the zone. Similarly, in limiting

weather conditions, such as very cold and cloudy days, the system may achieve significant energy flexibility, reduce energy costs, while maintaining thermal comfort.

Acknowledgements

I extend my gratitude to Dr. Andreas Athienitis, my supervisor, for his invaluable guidance and patience. I am truly grateful for the way he challenged me to enhance my skills, resulting in my growth as an engineer. Through his mentorship, I had the opportunity to work on a complex engineering project that not only expanded my knowledge but also sparked new academic interests.

I would also like to express my appreciation to Michael Kim for thoroughly reviewing my thesis and to Gilbert Larochelle-Martin for providing continuous guidance throughout my degree. In the lab, I extend my thanks to Jiwu Rao, Daniel Baril, and Cheng Mian Ma for their assistance in facilitating equipment installation, conducting experimental procedures, and setting up sensors.

I am sincerely grateful for the technical and financial support extended by the NSERC/Hydro Quebec Industrial Research Chair and the Faculty of Engineering at Concordia University.

My journey towards completing this degree would not have been possible without the help and guidance of my fellow students in the CZEBS office. Therefore, I would like to acknowledge the support of Andrea Petrucci, Anna-Maria Sigounis, Anthony Maturo, Emil Jalilov, Erin Gaucher-Loksts, Harry Vallianos, J.C. Pelletier De-Koninck, Kai Ye, Masoud Valinejad, Matin Abtahi, and Navid Morovat.

Despite not having had the opportunity to meet in person, I express my gratitude to Stratos Rounis for taking the time to meet with me online during the initial stages of my degree, helping me navigate the transition into academia. Furthermore, I would like to thank Ali Saberi, another former student of Dr. Athienitis, for assisting me during the preliminary design phase of installing the hydronic radiant floor in the Future Building's Lab.

Lastly, I would like to extend my heartfelt thanks to my parents, Caroline and Todd, my brother James, and my girlfriend Aryn, for their unwavering support and endless patience throughout my academic journey.

Table of Contents

List of Figures

List of Tables

Nomenclature

Acronyms

GHG – Greenhouse Gas

CO_2 – Carbon Dioxide

STPV – Semi-transparent Photovoltaic

MVB – Motorized Venetian Blinds

HRFH – Hydronic Radiant Floor Heating

TES – Thermal Energy Storage

BIPV – Building Integrated Photovoltaic

PEX – Crosslinked Polyethylene

DSM – Demand Side Management

RC – Resistance-Capacitance

db – Dead-band

PPD – Predicted Percent Dissatisfied

UDI – Useful Daylight Index

DGP –Daylight Glare Probability

ABE –Active Building Envelope

RBC –Rule Based Control

CO – Cut-Off Control

PF – Packing Factor

WWR – Window-to-wall Ratio

FBL – Future Building's Lab

NZEB – Net-zero Energy Building

TABS – Thermally Activated Building System

BEFI(P) – Building Energy Flexibility Index

IGU – Insulated Glazing Unit

DG – Double Glazed

TG – Triple Glazed

QG – Quadruple Glazed

PMV – Predicted Mean Vote

IEQ – Interior Environmental Quality

GP – Glare Potential

DGI –Daylight Glare Index

FDM –Finite Difference Method

MPC –Model Predictive Control

AO – Aways Open Control

ASHRAE – American Society of Heating Refrigeration and Air Conditioning Engineers

HVAC –Heating Ventilation & Air Conditioning

IESNA – Illuminating Engineering Society of North America

General Symbols

A – Area

Q – Energy

C_p – Specific heat

V – Velocity

L – Length (or thickness)

H – Height

W – Width

D – Depth

t – Time

T – Temperature

P – Power

μ – Temperature Coefficient

dc – Distance between cell

σ – Stefan-Boltzmann Constant

Nu – Nusselt Number

Ra – Rayleigh Number

p – Pressure

E – Illuminance

Vol – Volume

$\dot{m}$ – Mass flow rate

q – Heating source

R – Resistance

C – Capacitance

U – Conductance

Δt – Timestep

Dt – Duration

S – Solar Radiation

η – Efficiency

Kp – Proportional Control Constant

Bi – Biot Number

ch – Cell Height

cw – Cell Width

h – Heat Transfer Coefficient

k – Thermal Conductivity

ach – Air changes per hour

M – Exitance

Solar Geometry, Blind Angles, & Optical Properties

n – Day of year

α – Solar Altitude Angle

φ – Solar Azimuth Angle

θ – Incidence Angle

β – Tilt angle

d – Profile Angle

γ – Surface Solar Azimuth Angle

δ –declination angle

τ – Transmittance

ε – Emissivity

ρ – Reflectance

α – Absorptance

Subscripts

i – Node 'i'

j – Node 'j'

p – Point in space, timestep

op – Operative

mr – Mean Radiant

pr – Plane Radiant

ref – Reference Case

flex – Flexibility Case

case – Control Case

f – Floor

c – Convective

r – Radiative

win – window

cav – Cavity

int – Interior

ext – Exterior

PV – Photovoltaic

cell – Photovoltaic Cell

fac – Façade

inter – Interreflections

inf – Infiltration

solar – Solar Radiation

supply – Supply Temperature

return – Return Temperature

front – Solar Radiation on front of PV cell

back – Solar Radiation on back of PV cell

A – Aspect Ratio

m – Mean

g – Glazing

cond –conduction

tot – Total

mod – modules

clr – Clear Day

P, mp – Max Power Point

cld – Cloudy Day

vis – Visible Spectrum

wp – Workplane

sp – Setpoint

opt – Optimal

NO – Near Optimal

aux – Auxiliary

max – Maximum

art – Artificial

dim – Dimming Level

suff – Sufficient

wd – Workday

dl – Daylight

Occupant Comfort

$F_{i,j}$ – View Factor

$c_{p,j}$ – Configuration Factor

M – Metabolic Energy Production

I_{cl} – Clothing Insulation

R^{-1} – Radiosity Matrix

L –Thermal Load on the Body

ω –solid angle: glare source

γ –solid angle

L –Luminance

P –Position Index

Chapter 1: Introduction

1.1. Motivation

The building sector is a major contributor to climate change, due to the high energy demands necessary for maintaining occupant comfort. Globally, nearly 30% of greenhouse gas (GHG) emissions are due to buildings (GlobalABC et al., 2019), with 12% of emissions originating from the building sector in Quebec (Statistics Canada, 2022). Transitioning towards a net-zero future will help to reduce the share of GHG emissions from buildings on both a local and global scale. In Quebec, the largest share of energy consumption for commercial and institutional buildings results from space heating (47%) and lighting (17%; Whitmore & Pineau, 2021). Moreover, 80% of Quebec households use electric heating (Hydro Quebec, 2019), which places significant stress on the electric grid to meet peak demand requirements (Athienitis et al., 2020). On January 21st, 2022, Quebec recorded its highest peak demand at 40,300 MW. This is potentially problematic because more buildings are becoming electrified, and therefore, more capacity will be needed to meet winter peak demands (see Figure 1.1).

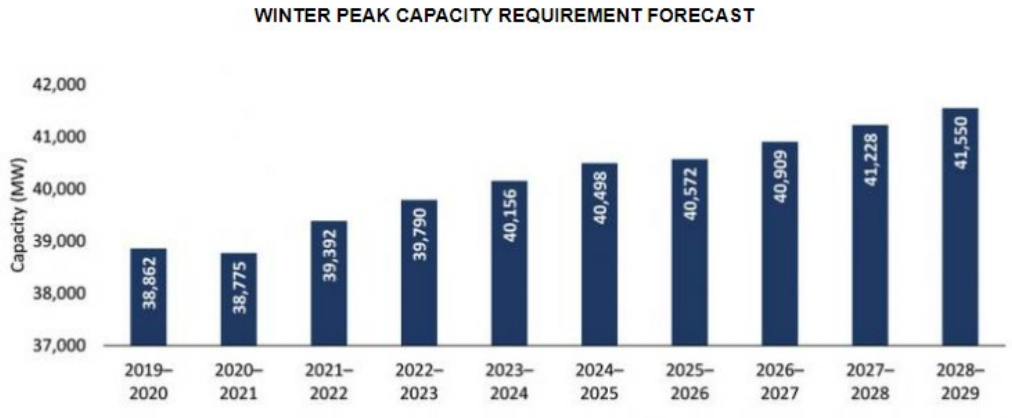

Figure 1.1. Quebec's Forecasted Winter Peak Demand Requirement. (Hydro Quebec, 2020).

Typically, to create more capacity to handle these excess energy demands, utility companies will either develop new power plants, or run older power plants, which is worse for the environment because they depend on the use of fossil fuels (Government of Quebec, 2020). Another option to alleviate stress on the grid is to create energy flexibility of building demands. Energy flexibility can be defined as the ability of a building (or zone) to increase or decrease its electricity demand, for a specified period, when needed for the grid (Athienitis et al., 2020). This results in shifting energy demands away from peak demand periods for the grid. During the heating season in Quebec, these peak demand periods occur between 6-9AM and 4-8PM. Energy flexibility can be achieved through proper design of the building envelope and through predictive control of its integrated systems.

1.2. Perimeter Zones in Commercial Net Zero Energy Building's

Net-Zero Energy Buildings

There are several definitions of a net-zero energy building (NZEB), but the prefix 'net' suggests that there is a balance between energy demand and supply (Athienitis & O'Brien, 2015). Depending on the goals of a project, different weightings are used, such as energy (kWh), greenhouse gas emissions (CO_2), or cost ($; Deng et al., 2014). Figure 1.2. is a graphical representation of a NZEB based on different weighting criteria.

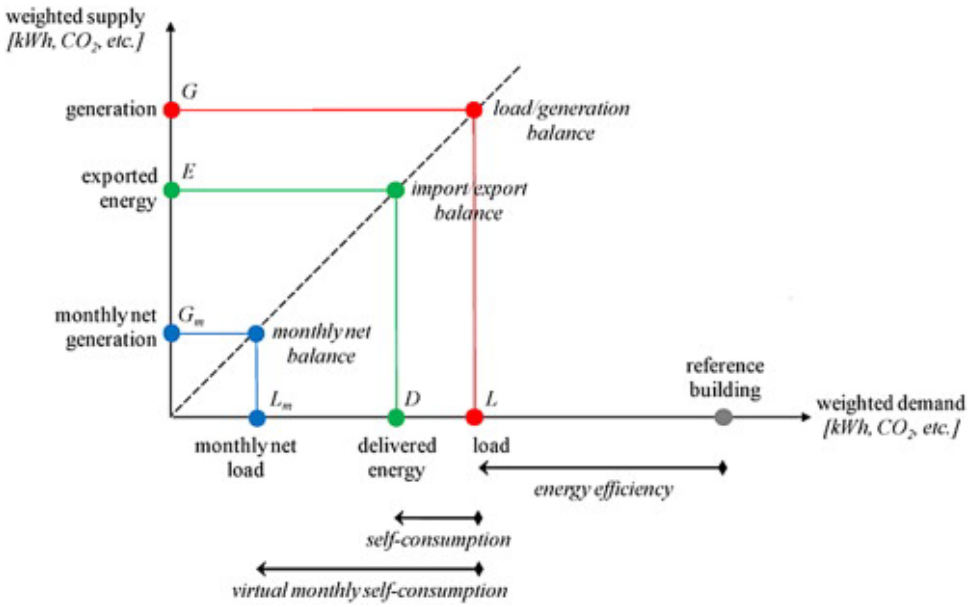

Figure 1.2. Graphical Representation of Net-Zero Energy Building (Sartori et al., 2012).

This thesis defines net-zero energy buildings as a those that consume at least as much energy as they generate for themselves, or for the electric grid, on a monthly or annual basis (Sartori et al., 2012). These buildings may not achieve a net zero standing in each given year due to the nature of weather, building condition, and operation, but they can be considered near net-zero in these cases (Pless & Torcellini, 2010). For buildings to operate at net-zero or near net-zero, correct decisions must be made at the preliminary design stage for the building. For example, passive building design aims to minimize energy demands during a buildings lifetime without the use of integrated mechanical systems. If sound passive design is achieved, then the building will rely less on implemented HVAC and lighting systems. This allows integrated renewable energy systems to neutralize the energy loads of the building.

Perimeter Zones

Commercial buildings are commonly divided into two types of zones; perimeter and core (Lim et al., 2022). Perimeter zones are exposed to the exterior environment through windows and are typically defined by an interior depth of up to 4.5 m (15 ft.) from the façade (LANL, 2002). There

are several critical considerations associated with perimeter zones such as the benefits of: passive heating with solar gains, reduced lighting loads from daylighting, and providing views to the exterior of the building. Conversely, perimeter zones have several risks associated with them: overheating and glare due to excessive solar gains and daylight, increased heat losses through windows potentially increasing heating demands in the winters (Chaloeytoy et al., 2019; Moe, 2010). Many common design techniques and approaches may be used for realizing a net-zero target and minimizing the risks associated with perimeter thermal zones (Kolokotsa et al., 2011):

- Passive design techniques.
- Use of renewable energy systems.
- Innovative shading devices.
- Efficient heating systems (e.g., thermally activated building systems)

Among the techniques listed, this thesis investigates the design aspects associated with the perimeter zone (e.g., building orientation, window-to-wall ratio, thermal mass), renewable energy systems (e.g., bifacial semi-transparent photovoltaic windows), shading devices (e.g., motorized venetian blinds), and thermally activated building systems (e.g., hydronic radiant floor heating).

1.3. Objectives

1. This thesis will develop a model for designing and controlling energy-positive façades with radiant floor heating for perimeter zones in commercial buildings, with the goal of optimizing energy flexibility and efficiency within thermal and visual comfort constraints during the heating season. Systems included in the model will be bifacial semi-transparent photovoltaic (STPV) windows, motorized venetian blinds (MVB), and hydronic radiant floor heating (HRFH).

2. We will examine near-optimal control strategies for the blind tilt angle (β_{opt}) of the MVB, temperature setpoint strategies (T_{sp}) of the zone air temperature, and dimming percentages of the artificial luminaires, based on different environmental conditions (i.e., clearness, exterior temperature). A parametric analysis of key design variables for these systems including slab thickness of the HRFH (L_{slab}), window-to-wall ratio ($WWR \equiv A_{win}/A_{fac}$), and packing factor ($PF \equiv A_{PV}/A_{win}$), will determine their optimal ranges when subjected to near-optimal control strategies (see Figure 1.3). Key performance indicators such as energy flexibility, energy efficiency, thermal comfort, and visual comfort will be used to identify when near-optimal design and control has been achieved. The presented model will be validated with experiments at an outdoor test facility in Montreal, Quebec (Future Building's Lab, FBL).

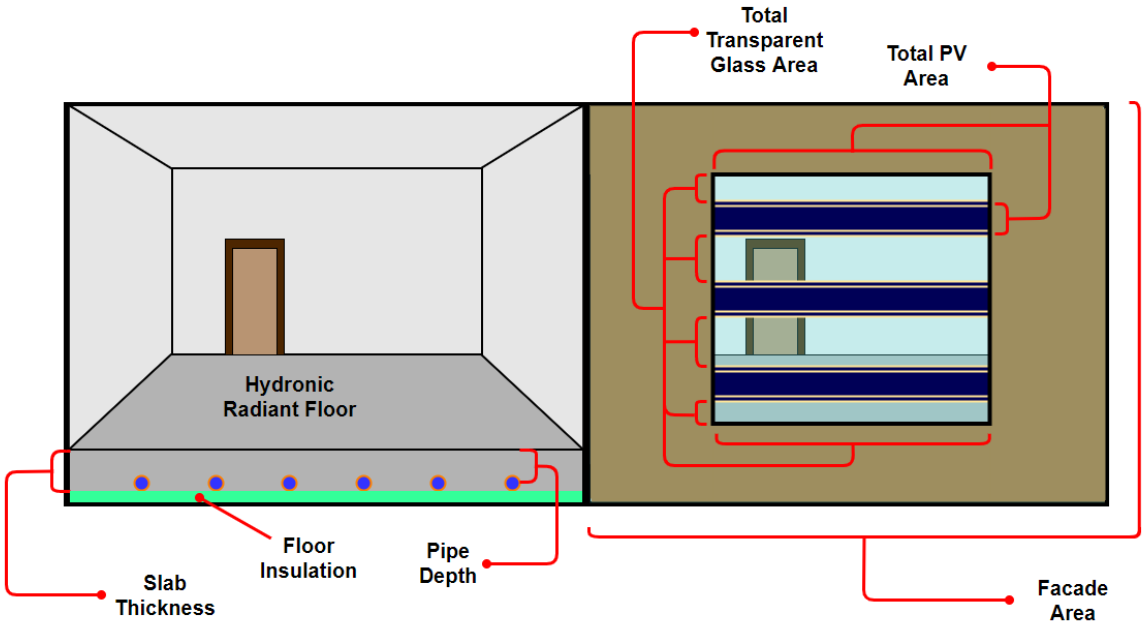

Figure 1.3. Schematic of Perimeter zones and key design variables.

1.4. Outline

Chapter 1: *Introduction* – This chapter establishes the motivation, background information, and objectives of this research study.

Chapter 2: *Literature Review* – A chapter to review the relevant literature for the design and control of perimeter zones in net-zero energy buildings, building integrated systems such as semi-transparent photovoltaic windows, motorized shading, thermally activated building systems, and key performance indicators for energy efficiency, energy flexibility, thermal comfort, and visual comfort.

Chapter 3: *Methodology & Experimental Case Study* – A detailed chapter to introduce the perimeter thermal zone case study in Montreal, Quebec, and the modelling approaches used in this model. The zone is modelled with an RC thermal network and simulations are completed with the finite difference method to calculate temperature profiles and heating demands. Daylighting analysis is completed with the radiosity method. The experimental setup is detailed and includes the measurement methods for calculating the energy performance and occupant comfort results associated with the zone.

Chapter 4: *Experimental Results & Discussion* – This chapter presents the experimental and results obtained from the perimeter thermal zone case study and the verification with the simulation model developed.

Chapter 5: *Conclusions & Future Research Needs* – Key conclusions from this research study are summarized, modelling and experimental limitations are discussed, the future research needed, and the contributions of this study.

Chapter 2: Literature Review

2.1. Key Performance Indicators in Net Zero Perimeter Zones

High performing buildings must meet specific energy performance criterion while maintaining a suitable environment for its occupants. The energy performance indicators that will be addressed in this study include energy efficiency and energy flexibility, while the occupant comfort performance indicators include thermal and visual comfort. These performance indicators will be discussed in detail below.

2.1.1. Energy Efficiency

We can reduce the overall energy loads of buildings with passive design techniques, integration of renewable energy systems, and proper design and control of shading and heating systems. Windows have the highest heat penetration for buildings, and high glazing areas are typical in office buildings. Although this design aspect can help to reduce heating loads with solar gains, it simultaneously increases the risk of overheating, even during the heating season in cold climates (Brideau et al. 2015; Grynning et al. 2014). Therefore, when relying on high glazing areas to reduce heating demands in winter, controlling the admission of solar gains with optimal temperature setpoint strategies should be adopted to avoid overheating (van Moeseke et al., 2007).

Similarly, high glazing areas allow increased daylighting which reduces electric lighting loads. However, net energy consumption may increase with higher window-to-wall ratios (WWR) as the decrease in electric lighting may not compensate for the increase in cooling demand due to excessive solar gains (Dubois & Flodberg, 2013). Poirazis et al. (2008) completed a simulation study on different WWRs for a single-skin glazed office building and found that 100% glazing areas achieved a 15% increase in annual energy demand compared to WWRs of 30%, due to

increased cooling demands. Furthermore, greater WWRs increase the potential for glare, leading to visual discomfort (Dubois & Flodberg, 2013).

Integrating renewable energy systems into buildings for electrification is another method for improving energy efficiency (Athienitis et al., 2020; Bambara et al., 2021), over and above passive design techniques. Increasing the electricity demand in high-performing buildings increases pressure on the electrical grid to meet the demands of the population, specifically during peak demand periods. Therefore, while targeting energy efficiency, a simultaneous objective of improving energy flexibility must be considered for new and existing buildings.

2.1.2. Energy Flexibility

Energy flexibility can be defined as a building's ability to adjust its energy supply or demand, when needed for the electrical grid. Improved energy flexibility can be achieved through many approaches and technologies (Athienitis et al., 2020); described below are the technologies or techniques relevant to this study:

1. Passive thermal mass of the building.
2. Modification of zone setpoints.
3. Thermally activated building systems (TABS, e.g., hydronic radiant floor heating).
4. Heat pumps.
5. On-site renewable energy, e.g., semi-transparent photovoltaic windows.
6. Controlled lighting loads.

Energy flexibility can be quantified by a dynamic index called the Building Energy Flexibility Index (BEFI; Athienitis et al.,2020). This index calculates how much average power over a specified period can be increased or decreased, when compared to a reference energy consumption

profile. Shown below in equation (2.1) and (2.2) is the BEFI (W) and BEFIP (%) which normalizes the BEFI:

$$\overline{\mathrm{BEFI}}(t, Dt) = \frac{\int_t^{t+Dt} P_{ref} dt - \int_t^{t+Dt} P_{flex} dt}{Dt} \tag{2.1}$$

$$\overline{\mathrm{BEFIP}}(t, Dt) = \frac{\int_t^{t+Dt} P_{ref} dt - \int_t^{t+Dt} P_{flex} dt}{\int_t^{t+Dt} P_{ref} dt} \tag{2.2}$$

Pref is the power consumption of a reference profile case, *Pflex* is the power consumption for a flexible case, *t* is the starting time of flexibility, and *Dt* is the duration of the flexibility. Shown below in Figure 2.1 are the two peak demand periods for a typical winter day in Quebec, which occur from 6-9AM and 4-8PM (Hydro Quebec, 2019).

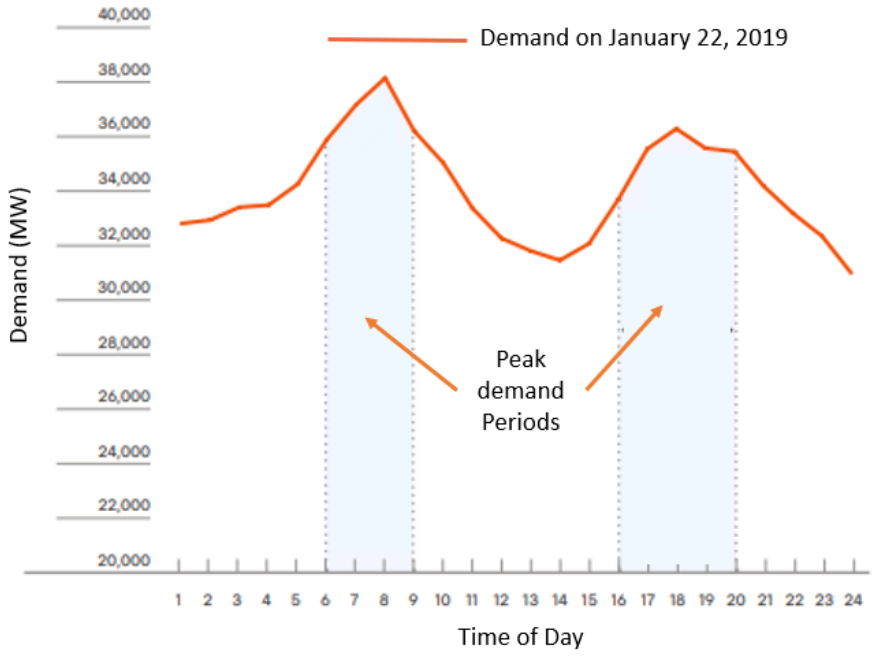

Figure 2.1. Peak demand periods on a winter day in Quebec (Hydro Quebec, 2019).

Given that humans spend upwards of 90% of their lifetime inside buildings (ASHRAE, 2010a), careful consideration must be taken when developing near-optimal control strategies to maintain occupant comfort. Studies indicate that discomfort from indoor environmental quality (IEQ) may lead to a decrease in work performance (Guili et al., 2012; EPA, 2000). Therefore, when targeting increased energy performance, it is important not to concede occupant comfort and health.

2.1.3. Thermal Comfort

Thermal comfort is defined as a "condition of the mind which expresses satisfaction with the thermal environment" (ASHRAE, 2010a, pg.4; Fanger, 1988, pg. 3057). There is a difficulty in providing thermal comfort for all occupants as individual preferences are present. One main approach to assessing thermal comfort is the Predicted Mean Vote (PMV) index which considers six factors. These factors include air and mean radiant temperature, humidity, and air velocity, as well as clothing insulation and physical activity of a person. See Figure (2.2) for a schematic of the factors affecting thermal comfort.

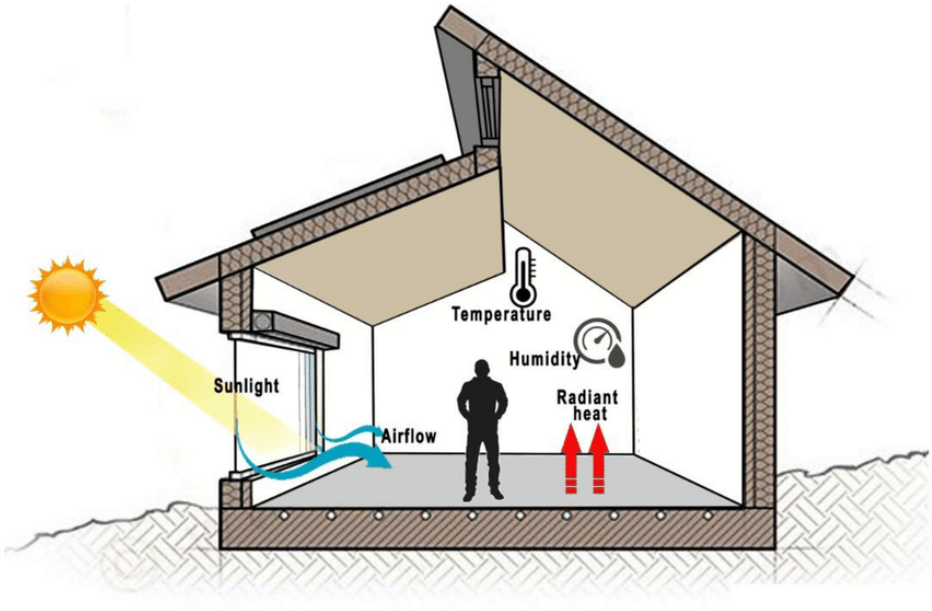

Figure. 2.2. Factors affecting Thermal Comfort. (Vijayan et al., 2022)

Thermal Comfort Evaluation

The PMV index is a 7-point thermal sensation scale ranging from hot to cold (ISO-7730, 2005). Table 2.1 below shows the 7-point PMV scale, and the corresponding equation (2.3) calculates the PMV index. *M* is the rate of metabolic energy production (W/m^2), and *L* is the thermal load on the body which is the difference between internal heat production and heat loss to the environment based on skin temperature and sweat rate due to the activity level (ASHRAE, 2017).

$$\mathrm{PMV} = (0.303 \cdot \exp(-0.036 \cdot \mathrm{M}) + 0.028) \cdot \mathrm{L} \qquad (2.3)$$

Table 2.1. 7-point PMV scale

Scale	Thermal Perception
+3	Hot
+2	Warm
+1	Slightly Warm
0	Neutral
-1	Slightly Cool
-2	Cool
-3	Cold

Literature states that a comfortable environment should be within the range of PMV = ± 0.5 (ASHRAE, 2010a; Fanger, 1988), but for the purposes of this study, a range of PMV = ± 1 is considered satisfactory. This thermal comfort range was extended to allow increased freedom to improve energy performance. The Predicted Percentage of Dissatisfied (PPD) is determined by the PMV index to express those feeling discomfort in certain thermal conditions. To compensate for individual differences, a minimum of 5% dissatisfied is accounted for by the equation. The equation for PPD (2.4) and the relation of PMV with PPD is shown in Figure (2.3):

$$\mathrm{PPD} = 100 - 95 \cdot \exp\left(-0.03353 \cdot \mathrm{PMV}^4 - 0.2179 \cdot \mathrm{PMV}^2\right) \qquad (2.4)$$

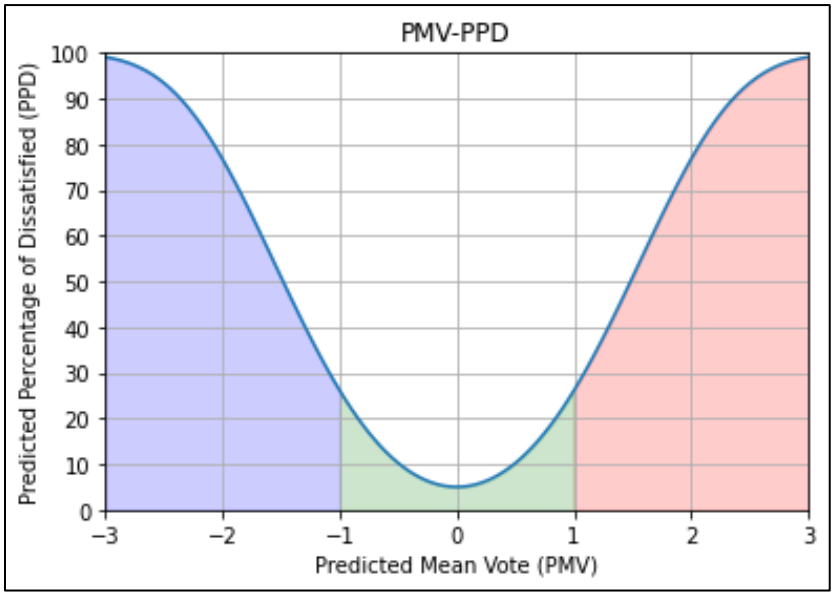

Figure 2.3. PMV-PPD scale.

Another variable in determining if an enclosure is thermally comfortable is the operative temperature, which is the average between the air temperature and the mean radiant temperature, weighted by their respective heat transfer coefficients, h_c and h_r. The method for determining thermal comfort with the operative temperature will be described in chapter 3.

$$\mathrm{T_{op}} = \frac{\mathrm{T_a} \cdot \mathrm{h_c} + \mathrm{T_{mr}} \cdot \mathrm{h_r}}{\mathrm{h_c} + \mathrm{h_r}} \qquad (2.5)$$

Beyond thermal discomfort from transmitted solar gains, transmitted daylight may also cause occupant discomfort due to glare. Another factor affecting visual comfort is providing an acceptable view to the outdoors. Therefore, building designs must strike a balance of WWR to minimize predicted glare and produce an acceptable connection to the exterior environment.

2.1.4. Visual Comfort

When visual discomfort arises, several symptoms may be associated: headaches, migraines, sore eyes, and gastrointestinal problems, among others (IESNA, 2000). There are several aspects of lighting that can cause visual discomfort, but for the purpose of this study, glare due to windows will be the focus. Glare can occur in two ways; the first is when there is too much illuminance and the second is when the range of luminance is too large in a visual environment. Discomfort glare is important for interior applications and is a feeling of displeasure caused by high luminance in the field view. Several design factors can influence discomfort glare including room size, shape, and wall surface reflectance's. Lighting factors such as illuminances, luminaire characteristics, and the number and location of luminaires also influence one's perception of visual comfort. Finally, human factors that affect glare include location, line of site, and individual differences of glare sensitivity (IESNA, 2000).

Windows, Luminaires, and Glare

Two important functions of windows are to provide an acceptable view to the outdoors and to transmit daylight into an adjacent interior zone. To accommodate the view to the outdoors, an adequate WWR is required. Consequently, with higher WWR's, an increased risk of glare is prevalent (Chauvel et al., 1982; Hopkinson, 1972). The addition of shading devices can reduce discomfort glare, however, reducing daylight into buildings may increase lighting loads (Bellia et al., 2014). In a typical office space, a minimum of 300-500 lux and up to 1000 lux are recommended on the workplane (Kapsis et al., 2015; Athienitis & Tzempelikos, 2002). To meet this range of illuminance, artificial lighting should be integrated, and these systems must not only be designed for performance but also to ensure visual comfort (Wienold & Christoffersen, 2006). Specifically, luminaires are recommended near walls to help increase surface luminance, while

direct and diffuse light are recommended to help reduce shadows from the occupant and desk objects. These design characteristics help to reduce overhead glare for visual comfort (IESNA, 2000). Furthermore, the occupant can face in the parallel direction with the window plane to reduce glare perception (Nazzal, 2005).

Glare Evaluation

A common method to evaluate glare is the daylight glare probability (DGP) which is calculated by the following formula:

$$\mathrm{DGP} = 5.87 \cdot 10^{-5} \cdot \mathrm{E_v} + 9.18 \cdot 10^{-2} \cdot \log\left(1 + \sum_{\mathrm{i}} \frac{\mathrm{L_{s,i}^2} \cdot \omega_{\mathrm{s,i}}}{\mathrm{E_v^{1.87}} \cdot \mathrm{P_i^2}}\right) + 0.16 \qquad (2.6)$$

E_v (lux) is the vertical illuminance at the eye, L_s (cd/m^2) is the source luminance, ω_s (sr) is the solid angle of the source, and P_i is the position index (Wienold & Christoffersen, 2006). The DGP is captured by use of cameras and is shown to have a reliable correlation with user perceptions of glare (Wienold & Christoffersen, 2005). The following figure shows luminance maps and the DGP at two different days of the year for the same time of day.

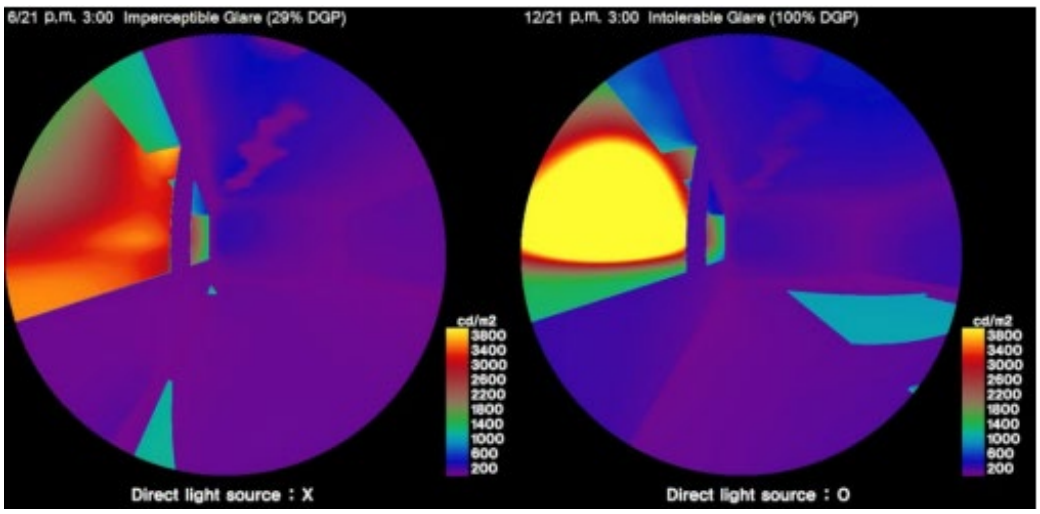

Figure 2.4. Glare due to Daylit Windows (Lee & Lee 2019).

Another method to assess glare from large sources (i.e., windows) is the daylight glare index (DGI) described by Chauvel (1982); Hopkinson (1972). This method does not require the use of cameras. The equations are based on experiments with uniform light sources, rather than real conditions of non-uniform light sources, and is calculated by the following equation where L_b is the background luminance (cd/m^2):

$$\mathrm{DGI} = 10 \cdot \log \cdot 0.478 \sum \frac{\mathrm{L_s^{1.6}} \cdot \omega^{0.8}}{\mathrm{L_b} + (0.07 \cdot \omega^{0.5} \cdot \mathrm{L_s})} \tag{2.7}$$

The 'new' Daylight Glare Index (DGI_N) evaluates glare with non-uniform lighting from windows (Nazzal, 2005). This method is completed experimentally with the use of three photometers and tests for a 'worst-case scenario'. This scenario is obtained by turning off the electric lighting and positioning illuminance sensors perpendicular to the center of the window face (Nazzal, 2005). The equation for the DGI_N is shown below:

$$\mathrm{DGI_N} = 8 \cdot \log_{10}\left(0.25 \cdot \left(\frac{[\sum(\mathrm{L_{ext}^2} \cdot \gamma_{\mathrm{pN}})]}{[\mathrm{L_{surr}} + 0.07 \cdot (\sum(\mathrm{L_{win}^2} \cdot \omega_{\mathrm{N}}))^{0.5}]}\right)\right) \tag{2.8}$$

L_{win} is the vertical luminance of the window, L_{ext} is the exterior vertical luminance, and L_{surr} is the average luminance in the room. ω_N (sr) is the solid angle subtended by the window, or glare source, to the point of observation, and γ_{pN} (sr) is the solid angle subtended by the source. This method is further described in Chapter 3. The table of glare criterion based on DGI values is shown in Table (2.2).

Table 2.2. Glare Perception Scale with Daylight Glare Index.

DGI	Glare Criterion	DGI	Glare Criterion	DGI	Glare Criterion
<16	Imperceptible	20	Just Acceptable	26	Uncomfortable
16	Just Perceptible	22	Acceptable	28	Just intolerable
18	Perceptible	24	Just Uncomfortable	>28	Intolerable

To meet the key performance indicators of energy efficiency, energy flexibility, thermal comfort, and visual comfort, correct design decisions must be made in the preliminary phases of building construction.

2.2. Design of Perimeter Zones in Net-Zero Energy Buildings

2.2.1. Passive Design of Perimeter Zones

Passive solar design uses the natural environment, climate, and building form to improve energy efficiency of the building while ensuring a comfortable environment for occupants. Passive solar design principles include the orientation of the building, shading systems, fenestration systems, building materials, thermal mass, and natural ventilation (Altan et al., 2016). Incorporation of passive strategies is essential in the design stage for net-zero energy buildings.

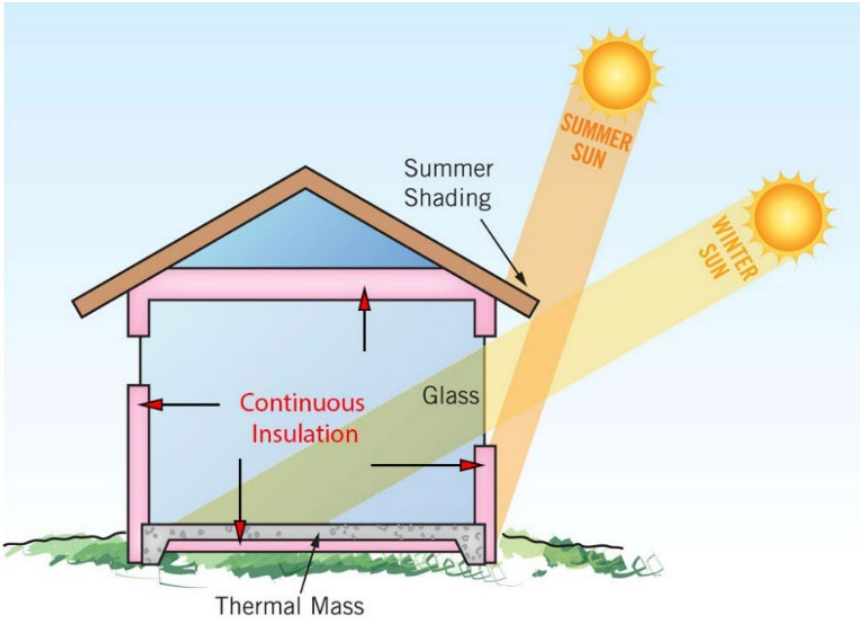

Figure 2.5. Passive Solar Components. (Eco Design Advisor, 2020).

Window-to-Wall Ratio

A major design component on building façades is the window-to-wall ratio, which is the ratio of window area to the façade area. According to ASHRAE Standard 90.1 (2016) office buildings with less than 5,000 ft^2 (464.5 m^2) of floor area should have a maximum WWR of 19%. Office buildings with floor areas between 5,000-50,000 ft^2 (464.5-4,645.2 m^2) and greater than 50,000 ft^2 (4,645.2 m^2), should have a maximum WWR of 31% and 40%, respectively.

Window Design

Significant amounts of heat gains and losses in buildings are due to windows, which has a considerable effect on both space conditioning and occupant comfort (Hee et al., 2015). Fenestration systems have improved with the introduction of low emissivity (low-E) coatings. This technology originated in the 1960's and has had a major impact on energy savings in buildings (Glaser, 2008). These coatings are spectrally selective such that they reduce radiant heat exchange without conceding transmitted daylighting (ASHRAE, 2017). To further reduce heat transfer

within the cavities of the glazing units, inert gases such as argon or krypton are often pumped into the evacuated air cavity (Manz, 2008; Zoller, 1913).

Passive Thermal Mass

Thermal mass and resistance are important passive design aspects for thermal management in buildings. The standard for minimum thermal resistance is continuously updated in ASHRAE Standard 90.1 (ASHRAE, 2010b; ASHRAE, 2016), but as of 2010, there were no quantitative standards which require thermal mass (ASHRAE, 2010b; Wang et al., 2014). Thermal mass in buildings is an effective approach to improve building performance. Essentially, thermal mass absorbs heat and stores the energy during warmer conditions and releases this thermal energy during cooler conditions (Ma & Wang, 2012).

Energy loads may be significantly reduced while maintaining comfort by combining passive design techniques, such as equator facing perimeter zones, optimal WWRs, modern fenestration designs, acceptable building thermal resistance, and sufficient thermal mass. To further neutralize the energy loads, the addition of renewable energy systems (i.e., building integrated photovoltaics; BIPV), can allow a building to achieve a net-zero energy status.

2.2.2. Active Building Envelopes: Building Integrated Photovoltaics

For a building envelope to be considered an Active Building Envelope (ABE) one of two conditions must be met. One of these conditions' states that a building envelope system transforms renewable energy (i.e., solar energy) into conventional energy (i.e., electrical energy) to improve building performance (Luo et al., 2019). Photovoltaic elements on buildings have historically been integrated in skylights, roofs, and walls, but applications of PV within glazing have been progressing. BIPV windows are ideal candidates to reduce energy demands in buildings through

electricity generation and transmittance (Skandalos & Karamanis, 2015). Semi-transparent photovoltaic (STPV) windows are a type of BIPV commonly integrated into the façade. An STPV window is a design that can generate solar electricity while reducing occupant discomfort by limiting solar gains and daylight, while providing an adequate view of the outdoors (Bahaj et al., 2008; James et al., 2009). This study focuses on the use of opaque-spaced STPV cells.

Packing Factor

When designing opaque spaced STPV for implementation in a building, there is a trade-off between electricity generation and transparency. Packing factor (PF) is the design variable which must be optimized and is the ratio of PV cell area to the window area. The distance between rows of PV cells, dc, will decide the transparent glazing area (see Figure 2.6). Higher PFs provide a higher potential of energy generation but reduce transmitted daylight and solar heat gains while obstructing the exterior view Alternatively, lower PFs decrease potential electricity generation but increase admitted daylight and heat gains while improving the exterior view. Interior shading patterns must also be considered when choosing STPV design (see Figure 2.7; Hachem-Vermette, 2020).

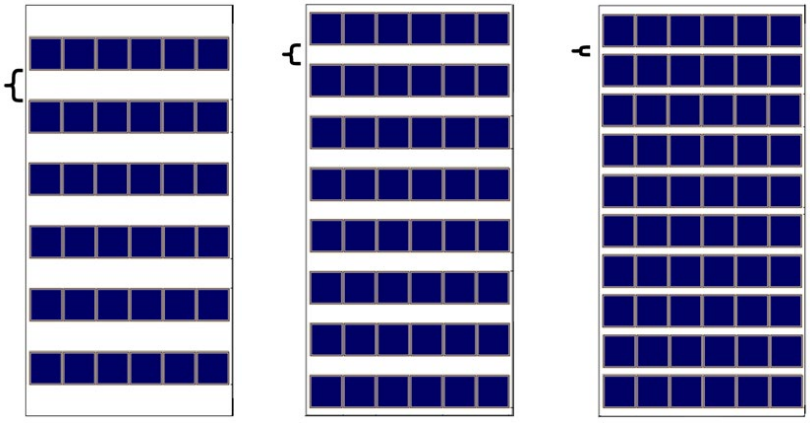

Figure 2.6. Schematic of different Packing Factors for Opaque-STPV.

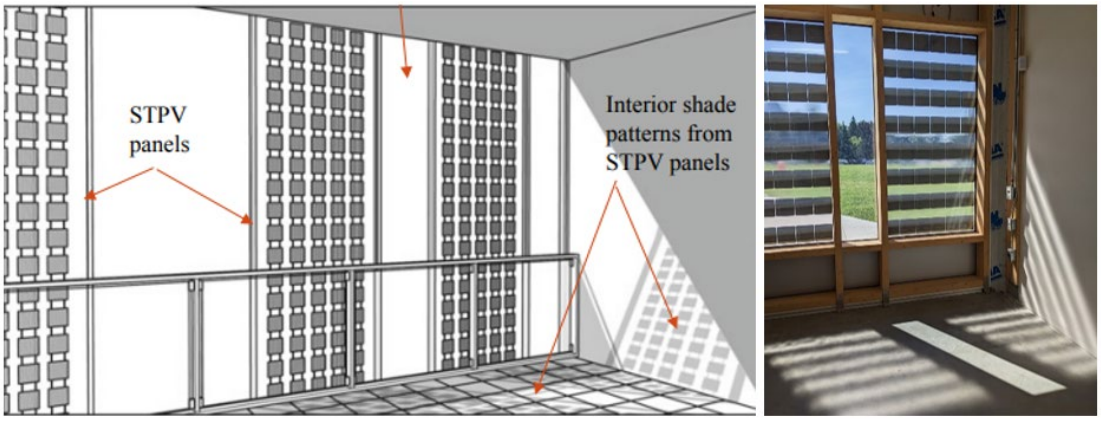

Figure 2.7. Interior Shading Pattern from Opaque-STPV. Left:(Hachem-Vermette, 2020), Right: Future Building's Lab.

Photovoltaic Cell Type

Monofacial PV cells have been historically designed into these systems, but with the emergence of bifacial PV cells, electricity generation from these systems can be improved. Bifacial PV cells have been produced industrially since 1984 (Lorenzo, 2021), and these cells allow electricity generation from both sides of the material. Light and solar radiation within a window is either transmitted, absorbed, or reflected. The reflected portion will be transmitted, reflected, and absorbed again, continuing an infinite number of times. This can also be applied to opaque surfaces, which will absorb and reflect the light and solar radiation (IESNA, 2000). Shown below is the equation used to calculate the illuminance at a point in space with the apparent luminous exitances M_i of n surfaces, which can be converted to irradiance.

$$\mathrm{E_{inter}} = \sum_{\mathrm{i=1}}^{\mathrm{n}} \mathrm{c_{i\rightarrow p}} \cdot \mathrm{M_i} \qquad (2.9)$$

E_{inter} is the illuminance produced by the interreflection in the window, and $c_{i\rightarrow p}$ is the configuration factor from surface i to point p. Due to the inter-reflections of the insulated glazing unit (IGU), energy generation can be increased without the need to increase the glazing area. A

recent simulation study found that bifacial PV cells increased electricity generation between 4.7% - 18.8%, when compared to monofacial PV cells (Chen et al., 2021). Soria et al. (2016) completed a small-scale study of bifacial STPV on a façade with the addition of a reflective plate at different distances from the module and found a 25% annual increase of electrical energy generation when compared to monofacial PV cells.

In this study, highly reflective venetian blinds are integrated between the two inner glazing layers of the IGU, acting as a reflector plate. The bifacial STPV design is significant when considering control strategies of motorized venetian blinds; different blind tilt angle (β) strategies of the MVB can be evaluated to assess the improvement of electricity generation.

2.2.3. Solar Shading with Motorized Venetian Blinds

The regulation of daylight and solar gains is essential to enhance a building's energy performance and to ensure both thermal and visual comfort of occupants (Szokolay, 2014; Kensek & Hansanuwat, 2011). Conventional shading systems are static (i.e., overhangs) or manual (i.e., roller shades). Static shading can alleviate overheating during peak radiation hours (Al-Tamimi & Fadzil, 2011), but is inadequately responsive to inconsistent conditions over a series of days (Al-Masrania et al., 2018). Additionally, inconsistent amounts of natural daylight will be admitted into the building with static shades, potentially causing increased lighting energy demands (Kensek & Hansanuwat, 2011). Depending on building form and location, static shades only provide optimal conditions for limited times throughout the day. Therefore, static shades are becoming unfavorable designs for current and future buildings in terms of control and energy efficiency (Al-Masrania & Al-Obaidi, 2019).

Advancements in façade design and higher WWRs increase the need for dynamic shading for the regulation of both daylight and solar radiation (Johnsen & Winther, 2015). When compared to conventional shading, dynamic shading devices are automatically operated systems which respond to both exterior and interior environments to provide improved comfort and energy performance (Kim et al., 2009). This is even more crucial when perimeter zones have thermally activated building systems (TABS) integrated into the design.

2.2.4. Thermally Activated Building Systems in Perimeter Zones

Thermally activated building systems store and transfer heat using embedded water pipes or air ducts to act as heat exchangers. TABS are a favorable technology for enhancing both energy efficiency (Navarro et al., 2016) and energy flexibility (Dermardiros et al., 2017). Other benefits of thermal energy storage systems include economic feasibility, and reduced pollution and CO_2 emissions (Dincer & Rosen, 2002). Radiant floor systems have a high temperature gradient near the surface of the floor, but as the room height increases, the temperature distribution is uniform to maintain thermal comfort (Khorasanizadeh et al., 2014). Designing and controlling radiant heating systems for perimeter zones can be complicated when considering both internal and external modes of heating. The thermal mass is heated internally by hot water being pumped through piping and on the surface from transmitted solar radiation (Athienitis, 1997).

Thermal inertia of a building is frequently included as a methodology to improve thermal performance. Materials of high thermal mass such as concrete are used to increase thermal storage capacity and minimize thermal fluctuations of the envelope. This study focuses on the integration of TAB systems into the floor. TAB systems are considered to be promising technologies for commercial and institutional buildings, where applications in the floor allow increased exposure to solar gains admitted into a zone (Navarro et al., 2016).

Proper design of TAB systems must be ensured, and the design variable considered in this study is slab thickness (L_{slab}). When designed with insufficient thickness, these systems have a lower thermal lag, in which the thermal response of the floor surface and room air temperature will be reduced. This can decrease the ability of a building to use stored heat for when later needed. Conversely, a high slab thickness will produce a higher thermal lag and longer thermal response to surface and room temperatures (Gomez et al., 2017). Another design consideration for TAB systems is the location of the piping, whether that be at the base, in the middle, or near the top of the slab. Shown in figure (2.8) is a cross-section of a hydronic radiant floor heating system in a perimeter zone, with pipes embedded at the bottom of the slab. L_{slab} is shown as the design variable and the external and internal heating sources are q_{solar} and q_{aux}, respectively:

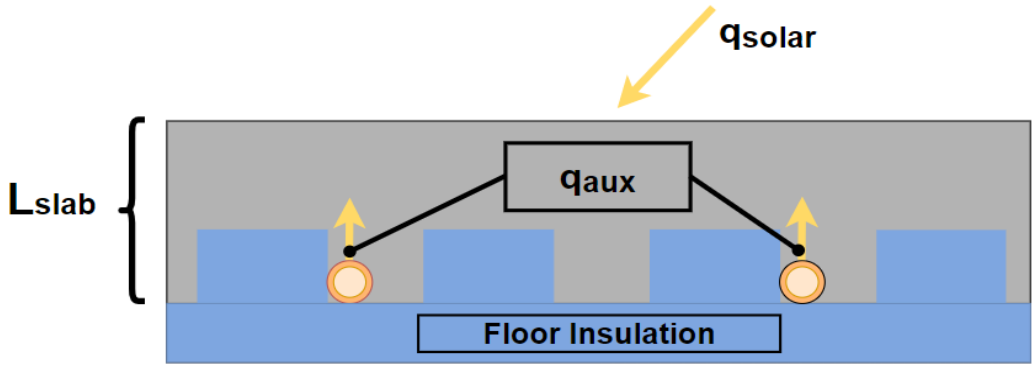

Figure 2.8. Cross-section of Hydronic Radiant Floor System.

As design plays a major role in building performance, the control of its integrated systems during the operational stage is equally as important to meet energy performance and occupant comfort targets. Katipamula & Brambley (2005) found that improper control contributes to 15%-30% of wasted energy in commercial and institutional buildings. A leading example of poor control techniques include incorrect temperature setpoint strategies. When considering HVAC systems, Akinci et al. (2011) summarized that between 25% and 45% of energy used was wasted (e.g.,

heating with no occupancy). A review completed by Roth et al. (2005) concluded that an increase of 4%-20% of primary energy consumption in the US was caused by HVAC, lighting, and refrigeration system faults, such as unnecessary system usage, poor control strategies, and malfunctioning of system controllers. The following section reviews literature on the current state of building control for shading and TAB systems and will introduce methods of control to reach key performance indicators in perimeter zones.

2.3. Modelling and Predictive Control for Net-Zero Perimeter Zones

Currently, rule-based control (RBC) methods are commonly utilized in buildings (Prívara et al., 2013). Rule-based control is typically implemented through temperature setpoint manipulation, such as pre-conditioning or nighttime setbacks, without the use of building models. Even with only near-optimal operating points achieved, these techniques can realize considerable improvements in energy performance for buildings (Mařík et al., 2011). Fixed setpoint schedules are developed to obtain a desired goal such as energy efficiency (e.g., nighttime setback) or energy flexibility (e.g., pre-heating setpoint) without the use of weather forecasts or building models.

With advancements in computing power and increased data collection, model predictive control (MPC) has become of high interest in modern building research (Athienitis & O'Brien, 2015). These controllers require building models to optimize energy performance by predicting thermal behaviour of the building and thermal comfort for occupants. MPC can be classified into three categories: white, black, and grey box models. White box models use physical principles, black box models are purely data-driven models, and grey box models combine both physics and data-driven models (Foucquier et al., 2013). A drawback of these MPC controllers include the significant cost and time for training and monitoring to provide optimal operation. To allow the

MPC to operate appropriately, smart meters must be implemented to permit communication between the customer and the electric grid (Péan et al., 2019). The combination of rule-based control and model predictive control may be adopted; this concept is a heuristic MPC approach. Rule-based control of building systems (i.e., temperature setpoint strategies) can be incorporated to physical building models.

2.3.1 Modelling Perimeter Zones

Resistance-Capacitance Thermal Networks

A common grey-box modelling approach is resistance-capacitance models (RC). In a thermal zone we can represent different walls and surfaces by different nodes, which have a connected thermal resistance, *R*, and thermal capacitance, *C*. Additionally, these nodes may have a heating source applied, including but not limited to solar radiation, radiators, waste heat from lights, and occupants. Thermal networks are described by the analogy of electrical systems, using Ohm's law and Kirchhoff's law, and are represented by thermal circuits (Athienitis & O'Brien, 2015; Bagheri et al., 2016). An important first step in this approach is to choose the order of the model, in other words, the number of capacitances in the thermal network.

A first order model considers one thermal capacitance, and assumes the floor has significant thermal mass, relative to the other surface materials (Athienitis, 1999). Shown in figures (2.9 and 2.10) is a schematic of a reduced order thermal zone model with its appropriate RC thermal network, respectively. These figures give a simple representation of RC thermal networks for perimeter zones.

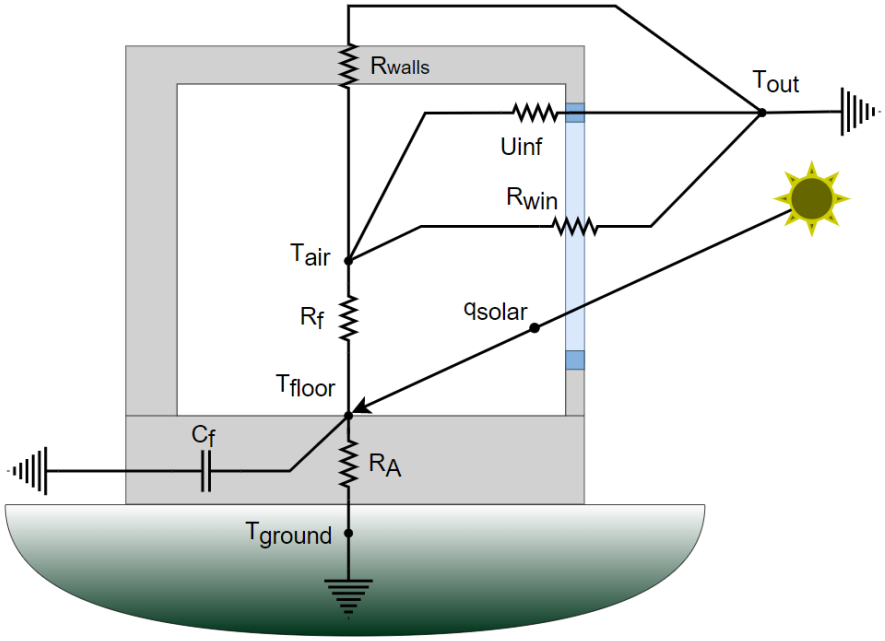

Figure 2.9. Example of First Order Room Model, Schematic.

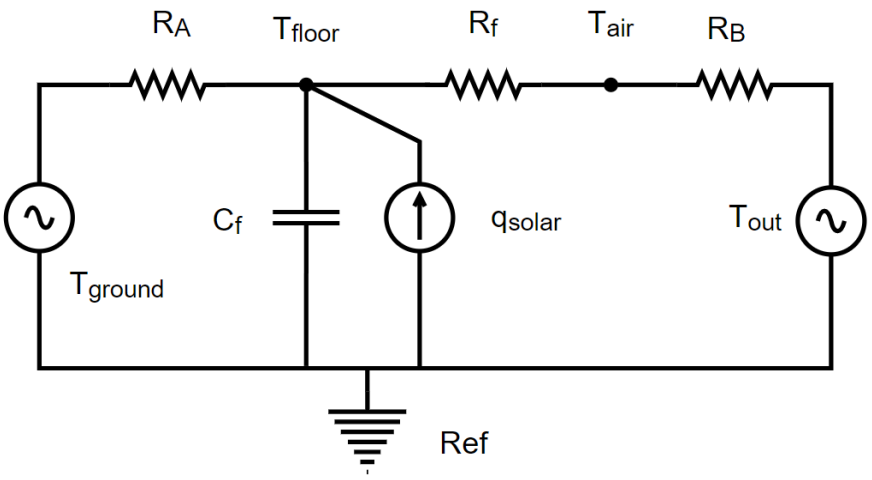

Figure 2.10. Example of RC Thermal network of First Order Thermal Zone.

R_A is the thermal resistance of the thermal storage mass, insulation, and the ground, $R_B = 1/\left(\frac{1}{R_{walls}} + \frac{1}{R_{win}} + U_{inf}\right)$ is the effective resistance to the exterior temperature node, q_{solar} is the transmitted solar radiation incident on the floor mass, and C_f is the thermal capacitance of the floor mass. Higher detailed RC models can be developed to give a higher accuracy model, meaning

splitting thermal capacitances into multiple layers, to increase the order of the model (Athienitis, 1999).

Lumped Capacity Analysis

For low-order thermal models the Biot number must be less than or equal to 0.1 for the model to be accurate. This dimensionless parameter determines the temperature drop in the concrete relative to the temperature difference between the surface of the concrete and the air (Incropera et al., 2011; Yuan et al., 2018). The Biot number is calculated using the equation below:

$$\mathrm{Bi} = \frac{\mathrm{h_{cf}} \cdot \mathrm{L_{char}}}{\mathrm{k_{con}}} \leq 0.1 \qquad (2.10)$$

Bi is the Biot number, h_{cf} is the convective heat transfer coefficient of the hot floor to the air node, L_{char} is the characteristic length, and k_{con} is the thermal conductivity of concrete. For hydronic radiant floor systems with concrete having low thermal conductivity (i.e., lightweight concrete) the Biot condition is not usually met. Therefore, the concrete should be discretized into multiple sublayers, which increases the order of the model. For thermal zones with radiant systems, RC models of order 3 or 4 are generally considered accurate (Candanedo et al., 2022).

RC thermal networks is a simple approach for modelling thermal zones to provide accurate simulation of a desired goal. Another benefit to these models is that they can be coupled with control systems, thus allowing the model to train with collected data and help achieve a net-zero status (Bagheri et al., 2016). The RC model used in this thesis will be discussed in Chapter 3.

Finite Difference Method

The finite difference method is a simple way to move from a steady state to a transient domain, and this method is considered reliable in creating accurate building models (Bagheri et al., 2018).

In the transient finite difference method, daily temperatures, heating profiles, peak heating loads, and solar effects can be calculated in RC networks. An energy balance is then applied to each node, which calculates the temperature as a function of time (Athienitis & O'Brien, 2015; Bagheri et al., 2016). The general form of the explicit finite difference method is shown below in equations (2.11) and (2.12).

$$\mathrm{T_{i,p+1}} = \left(\frac{\Delta \mathrm{t}}{\mathrm{C_i}}\right) \cdot \left(\mathrm{q_i} + \sum_{\mathrm{j}} \frac{\mathrm{T_{j,p}} - \mathrm{T_{i,p}}}{\mathrm{R_{i,j}}} \right) + \mathrm{T_{i,p}} \tag{2.11}$$

$$\Delta \mathrm{t_{critical}} = \min \left(\frac{\mathrm{C_i}}{\sum_{\mathrm{j}} \frac{1}{\mathrm{R_{i,j}}}} \right) \tag{2.12}$$

$T_{i,p}$ is temperature of node 'i' at time step 'p', $T_{j,p}$ is temperature of node 'j' at time step 'p', C_i is the thermal capacitance of node 'i', $R_{i,j}$ represents the thermal resistance between nodes 'i' and 'j', and q_i is the heat source at node 'i' (Athienitis & O'Brien, 2015; Hill & Athienitis, 2023). In equation (2.11), $\Delta t_{critical}$ symbolizes the critical time step of the zone, calculated from all capacitances in the model.

2.3.2. Control of Hydronic Radiant Floor Heating Systems

Controlling these systems in thermal zones is typically done with a thermostat. One of the main concerns when installing a thermostat, especially in perimeter zones, is the potential for high solar radiation incident on the device. Indeed, the thermostat may interpret the whole zone temperature as increasing and signal an air conditioning system to cool the zone. This can cause a significant increase in cooling loads and may lead to thermal discomfort (McDowall, 2007).

Typically, water or a water-glycol mix is supplied through the piping within the hydronic system. Temperature setpoint strategies will allow a supplying water tank to decide if water is needed, and

what supply temperature is necessary to meet the setpoint. An advantage of TABS includes maintaining a lower room temperature setpoint in the heating season due to the radiant heat transfer between the large floor and other surfaces (Rhee & Kim, 2015). Despite this advantage, previous research on TABS control in perimeter zones has revealed challenges when considering weather patterns combined with a high thermal inertia of a concrete slab (Joe & Karava, 2019). Furthermore, when controlling for energy efficiency or energy flexibility, different control approaches are used.

Energy Efficiency

When controlling for energy efficiency, nighttime setbacks have shown to reduce the annual energy consumption of buildings (Manning et al., 2007; Tariku et al., 2008). Moreover, office buildings are assumed to have no occupancy at these times when considering a typical workday, therefore, constraints of comfort may be omitted during nighttime hours (Brooks et al., 2015). Consequently, these setback strategies may increase energy loads during peak demand periods (Ingersoll & Huang, 1985), further increasing stress on the electric grid.

Energy Flexibility

A common technique used for energy flexibility is preheating, which preheats the TABS before occupation hours or peak demand periods. The goal of this strategy is to reduce the total energy demand of the building and/or improve energy flexibility to reduce the stress on the electric grid during critical times (Ramos et al., 2019; ASHRAE, 2019). Figure (2.11) shows two general examples of temperature setpoint strategies, with the peak demand periods highlighted: nighttime setback for energy efficiency (blue), and pre-conditioning for energy flexibility (red).

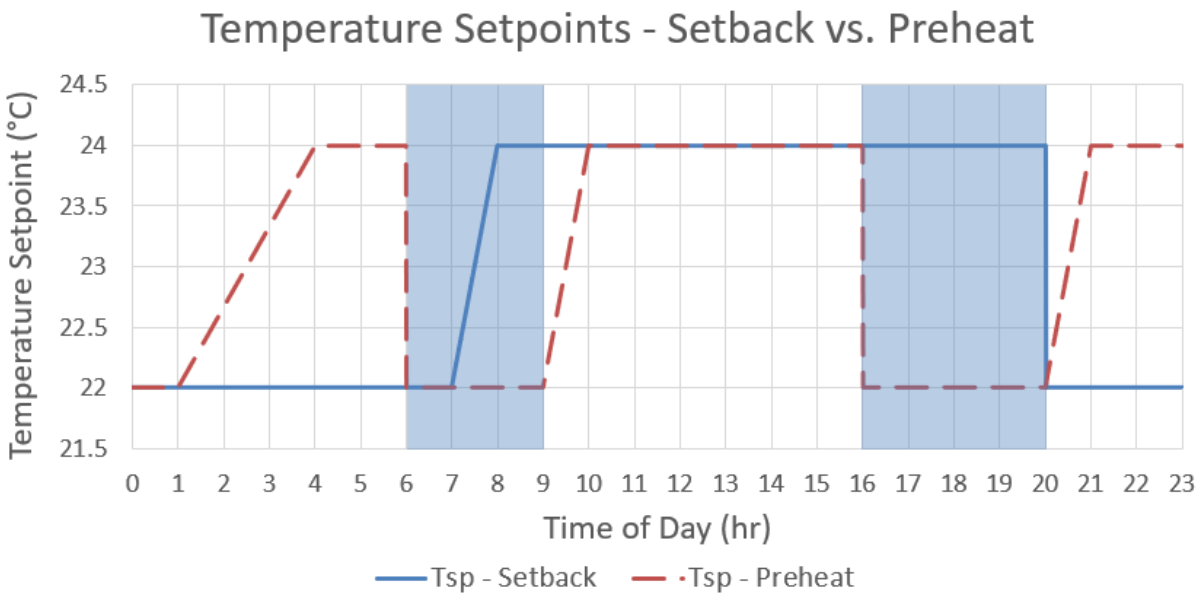

Figure 2.11. Two examples of Temperature Setpoint Strategies

Thermal Time Constant and Thermal Response Time

Before developing temperature setpoint strategies with hydronic radiant floor systems, the thermal time constant and thermal response times should be calculated. The thermal time constant calculates the time it takes for a system to reach 63.2% of the steady state temperature. The thermal response time describes the time it takes a system to reach 95% its steady state value. Ning et al. (2017, pg.40) defined the thermal response time of a radiant system as "the time it takes for the surface temperature of a radiant system to reach 95% of the difference between its initial and final values when a step change in control of the system is applied as input". The lumped capacity analysis is not suitable in determining the time constant for radiant systems with large thermal mass. Therefore, when determining the response times of radiant systems, experimental response curves should be analyzed to calculate different response times (e.g., 50%, 63.2%, 95%, etc.). These curves will allow the development of improved temperature setpoint strategies. Further, Ning et al. (2017) concluded that concrete thickness and pipe spacing had the most significant impact on the thermal response time of TAB systems. Concrete type had a lesser but still

considerable effect, while pipe diameter, operative temperature, water flowrate, and water supply temperature did not have a significant influence on the thermal response time of these systems.

TABS with Shading Devices

Beji et al. (2020) examined the dynamic thermal behaviour of a radiant floor heating system when subjected to direct solar radiation for different durations. It was found that high room air and floor surface temperatures occurred with a longer time duration of 6 hours, while low durations of 2-hour direct solar radiation caused only slight overheating. Furthermore, the area of sun-patch showed an increase in surface temperature of 11-21 ºC when compared to the non-exposed area. This study provides insight on how radiant floor heating systems should be coupled with solar shading systems in perimeter zones to ensure occupant comfort (Romani et al., 2016).

2.3.3. Control of Motorized Venetian Blinds

Excessive solar gains and luminance may result in overheating and glare. Therefore, shading systems must be controlled to improve energy performance, without conceding occupant comfort. Blind tilt angle (β) is the controlled variable of motorized venetian blinds, and three components are necessary for its automated response. First, sensors obtain necessary data, a controller then decides a suitable action, and finally, an actuator performs the desired action (Konstantoglou & Tsangrassoulis, 2016). One common control strategy for these shading systems is the always open (AO) blind control strategy which rotates the blind tilt angle parallel to the sun rays. Maximum daylight and solar radiation transmission occurs with this control strategy to provide passive heating and lighting, although, risks of glare and overheating increase. Another common control strategy is the cut-off (CO) control strategy which rotates to an optimal tilt angle for blocking direct beam solar radiation and daylight while admitting their diffuse components. Risks of

overheating and glare are reduced with this control strategy (Athienitis & Tzempelikos, 2002). See figure (2.12) for schematics of the “always open” and “cut off” blind control strategies.

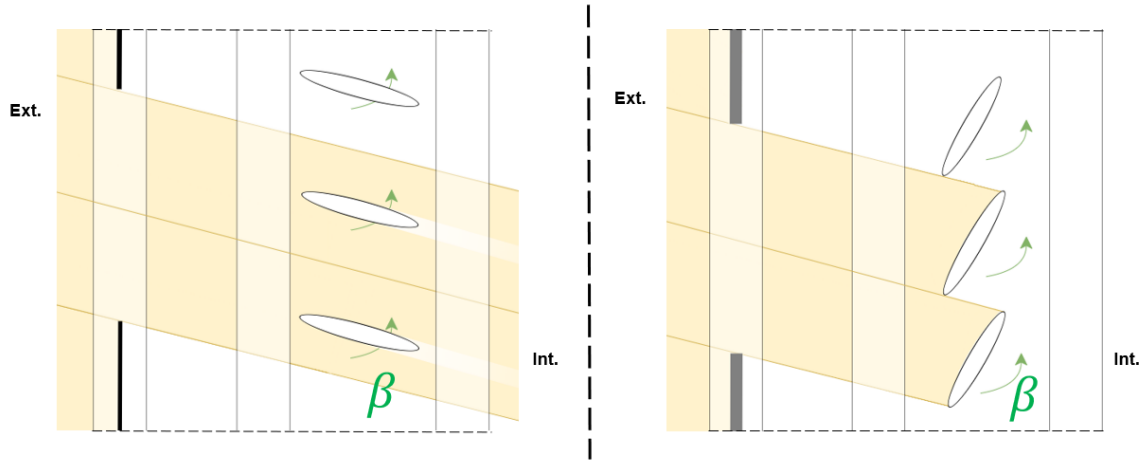

Figure 2.12. Two examples of reflective blind control strategies. Always Open Control (Left) and Cut-off Control (Right).

2.4. Research Gaps and Aim of the Current Study

Interaction between NZEB elements

For buildings to operate as a near-NZEB or NZEB common practices and design techniques are undertaken (Kolokotsa et al., 2011; Belussi et al., 2019; Magrini et al., 2020):

- Passive design techniques (e.g., building orientation, optimal WWRs, sufficient thermal mass).
- Use of renewable energy systems (e.g., bifacial semi-transparent PV windows).
- Innovative shading devices (e.g., motorized venetian blinds).
- Efficient heating equipment (e.g., hydronic radiant floors).

This study investigates the interactions between these systems for achieving optimized energy performance and occupant comfort in perimeter zones for net-zero energy buildings.

Research Gaps

Based on the literature discussed above, there are optimal design techniques and control approaches to improve the energy performance of perimeter zones, while maintaining occupant comfort, with these specific set of systems (i.e., bifacial STPV windows, motorized venetian blinds, and hydronic radiant floor heating systems).

Beji et al. (2020) studied different durations of direct solar radiation on TAB systems and concluded that although the TAB systems improved energy performance in perimeter zones shading devices would be necessary to avoid overheating. Zhao et al. (2022) studied the interior environment with the addition of a bifacial PV window and concluded overheating during high solar radiation periods. This was mainly due to the transparent area and the higher temperatures associated with bifacial PV cells. One key conclusion was the addition of a reflective layer behind the PV cells and an optimal packing factor could improve the occupant comfort while producing sufficient electricity. Furthermore, transmitted daylight may be excessive on clear days and with high transparent façade areas, leading to a potential visual discomfort. In addition, Soria et al. (2016) examined the energy generation of bifacial STPV windows with an added reflector plate at different distances from the PV cells and found improved energy performance. Importantly, these reflector plates are akin to reflective venetian blinds, suggesting that the introduction of venetian blinds in combination with TABS and bifacial STPV windows may be an optimal system design to improve energy performance of perimeter zones while maintaining occupant comfort.

Finally, Athienitis et al. (2020) examined energy flexibility with a floor heating system of high thermal mass in a perimeter zone with a high WWR and demonstrated improved energy flexibility. This study will expand upon the findings of Athienitis et al. (2020) by parametrically analyzing different combinations of key design variables described in Chapter 1, with the addition of an

active solar window with integrated motorized shades for the benefits of energy flexibility. It appears no research to date has examined the combination of active bifacial solar windows, motorized shading devices, and thermally activated building systems for perimeter zones experimentally. Therefore, the current study will examine these three systems and their implementation in perimeter zones for the combined benefits of energy performance and occupant comfort.

Chapter 3: Case Study and Methodology

This thesis presents a model for optimizing the design and control of perimeter zones with bifacial semi-transparent photovoltaic windows (STPV), motorized venetian blinds (MVB), and hydronic radiant floor heating systems (HRFH). The perimeter zone case study is presented with its integrated systems, geometry, and materials. The developed Resistance-Capacitance Model (RC), Facade Model, and Hydronic Radiant Floor model are all shown with their specified assumptions. Near-optimal control strategies used in this thesis for the blind tilt angle of the venetian blinds, temperature setpoint strategies, and artificial lighting are described. Finally, the simulation procedure to meet the targets of key performance indicators is explained. Figure (3.1) shows the scope of the methodology:

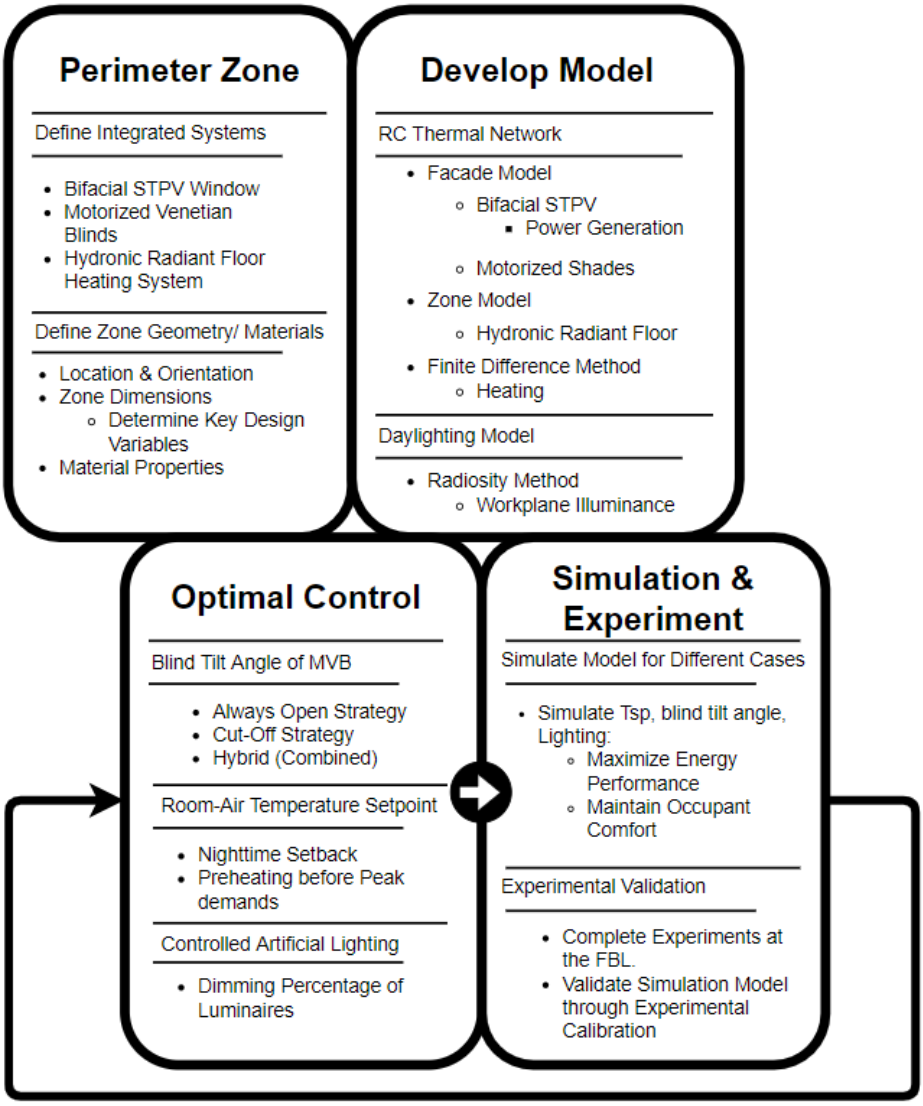

Figure 3.1. Methodology Scope.

3.1. Case Study of Perimeter Thermal Zone

Experimental work was completed at the Future Building's Lab (FBL) on Concordia's Loyola campus, in Montreal, Quebec. This experimental lab is south facing and has five independent testing cells allowing for multiple experiments to be conducted simultaneously. Figure (3.2) shows the FBL with test cells used for experiments highlighted.

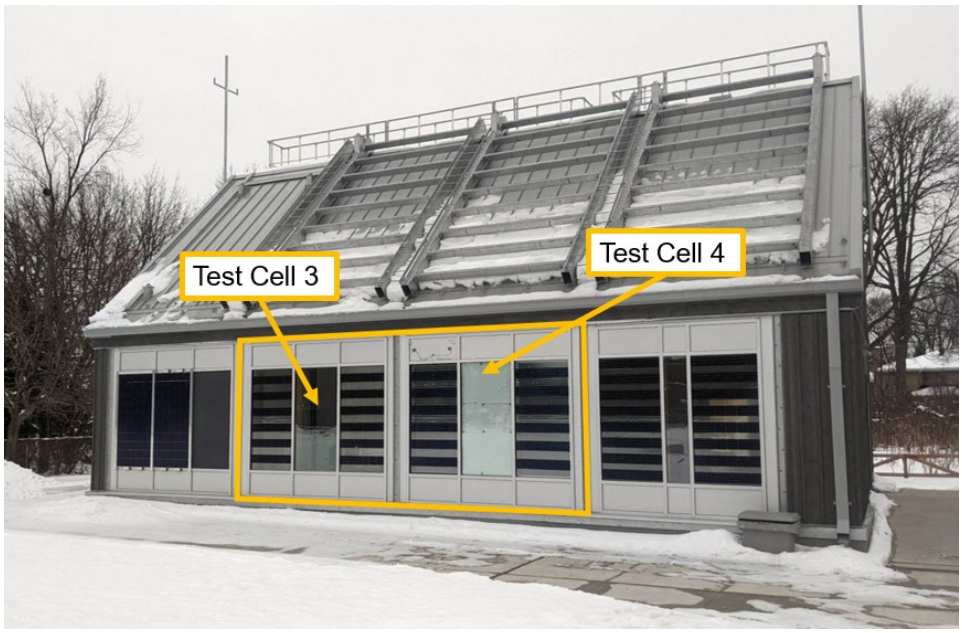

Figure 3.2. Future Building's Lab (FBL) in Montreal, Quebec.

3.1.1. Zone Description and System Identification

The three systems considered in this study are bifacial semi-transparent photovoltaic windows, motorized venetian blinds integrated within the STPV window, and hydronic radiant floor heating system. The bifacial STPV cells in test cell 4 are polycrystalline cells, the MVB are highly reflective and are integrated between the two inner glazing layers of each solar window. The concrete slab of the HRFH is a lightweight concrete mixture of low thermal conductivity. The necessary descriptions of the bifacial STPV window, MVB, and HRFH can be found in table 3.1. Additionally, the key design variables of window-to-wall ratio (WWR), packing factor (PF), and slab thickness (L_{slab}) can be found in table (3.1) with their installation values at the FBL. The hydronic system connection to the supplying water heater is described in section (3.2.1.1). Furthermore, occupants in this zone are assumed to be 1.55 m from the window (see figure 3.9) in line with the center of the double-glazed view section for typical working hours (8AM-5PM).

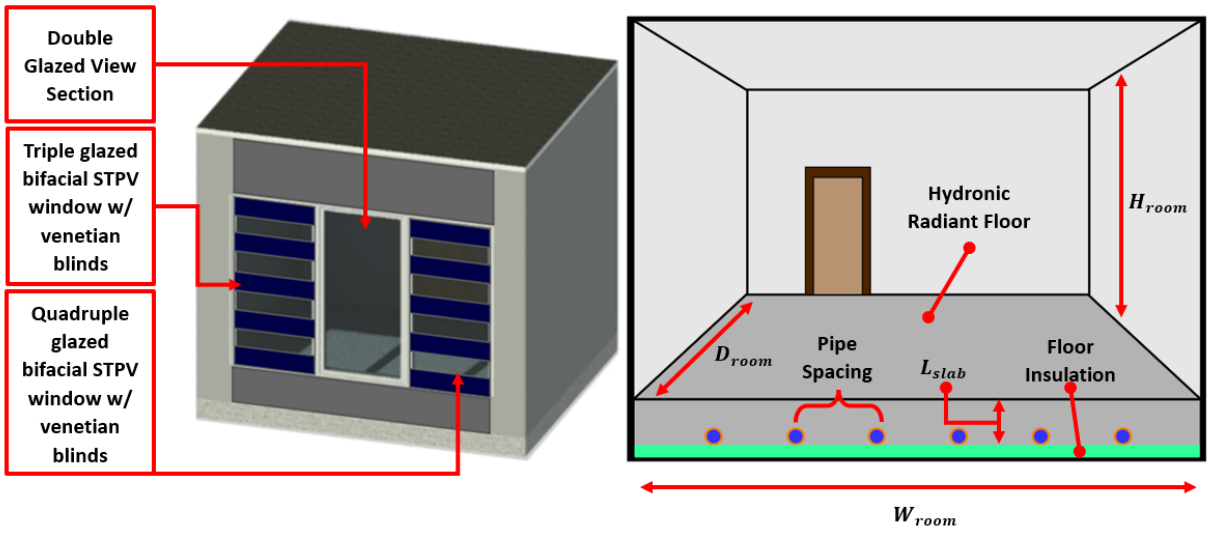

Figure 3.3. 3D Schematic of Test Cell 4. Left: Exterior; Right: Interior.

Table 3.1. Zone Dimensions and System Description.

Parameter	Test Cell 3	Test Cell 4
Window to Wall Ratio	38.7%	
Window Section Dimensions	Height = 1.954 m (6.41 ft)	
	Width = 0.986 m (3.23 ft)	
Window Design	Double Glazed	Left: Triple Glazed (TG) Middle: Double Glazed (DG) Right: Quadruple Glazed (QG)
STPV Cell Type	Monofacial	Bifacial
	Monocrystalline (black)	Polycrystalline (blue)
Packing Factor	45.9%	
Venetian Blinds (VB)	No	Yes
Slat Dimensions	-	Width: 34.9 mm
		Thickness: 6.4 mm
Slat Finish (Material)	-	Gloss White (Aluminum)
Distance from PV Cell to VB rotation axis (Center)	-	TG: 58.8 mm QG = 111.3 mm
Roller Shade	No	Yes
Concrete Floor Area	9.73 m^2 (104.73 ft^2)	
Concrete Slab Thickness	7.62 cm (3”)	10.16 cm (4”)
Pipe Location	Bottom of Slab	
Pipe Spacing	First 3 passes from window: 15.24 cm (6”) Remaining: 22.86 cm (9”)	
Room Height	2.88 m (9.45 ft)	2.85 m (9.35 ft)

The main test cell used in the model (see figure 3.5) is test cell 4, which has integrated venetian blinds in the bifacial STPV window. Test cell 3 is nearly identical in terms of dimensions and materials with differing facades, STPV, and hydronic slab thickness. Therefore, the model developed is transferrable between cells with minor adjustments.

3.2.1.1. Water Heater Connection to Radiant Floor

The HRFH system is supplied by a Rheem Hybrid Heat Pump/Water Heater, which has five operational modes, but this study uses 'Electric' mode only. Figure (3.4) shows a schematic of the connection between the water tank and the radiant floor. Table (3.2) describes the water tank parameters, water properties, piping design and dimensions, lightweight concrete (LWC) properties and the pump installed between the water heater and hydronic system. The installation procedure of the hydronic radiant floor and its connection to the water tank may be found in Appendix F.

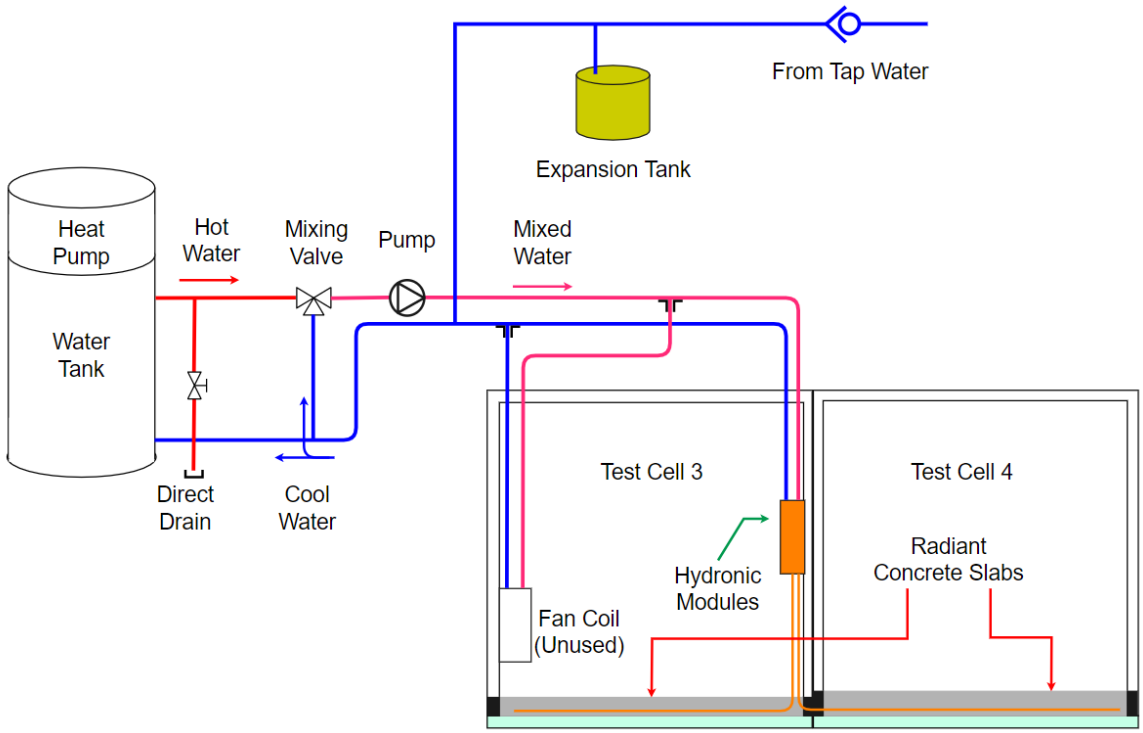

Figure 3.4. Schematic of Hydronic Radiant Floor Heating System Connected to Hot Water Tank.

Table 3.2. Water Tank Parameters, Water Properties, and Concrete Properties

Parameter	Value	
Pipe Length (Total)	106.7 m (350 ft)	
Pipe Pattern	Serpentine	
Piping	Interior Slab	PEX ($d_i = 1/2"$)
	Exterior to Slab	Copper ($\emptyset = 3/4"$)
Flow Rate	Test Cell 3	0.063 kg/s (1 gpm)
	Test Cell 4	0.095 kg/s (1.5 gpm)
Water Tank	Mixture	100 % Water
	Volume	189.3 L (50 gal)
	Uniform Energy Factor (UEF)	3.75
	Supply T	43 °C
	Specific Heat of Water (43°C)	4.18 (kJ/kg*K)
Lightweight Concrete Properties	Density	1995 (kg/m^3)
	Thermal Conductivity	0.872 (W/m*K)
	Specific Heat	913 kJ/(kg*K)
Grundfos Pump	Power	62.14 W (1/12 hp)

The expansion tank is used to protect closed loop water systems from excessive pressure due to thermal expansion; air partially fills the tank and compresses to help dampen the excess pressure. Water is heated in the tank and supplied through copper piping to a mixing valve and mixed with cooler return water after it has flowed through the PEX pipes. This mixed water is the supply water to the PEX pipes in the concrete slabs. The Hydronic modules shown allow for independent controllability in each test cell, as each zone has a programmable thermostat. A Watts ‘tekmar’ thermostat is used in both test cells 3 and 4. This device cannot program hourly temperature setpoints, but has four available setpoint events, and allows daily schedules to be set for each day of the week. To calculate the heating delivered to the slab from experiments we used the mass flow rate of water given by the following equation:

$$Q_{water} = \dot{m} \cdot C_p \cdot (T_{supply} - T_{return}) \quad (3.1)$$

$\dot{m}$ is the mass flow rate of the water, C_p is the specific heat of water, T_{supply} is the temperature of the water at the start of the loop, and T_{return} is the return temperature of the water through the hydronic loop. Supply and return temperatures are measured at the slab inlet and exit with thermocouples installed on the copper pipes.

3.2. Modelling of Perimeter Zone

RC Thermal Network

Reduced order RC models containing the critical physical information of the building can accurately represent buildings or thermal zones (Saberi-Derakhtenjani et al. 2015; Candanedo et al. 2022). The RC thermal network used in this thesis is a 3rd order model with a concrete layer having two capacitances, $C3$ and $C4$, and $C5$ is the capacitance of all wall surfaces lumped together.

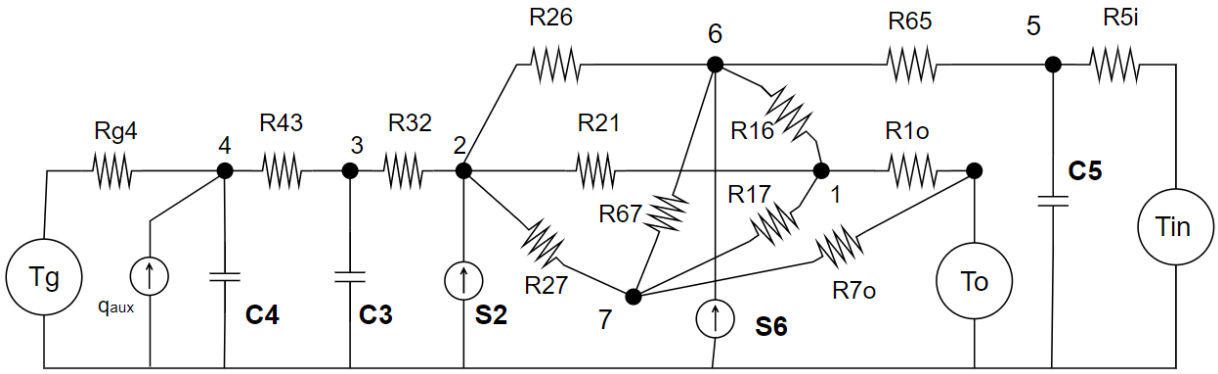

Figure 3.5. 3rd order RC thermal network model of a perimeter thermal zone.

The nodes in the figure (3.5) are described as:

- 1 Room Air
- 2 Floor Surface
- 3 1" below surface
- 4 1" above insulation
- 5 Midpoint between wall surface and adjacent zone surface
- 6 Wall Surface
- 7 Window Surface

The direct beam solar radiation incident on interior surfaces 2 and 6 are represented by $S2$ and $S6$, respectively. An approximation of 75% of the transmitted solar radiation incident on the floor surface ($S2$) with the remaining 25% incident on the unheated surfaces ($S6$) is assumed for simulations. This assumption is based on the ratio of floor to wall solar absorptance and the ratio between room width to depth (Athienitis & Stylianou, 1991). The calculated thermal resistances and capacitances are in table (3.3). The variable thermal resistances used in the finite difference method are denoted (FDM).

Table 3.3. Values of Parameters in RC Thermal Network shown above.

Parameter	Value	Parameter	Value
C3	900.66 kJ/K	**R5i**	0.059 K/W
C4	900.66 kJ/K	**R7o**	0.183 K/W
C5	278.54 kJ/K	**R43**	5.6 *10^{-3} K/W
Rg4	0.173 K/W	**R32**	2.8*10^{-3} K/W
R1o	0.096 K/W	**R17, R21, R27, R67, R26, R16**	Variable based on FDM
R65	2.3*10^{-3} K/W		
S_{ext}, To, Tin, Tg	Measured	***qaux***	Variable (Q_{water})

Finite Difference Method

The finite difference method is used to calculate temperature profiles, daily heating and peak heating loads in the RC model shown above. For clarity, the general form of the explicit finite difference method is described below:

$$T_{i,p+1} = \left(\frac{\Delta t}{C_i}\right) \cdot \left(q_i + \sum_j \frac{T_{j,p} - T_{i,p}}{R_{i,j}}\right) + T_{i,p} \tag{3.2}$$

$$\Delta t_{critical} = min\left(\frac{C_i}{\sum_j \frac{1}{R_{i,j}}}\right) \tag{3.3}$$

$T_{i,p}$ is temperature of node 'i' at time step 'p', $T_{j,p}$ is temperature of node 'j' at time step 'p', C_i is the thermal capacitance of node 'i', $R_{i,j}$ represents the thermal resistance between nodes 'i' and

'j', and q_i is the heat source at node 'i' (Hill & Athienitis, 2023; Athienitis & O'Brien, 2015). Equation (3.3), $\Delta t_{critical}$ symbolizes the critical time step of the zone, calculated from all capacitances in the model. The chosen timestep must be lower than the minimum value for numerical stability and was chosen to be 360 seconds (6 min). Shown in equation (3.4) is the auxiliary heating delivered from the hydronic radiant floor heating system, q_{aux}. The proportional control constant is K_p, where an adequate value is $^{q_{max}}/_{2}$ (Athienitis, 1999). T_{sp} represents the temperature setpoint, and $T_{1,p}$ is the room air temperature at time step 'p'.

$$\mathrm{q_{aux}} = \mathrm{K_p}\left(\mathrm{T_{sp}} - \mathrm{T_{1,p}}\right) \tag{3.4}$$

The list of equations used in the FDM may be found in Appendix A which is the programming codes with finite difference equations summarized in the thermal model.

3.2.1. Façade and Window Model

Figure (3.6) shows an energy balance of a triple glazed (TG) window with integrated venetian blinds within the two inner glazing layers and bifacial STPV cells embedded in the exterior glazing layer. The solar radiation and daylight incident on the front will be used to calibrate the RC model for the transmitted portions into the zone. Based on the optical properties of the blind layer, we can calculate the reflected portion back to the bifacial PV cells. The exterior temperature is another measured parameter used to calibrate the model. Initially a thermocouple was installed on the exterior of the building with a radiation shield. During clear days the solar radiation was deemed to cause inaccurate readings, therefore, temperature data from the airport weather station was used. The schematic is not to scale and shows a triple glazed window rather than all DG, TG, and QG windows. The solar and visible transmittance on a clear day of each window section were determined using the exterior and interior measured solar radiation and illuminance. Li-Cor

pyranometers and photometers were mounted on the exterior of the window-wall, shown in table (3.4).

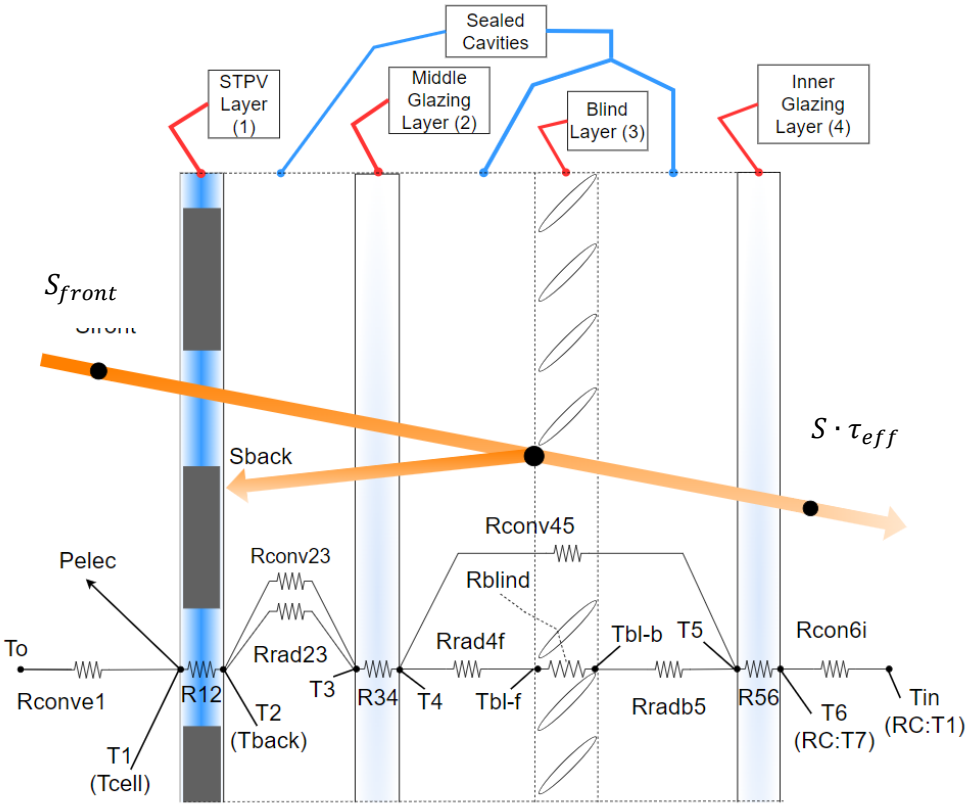

Figure 3.6. Energy balance of Triple Glazed STPV window.

The interior surface node in the figure below ($T6$) is considered node '7' in the RC model shown above with $R6i$ corresponding to the convective heat transfer coefficient to the room air ($R17$) and the remaining thermal resistance corresponds to $R7o$.

Table 3.4. Solar and Visible Transmittance Properties for a Clear Day

-	Window Section		
Property	Triple Glazed STPV	Double Glazed – Low-E View	Quadruple Glazed STPV
$\boldsymbol{\tau_{solar}}$	58.9%	49.8%	49.0%
$\boldsymbol{\tau_{vis}}$	65.8%	67.9%	61.5%

Heat Transfer through the Window

With the assumption of turbulent flow, the following correlation may be used for the convective heat transfer coefficient between the room air and window interior (Athienitis, 1999). T7 is the interior surface of the window facing the room and T1 is the room air:

$$\mathrm{h_{cwin}} = 1.31 \cdot (\mathrm{T7} - \mathrm{T1})^{1/3} \tag{3.5}$$

To calculate the heat transfer through multi-glazed windows with the venetian blinds WINDOW 7.7 (LBNL, 2019b) software was used for surface temperatures within the window cavities. The windows installed at the FBL are sealed and thermocouples cannot be applied to the interior surfaces within the system. This software uses NFRC-100 environmental conditions (NFRC, 2010). The convective heat transfer coefficient in the cavity is computed with the following equation (Athienitis, 1999; Nourozi et al., 2020):

$$\mathrm{h_{c,cav}} = \mathrm{Nu_A} \cdot \frac{\mathrm{k_{air}}}{\mathrm{L_{cav}}} \tag{3.6}$$

$h_{c,cav}$ is the convective heat transfer coefficient within the window cavity, Nu_A is the Nusselt number based on two different aspect ratios of height to cavity length, k_{air} is the thermal conductivity of air, and L_{cav} is the cavity length between surfaces. The cavity lengths within the windows at the FBL are fixed and to find the Nusselt number and thermal conductivity within the glazing, the following correlations are used (El Sherbiny, 1982):

$$\mathrm{Nu}_{80} = (1 + (0.0227 \cdot (\mathrm{Ra})^{0.438})^{18})^{1/18} \tag{3.7}$$

$$\mathrm{Nu}_{40} = (1 + (0.0303 \cdot (\mathrm{Ra})^{0.402})^{11})^{1/11} \tag{3.8}$$

Two Nusselt correlations are given based on two aspect ratios (80 and 40) present in the windows of test cell 4. The subscripts 80 and 40 represent the aspect ratio of (H_{win}/L_{cav}) and Ra is the Rayleigh number:

$$\mathrm{Ra} = 2.737 \cdot (1 + 2 \cdot \mathrm{a})^2 \cdot \mathrm{a}^4 \cdot (\mathrm{T_h} - \mathrm{T_c}) \cdot \left(\frac{\mathrm{L_{cav}}}{\mathrm{mm}}\right)^3 \cdot \mathrm{p}^2 \tag{3.9}$$

$T_m = (T_h - T_c)$ is the mean temperature across the cavity between the hot surface (T_h) and cold surface (T_c) in K, a is a factor given by $a = (100\ °C)/(T_m)$, and p is pressure (atm). Finally, the thermal conductivity of the air in the cavity is calculated with the following equation (Athienitis, 1999):

$$\mathrm{k_{air}} = \frac{0.002528 \cdot \mathrm{T_m}^{1.5}}{\mathrm{T_m} + 200} \tag{3.10}$$

The radiative heat transfer coefficient term can be calculated using the equation below, with ε_i and ε_j representing the emissivity of each glazing:

$$\mathrm{hr_{cav}} = \frac{4 \cdot \sigma \cdot \mathrm{T_m^3}}{\left(\frac{1}{\varepsilon_\mathrm{i}} + \frac{1}{\varepsilon_\mathrm{j}} - 1\right)} \tag{3.11}$$

To calculate the convective heat transfer coefficient on the exterior of the building, the following equation is used, assuming a minimum of 5 $\mathrm{W/m^2}$ occuring in still air:

$$h_{c,ext} = \max\left[5, \frac{8.6 \cdot V^{0.6}}{L^{0.4}}\right] \quad (3.12)$$

V represents the wind speed and L represents a characteristic length (Duffie et al., 2020). The convective thermal resistance may then be calculated for the exterior, or between the cavities, or for the interior in equation (3.13).

$$R_c = \frac{1}{A_{win} \cdot h_x} \quad (3.13)$$

h_x represents the convective heat transfer coefficient and the subscript 'x' may represent the exterior, window cavity, or interior of the building. Conductive thermal resistance through the glass may be calculated by the following equation:

$$R_{cond} = \frac{L_g}{A_{win} \cdot k_g} \quad (3.14)$$

Bifacial PV Production

Before evaluating the PV production of the STPV window, the relevant solar geometry must be calculated for the FBL, which is a south-facing building in Montreal, Quebec. Hottel's clear sky model (Hottel, 1976) is used to estimate the available solar radiation through the atmosphere and on the window's surface which is described in detail in Appendix C. Using the glazing properties, blind properties, and tilt angle, the reflected solar radiation incident on the back surface of the PV cell can be estimated. The total solar radiation incident on the front side of the PV cell, $S_{t,front}$, must be added to the solar radiation incident on the back side of the PV panel, $S_{t,back}$, for a total electricity production.

$$S_{tot} = S_{t,front} + S_{t,back} \quad (3.15)$$

Ray-tracing techniques were used (Chan & Tzempelikos, 2012), and assumptions were made to use one-ray transmitted to the blind layer and reflected to the back side of the PV cell. The

following assumption was made to calculate the back-side incident solar radiation, for a triple glazed and quadruple glazed window, respectively. τ_i is the transmittance of glazing layer 'i', ρ_j is the reflectance of glazing layer 'j', and ρ_{blind} is the reflectance of the blind.:

$$S_{t,back,TG} = S_{t,front} \cdot \left[(\tau_i \cdot \rho_j) + (\tau_i \cdot \tau_{i+1}^2 \cdot \rho_{blind})\right] \quad (3.16)$$

$$S_{t,back,QG} = S_{t,front} \cdot \left[(\tau_i \cdot \rho_j) + (\tau_i \cdot \tau_{i+1}^2 \cdot \rho_{j+1}) + (\tau_i \cdot \tau_{i+1}^2 \cdot \tau_{i+2}^2 \cdot \rho_{blind})\right] \quad (3.17)$$

Estimating power generation of the STPV was completed with Evans' Model (Evans, 1981), King's Model (King et al., 2004), and (ASHRAE, 2019). This is a simple model for evaluating the electrical production of PV modules using meteorological data.

$$P_{mod} = c \cdot \eta_{ref} \cdot \left(1 + \mu_{P,mp} \cdot (T_{cell} - T_{ref})\right) \cdot S_{tot} \cdot A_{PV} \quad (3.18)$$

P_{mod} is the electrical output of the PV modules (W), c is a unit correction coefficient (1), η_{ref} is the electrical efficiency of the reference conditions (incident radiation of 1000 W/m^2, PV module temperature of 25 ºC, and solar spectrum air mass of 1.5), $\mu_{P,mp}$ is the temperature coefficient at the maximum power point ($°C^{-1}$), T_{cell} and T_{ref} represent the operating cell temperature and reference temperature (25 ^oC), respectively. S_{tot} represents the total incident irradiance (W/m^2) and the total PV area is A_{PV} (m^2). To calculate T_{cell}, the following equation is used:

$$T_{cell} = T_{back} + \left({}^{S_{tot}}/_{S_{ref}}\right) \cdot \Delta T \quad (3.19)$$

T_{back} is the back-surface PV module temperature (^oC). S_{ref} is the reference solar irradiation ($1000 W/m^2$) and ΔT is the difference in temperature between the cell and the back surface at S_{ref}, which is given as 11 K for triple glazed STPV windows (ASHRAE, 2019). To find T_{back}, the equation below is used:

$$T_{back} = c_1 \cdot S_{tot} \cdot e^{(a+b \cdot V_{met})} + T_a \quad (3.20)$$

c_1 is a unit correction coefficient of 1 $\frac{m^2 \cdot K}{W}$, a and b $(^m/_s)^{-1}$ are empirically determined coefficients. For a triple glazed PV window, $a = -2.88$ and $b = -0.0319$ $(^m/_s)^{-1}$ (ASHRAE, 2019). The ambient temperature is represented by T_a (ºC) and the exterior wind speed at standard height of 10 m is V_{met} (m/s). Finally, to find the final electrical output of the PV system (P_{elec}), we must consider the losses, where $(1 - EL_1) \cdot (1 - EL_2) \cdots (1 - EL_i)$ is the electric losses due to factor i. The electrical losses considered in this methodology were based on ASHRAE (2019), and they include shading, soiling, light induced degradation, inverter, mismatch, and wiring.

$$P_{elec} = [(1 - EL_1) \cdot (1 - EL_2) \cdots (1 - EL_i)] \cdot P_{mod} \quad (3.21)$$

Table 3.5. Electrical Losses for STPV Window

Loss Description	Typical Range	Modelling Value
Shading	0.00-1.00	0.05
Soiling	0.02-0.25	0.05
Light Induced Degradation	0.01-0.10	0.01
Inverter	0.04-0.07	0.04
Mismatch	0.02-0.03	0.02
Wiring	0.01-0.02	0.01

The integrated venetian blinds are assumed to be highly reflective, therefore, can increase the potential incident solar radiation on the back side of the bifacial PV cells. The integrated blinds are not only controlled for improving the energy generation of the bifacial PV cells, but for optimal transmission of solar gains and daylight.

Transmittance of Window with Venetian Blinds

The transmittance of the blind layer can be calculated for both clear and diffuse days using the method from (Athienitis & Tzempelikos, 2002). The transmittance functions in this method were

determined for a double-glazed window with venetian blinds between the glazing layers. The blind slats in this study were aluminum having dimensions of 35mm wide and 6mm thick at the center. The slat dimensions and material in this study (width = 34.9 mm, thickness = 6.4 mm, aluminum) are similar, therefore, this method for calculating blind transmittance was deemed acceptable. For this study an assumption of multiplying the function by an additional transmittance value for each additional glazing layer is used. Shown below in equation (3.22) and (3.23) is the transmittance for a cloudy and clear day, respectively.

$$\tau_{vis}^{cld}(\beta) = \frac{4.5 \cdot 10^{12} \cdot \beta^{-6}}{e^{335/\beta} - 1} \cdot \left(\tau_g^{n-2}\right) \tag{3.22}$$

$$\tau_{vis}^{clr}(\beta, \theta) = 0.55 \cdot e^{-(\beta-80)^2/1900} \cdot (-4.917 \cdot 10^{-7} \cdot \theta^4 + 9 \cdot 10^{-5} \cdot \theta^3 - 5.67 \cdot 10^{-3} \cdot \theta^2 + 0.13 \cdot \theta - 4.37 \cdot 10^{-3}) \cdot \left(\tau_g^{n-2}\right) \tag{3.23}$$

β is the blind tilt angle, θ is the incidence angle, and τ_{glass}^{n-2} represents the transmittance of the glazing where the superscript 'n' is the number of glazing layers (e.g., TG =3). It is assumed that each additional glazing layer has the same properties. Figure (3.7) shows a schematic of the venetian blinds with 'n' glazing layers. The dashed box represents the transmittance due to a double glazed venetian blind window.

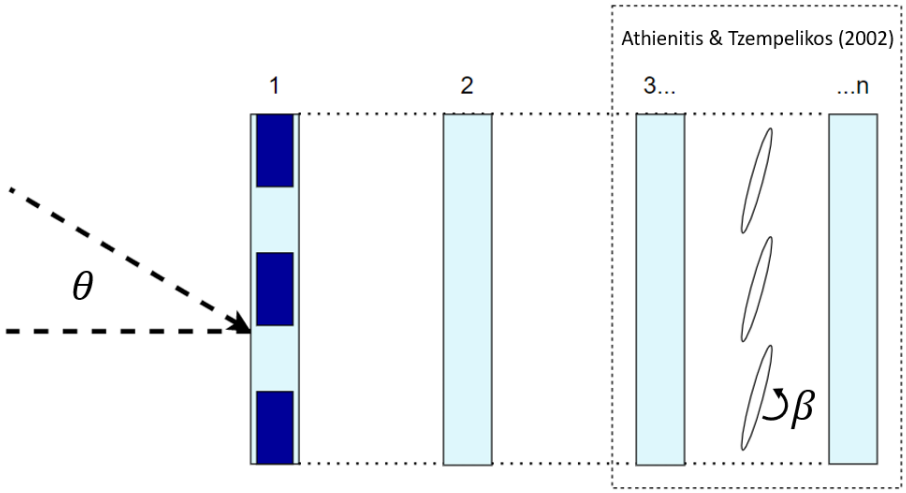

Figure 3.7. Schematic of 'n' glazing layers for equation (3.22 & 3.23).

3.2.2. Modelling of Floor Heating System

As per Figure (3.5) the RC model uses two capacitances within the concrete, but the order of the model may be further increased. Comparisons 2nd, 3rd, and 4th order concrete models will be compared for their accuracy in predicting room air, floor surface, and wall surface temperatures. Shown in figure (3.8) are the hydronic radiant floor RC networks with order two and three.

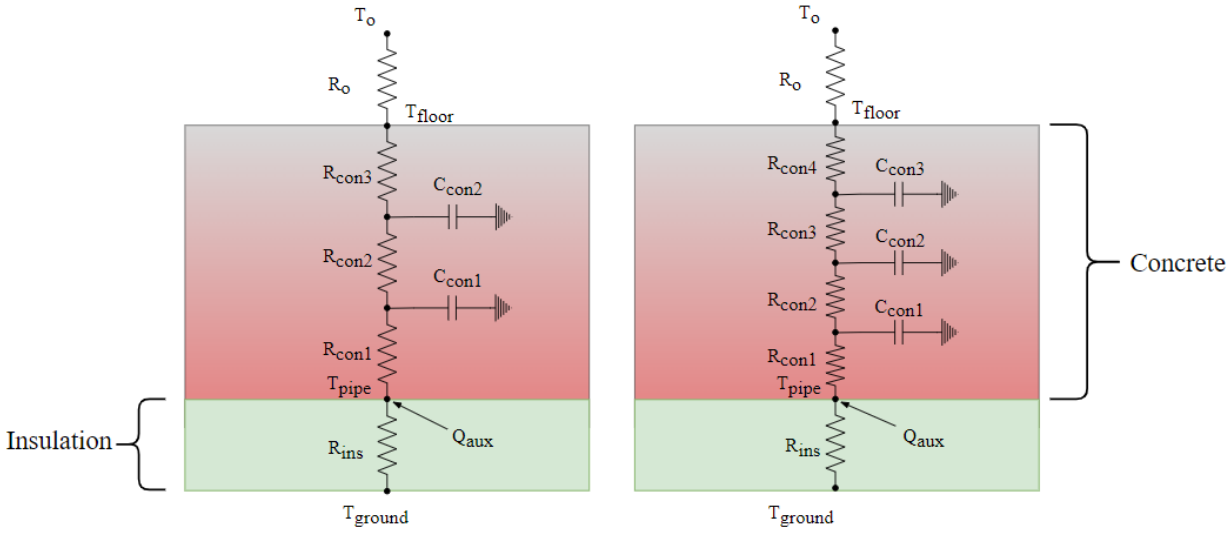

Figure 3.8. RC model of concrete layer discretized into 2 (left) and 3 (right) layers.

Heat Transfer Coefficients of Radiant Floors

This study considers radiant floors in the heating season, therefore, throughout a typical workday, the floor is typically warmer than the room air. Heat flow is assumed to be upward from the horizontal surface and assumed to be turbulent. Equation (3.24) is used for the convective heat transfer coefficient of the floor. (Athienitis & O'Brien, 2015).

$$\mathrm{h_{cf}} = 1.52 \cdot (\mathrm{T2} - \mathrm{T1})^{1/3} \tag{3.24}$$

$T2$ is the floor surface temperature and $T1$ is the air temperature in the thermal zone, with units of $°C$. The radiative heat transfer coefficient in equation (3.25) uses the factor, $4 \cdot (Tm)^3$, as a linearized parameter, which must have units of K. The emissivity of concrete is given by ε, which is assumed to be 0.92 (del Coz Diaz et al., 2014), meaning it is effective in absorbing and emitting radiant heat, $\sigma = 5.67 \cdot 10^{-8} \left(W/(m^2 \cdot K^4)\right)$ is the Stefan-Boltzmann constant, and $T6$ is the average surface temperature of the unheated walls.

$$\mathrm{h_{rf}} = \varepsilon \cdot \sigma \cdot 4 \cdot (\mathrm{Tm})^3 = \varepsilon \cdot \sigma \cdot 4 \cdot \left(\frac{\mathrm{T2} + \mathrm{T6}}{2}\right)^3 \tag{3.25}$$

Similarly, for the radiant heat exchange between the floors and the window surface equation (3.25) will be used, except $T7$ will substitute for $T6$.

3.2.3. Occupant Model for Thermal Comfort

The PMV Model with the CBE Comfort Tool (Tartarini et al., 2020; ASHRAE, 2010a) is used to determine the interior thermal environment. The occupant parameters assumed for this model include:

Table 3.6. Occupant Parameters for Thermal Comfort

Parameter	Activity	Value
Metabolic Rate (M)	Typing in an office	1.1 met (64 W/m^2)
Interior Air Speed (v)	-	0.1 m/s
Clothing insulation (Icl)	Winter Clothing	1.0
Occupancy	Typical Working Hours	8AM-5PM

Plane Radiant Temperature

The plane radiant temperature, T_{pr}, equation is used to estimate the mean radiant temperature, which approximates the view factor in an enclosure and requires inputs of all interior surfaces. Using the surface temperature values in the RC model described above we can estimate the plane radiant temperature. This equation assumes identical view factors for parallel surfaces (ASHRAE, 2017; Guo et al., 2019) and is determined by:

$$\mathrm{T_{pr}} = \frac{\big(0.18 \cdot (\mathrm{T6} + \mathrm{T2}) + 0.22 \cdot (\mathrm{T6} + \mathrm{T6}) + 0.30 \cdot (\mathrm{T7} + \mathrm{T6})\big)}{2 \cdot (0.18 + 0.22 + 0.30)} \qquad (3.26)$$

$T2$ represents the floor surface, $T6$ is the unheated surfaces (interior walls), and the window surface is $T7$. This method avoids geometric intricacies related to calculating the view factor for multiple positions and orientations in an enclosure (Guo et al., 2019).

Operative Temperature

The equation for T_{op} is shown in equations (3.27) and (3.28). For cases of low metabolic rates between 1.0-1.3 (58.2-75.66 $\frac{\mathrm{W}}{\mathrm{m^2}}$), air velocities less than 0.2 $\mathrm{m/s}$, and when not in direct sunlight equation (3.28) is an acceptable approximation of the operative temperature (ASHRAE, 2010).

$$\mathrm{T_{op}} = \left(\frac{\overline{\mathrm{h_c}} \cdot \mathrm{T1} + \overline{\mathrm{h_r}} \cdot \mathrm{T_{pr}}}{\overline{\mathrm{h_c}} + \overline{\mathrm{h_r}}} \right) \tag{3.27}$$

$$\mathrm{T_{op}} = \frac{\left(\mathrm{T1} + \mathrm{T_{pr}}\right)}{2} \tag{3.28}$$

The operative temperature, T_{op}, is an average of the air temperature, $T1$, and the plane radiant temperature, T_{pr}, which is then weighted by the average of respective convective and radiant heat transfer coefficients, $\overline{h_c}$ and $\overline{h_r}$.

3.2.4. Daylighting Model

Radiosity Method

Using the measured illuminance incident on the window and transmitted through the fenestration system we can use the radiosity method to validate the measured workplane illuminance. The workplane height, H_{wp}, is 0.8 m and the sensor distance from the window, D_{sen}, is 1.55 m from the window. The terms D_{L1} and D_{L2} denote the distance from the window to each luminaire installed on the ceiling. Figure (3.9) shows a schematic of sensor installation for daylighting and D_{L1} and D_{L2} are the distances of the luminaires from the window:

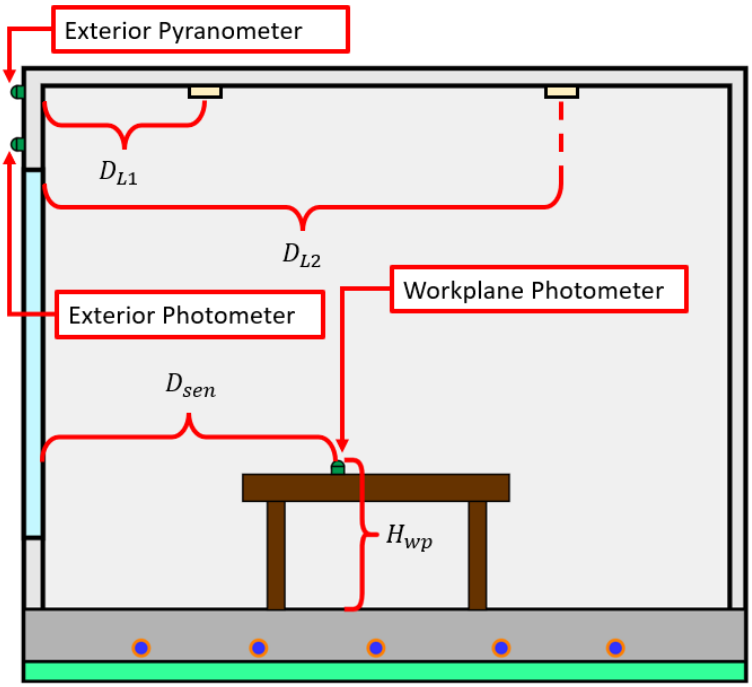

Figure 3.9. Schematic luminaire and sensor locations.

This method requires the calculation of view factors between surfaces and assumes diffuse reflecting surfaces (Hughes et al., 2013; Chan & Tzempelikos, 2012). The following equation is the general form of the radiosity method, in terms of luminous exitance (lm/m^2):

$$\mathrm{M_f} = \mathrm{M_{oi}} + \rho_\mathrm{i} \cdot \sum_\mathrm{j} \mathrm{M_j} \cdot \mathrm{F_{ij}} \tag{3.29}$$

M_f is the total luminous exitance of surface'i' (lm/m^2), M_{oi} is the initial luminous exitance of surface 'i', ρ_i is the diffuse reflectance of surface 'i', M_j is the total luminous exitance of surface 'j', and F_{ij} is the view factor between surfaces 'i' and 'j'. The following figure shows the 3-surface radiosity model, for modelling exitance exchange between interior surfaces:

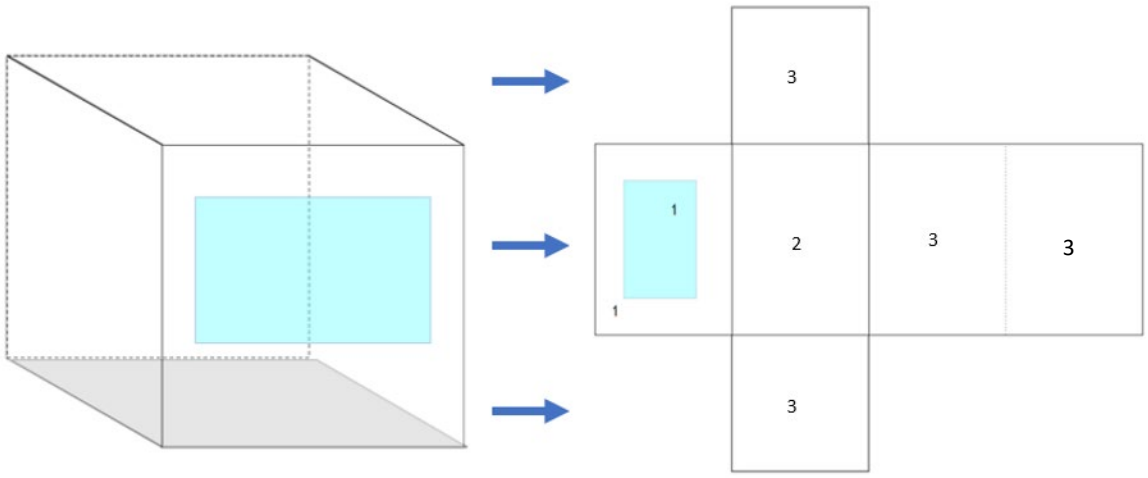

Figure 3.10. 3-surface enclosure for Radiosity method.

Using the 3-surface model, we assume surface 1 is the window and window-wall, surface 2 is the floor, and the remaining walls and ceiling are surface 3. The reflectance's of each surface, the effective reflectance's, and the calculated view factors is found in table (3.7). The formula to calculate the view factors can be found in Appendix C.

Table 3.7. Surface Reflectance's, Sensor Location and View Factors

Surface Reflectance	**Value**	**View Factor**	**Value**
$\boldsymbol{\rho_{glass}}$	0.15	**F11**	0
$\boldsymbol{\rho_{floor}}$	0.25*	**F12**	0.19
$\boldsymbol{\rho_{wall}}$	0.65*	**F13**	0.81
Effective Reflectance	**Value**	**F21**	0.22
$\boldsymbol{\rho_1}$	0.35	**F22**	0
$\boldsymbol{\rho_2}$	0.25	**F23**	0.78
		F31	0.23
$\boldsymbol{\rho_3}$	0.65	**F32**	0.19
		F33	0.59

**CEN (2011).*

To find the final luminous exitances of each surface, we must calculate the radiosity matrix with the following equations (Goral et al. 1984):

$$R^{-1} = \begin{bmatrix} 1-\rho_1 \cdot F_{11} & -\rho_1 \cdot F_{12} & -\rho_1 \cdot F_{13} \\ -\rho_2 \cdot F_{21} & 1-\rho_2 \cdot F_{22} & -\rho_2 \cdot F_{13} \\ -\rho_3 \cdot F_{31} & -\rho_3 \cdot F_{32} & 1-\rho_3 \cdot F_{33} \end{bmatrix}^{-1} \quad (3.30)$$

$$M_i = R^{-1} \cdot M_o \quad (3.31)$$

where the reflectance of each surface is given by ρ_i, with $i = 1 \cdots 3$ and $F_{i,j}$ is the view factor from surface i to j. Once the final luminous exitance of each surface is calculated, the average illuminances of each surface, E_i, and the illuminance at a specific point, E_p, can be found, where $c_{p,j}$ is the configuration factor from surface j to point p:

$$E_i = \sum_j F_{ij} \cdot M_j \quad (3.32)$$

$$E_p = \sum_j c_{p,j} \cdot M_j \quad (3.33)$$

Artificial Lighting

Upon calculating the workplane illuminance supplementary artificial light may be needed for specific times throughout the day. In the thermal zone presented luminaires are positioned along the center of the width in the room at 0.57 m and 2.37 m from the window. The luminaires installed at the FBL are Fortimo LED Strips with the following specifications:

Table 3.8. Luminaire Properties

Parameter	Value
Length	0.56 m (22”)
Initial Lumen Output (lm)	6120
Input Watts (W)	45.33
Efficacy (lm/W)	135

3.2.5. Model Calibration

The RC model was calibrated with inputs of ground temperature, Tg, adjacent zone interior temperature, Tin, exterior temperature, To, and solar radiation incident on the exterior of the window, S_{front}. Similarly, the daylighting model was calibrated with illuminance on the exterior of the window surface, E_{ext}. The exterior pyranometer and photometer were pre-calibrated from the manufacturer. The calibration constant for the pyranometer is -94.76 $\mathrm{W/m^2/mV}$ while the constant for the photometer is -6.13 $\mathrm{kLux/mV}$. The thermocouples were calibrated to the watts tekmar thermostat installed in each test cell. The thermostat gave room air temperature readings with an accuracy ±0.2 °C at 25 °C.

3.3. Optimal Control

Three systems in this study are controlled, the motorized venetian blinds, the hydronic radiant floor heating system, and the artificial lighting in the perimeter zone. The controlled variable for the venetian blinds is the blind tilt angle (β) and the air temperature in the room is controlled via temperature setpoint strategies (T_{sp}) in which the HRFH system will supply heating. The luminaires in the zone are controlled via dimming percentages. These systems are controlled to meet the targets of key performance indicators of energy performance and occupant comfort.

3.3.1 Motorized Venetian Blinds

Cut-Off Blind Control Strategy

Using equations (3.22) and (3.23) for window transmittance we can implement blind control strategies based on a desired goal (i.e., energy performance or occupant comfort). Two blind control strategies are considered in this thesis, the first being the “Cut-off” (CO) blind tilt angle strategy and is described in further detail in Athienitis & Tzempelikos, (2002). To calculate the optimum blind tilt angle, the profile angle ‘$d(n,t)$’ must be calculated for a specific time of day.

$$\mathrm{d(n,t)} = \tan^{-1}\left(\frac{\tan\left(\alpha(\mathrm{n,t})\right)}{\cos\left(\varphi(\mathrm{n,t})\right)}\right) \tag{3.34}$$

$\alpha(\mathrm{n,t})$ is the solar altitude on day 'n' at time 't' and $\varphi(\mathrm{n,t})$ is the solar azimuth angle on day 'n' at time 't'. The profile angle is then used to calculate the optimum blind tilt angle, on a clear day, to block direct beam solar radiation, β_{opt}^{clr}, shown in equation (3.35). When assuming the blinds have equal distance between them as blind length, a profile angle of $\mathrm{d(n,t)} > 45°$, will block all direct beam radiation from transmitting through the blind layer.:

$$\begin{gathered}\text{if } \mathrm{d(n,t)} > 45°\text{: } \beta_{\mathrm{opt}}^{\mathrm{clr}}(\mathrm{n,t}) = 90°; \\ \text{else: } \beta_{\mathrm{opt}}^{\mathrm{clr}}(\mathrm{n,t}) = 180° - 2 \cdot \mathrm{d(n,t)}\end{gathered} \tag{3.35}$$

Always Open Blind Control Strategy

Another blind control strategy considered in this thesis is an 'Always Open' (AO) method to allow a maximum number of solar gains and daylight to be transmitted through the blind layer and into the building. Based on the profile angle, $d(n,t)$, we can calculate a blind tilt angle to be parallel to the incoming solar radiation and daylight based on the horizontal blind tilt angle of $\beta_{horz}^{blind} = 90°$. A schematic of the always open blind control strategy is shown in figure (3.11) below the following equation.

$$\beta_{AO}^{blind} = 90° - d(n,t) \tag{3.36}$$

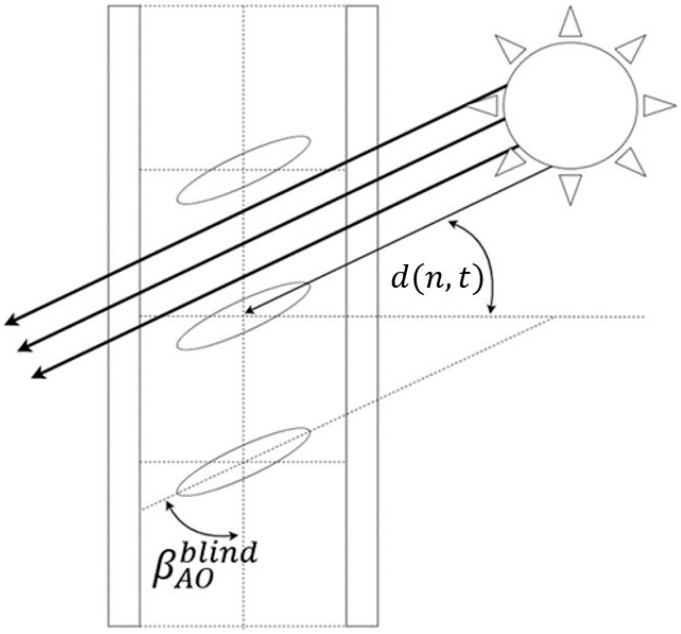

Figure 3.11. Schematic of always open blind strategy based on the profile angle and horizontal blind position.

Combinations of these two blind control strategies may be employed throughout the day to meet the targets of key performance indicators. For example, on clear days the AO strategy may employed during peak demand periods to maximize passive heating during this time. During the middle of the day and high solar radiation periods, the CO strategy may then be employed to maintain occupant comfort. Different combinations of these can then be implemented to improve passing heating and lighting while avoiding discomfort, based on the exterior conditions.

3.3.2. Hydronic Radiant Floor Heating

Temperature setpoint strategies were implemented into the model to achieve the key performance indicators. Strategies to meet energy efficiency (i.e., nighttime setbacks) and energy flexibility (i.e., preheating) are implemented into the RC model based on the air temperature and floor surface

temperature. Using equation (3.3) for q_{aux} we can apply heating to the radiant floor when the air temperature drops below the dead-band (db) that is programmed. Furthermore, the maximum floor surface temperature for thermal comfort is 29 °C (ASHRAE, 2010a), therefore, heating is shut off if the floor surface temperature is above a specified temperature. The hydronic floor supply temperature was low at 43 °C and based on equation (3.1) a maximum heating input is 550 W:

Table 3.9. Auxiliary Heating Control of the Hydronic Floor

Parameter	Dead-band (°C)	Condition		Output (W)
q_{aux}	0.25	$(T_{sp} - T_{1,p}) > 0.25$	min	q_{max} / $Kp \cdot (T_{sp} - T_{1,p})$
	2.00	$(29\ °C - T_{2,p}) < 2$	0	

Thermal Response Times of Radiant Floors at the FBL

As the Biot number condition is not usually met with larger thermal masses (Ning et al., 2017) and radiant systems with a lower thermal conductivity, thermal response times must be calculated via response curves. When controlling for energy flexibility, we can use these thermal response times to set a preheating duration time specific to the thermal mass volume, to simultaneously minimize the daily heating load. Shown in Figure (3.12) are the thermal response times of two slabs installed at the FBL having different thicknesses.

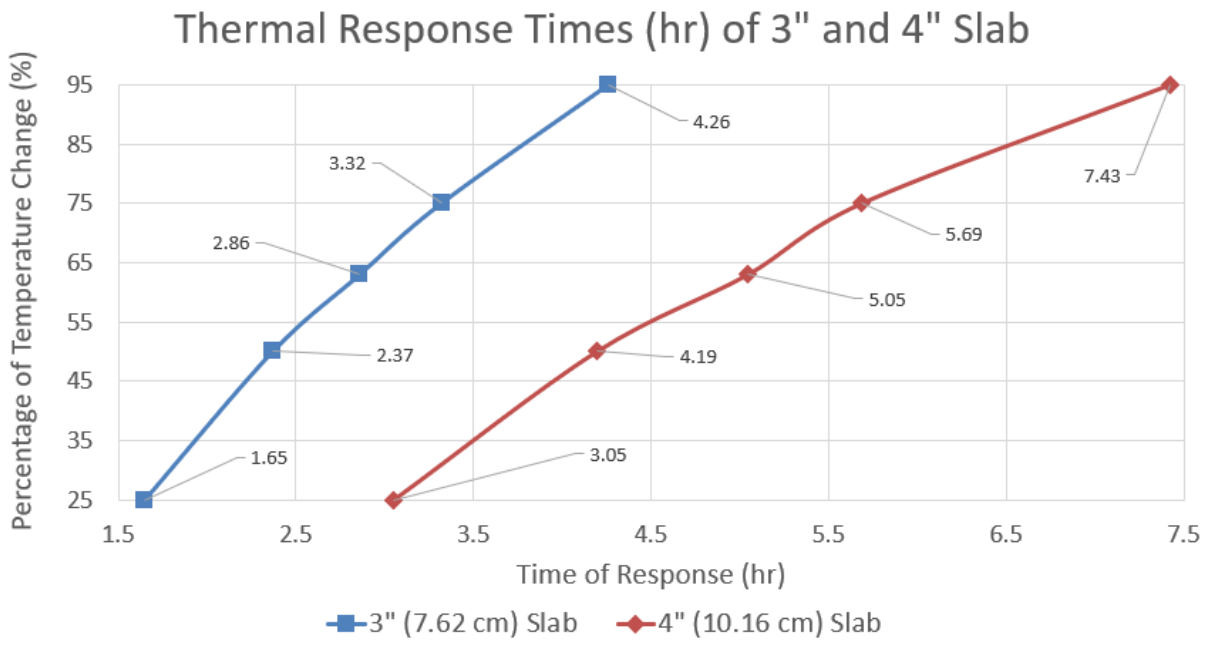

Figure 3.12. Thermal response times of a 3" (7.62 cm) and 4" (10.16 cm) slab.

With lightweight concrete, the thermal response times of the radiant floor system requires high preconditioning periods. Figure (3.12) was determined through experimental work and shows the response times of a 3" (7.62 cm) and 4" (10.16 cm) radiant floor.

For the radiant floor archetype, with the pipe location at the bottom of the slab, we can preheat the slab before the peak demand periods of 6-9AM in Quebec to provide acceptable thermal storage and minimize auxiliary heating in this period while maintaining thermal comfort for occupants. In this case study, we increase the setpoint a few hours before this peak period, which will ultimately increase the heating load for this time and remove any required heating for the peak demand period due to the heat stored in the concrete slab (Candanedo et al. 2022).

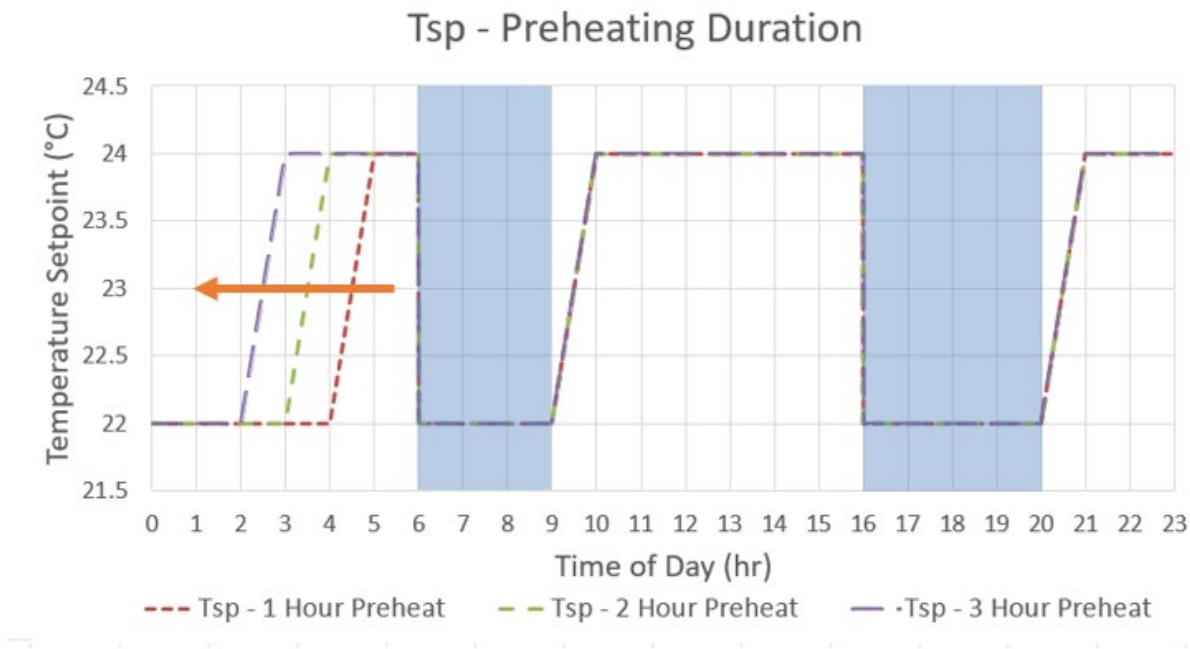

Figure 3.13. Temperature Setpoint Strategies with different morning preheat durations.

Preheating strategies for different durations before each peak demand period will be assessed for their energy flexibility and energy efficiency benefits. The red curve shows a preheating event for 1 hour before the peak period, while the green and purple curves show preheating strategies for 2 and 3 hours, respectively. The orange arrow indicates an increasing preconditioning period to be evaluated and similar strategies will be tested before the evening peak period. Highlighted in blue is the morning and evening peak demand periods of Quebec.

Near Optimal Temperature Setpoint Strategies

Jalilov & Athienitis (2021) developed temperature setpoint strategies based on different environmental clusters, such as exterior temperature and clearness index, for both energy flexibility and efficiency benefits, by using k-means clustering (Hartigan & Wong, 1979). Exterior temperature was clustered into mild, cold, and very cold design days, while the clearness index was clustered into cloudy, semi-cloudy, and clear days. These temperature setpoint profiles will be assessed in this model to test their applicability in perimeter thermal zones. Figure (3.14) shows

examples of three strategies for a cold day in different clearness conditions. Temperature setpoint strategies developed for all scenarios can be found in Appendix B.

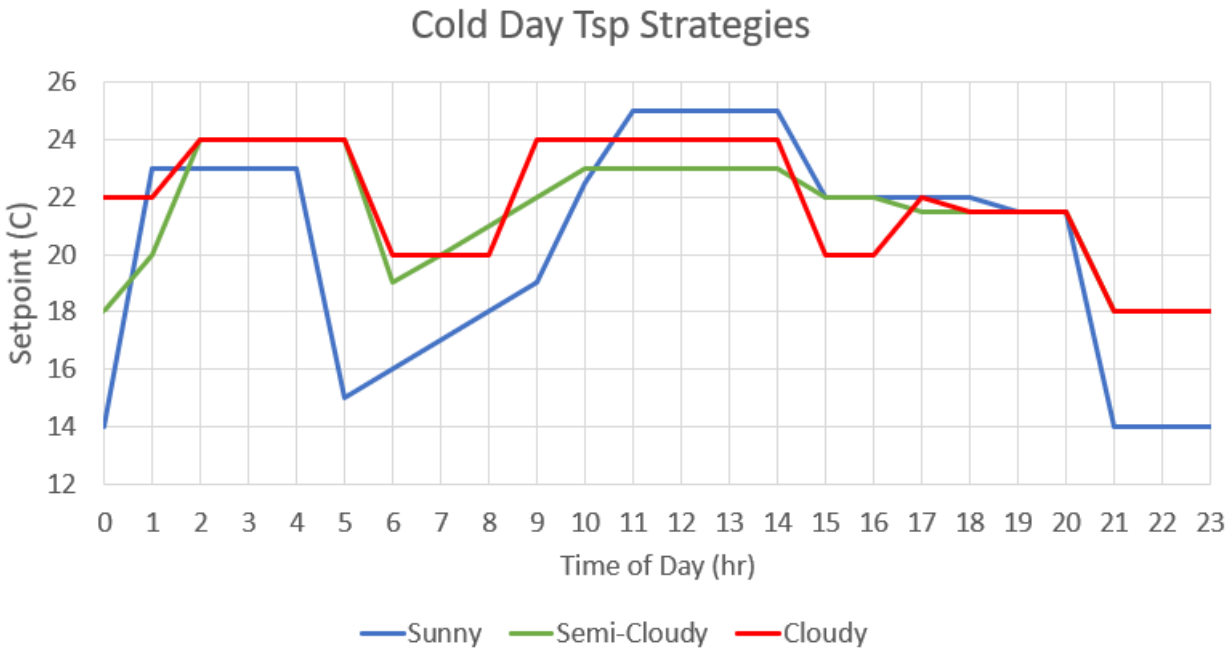

Figure 3.14. Tsp Strategies for a Cold Day for Different Environmental Conditions.

3.3.3. Controlled Lighting Loads

Using the control approach from Athienitis & Tzempelikos (2002) we can improve the energy flexibility of the perimeter zone by reducing the lighting load of a reference artificial lighting case. The reference case assumes the lamps may only be completely on or off. Flexible control assumes two dimming strategies:

1. The luminaires are dimmable at 0, 25, 50, 75, and 100%.
2. The luminaires are dimmable at 0, 12.5, 30, 47.5, 65, 87.5, and 100%.

A dimming of 0% means the lights are off. The output of the lighting energy used may then be calculated via the dimming percentage:

$$E_{art} = f_{dim}^{1} \cdot \frac{I_i^1}{L_1^2} \cdot \cos(\theta_1) + f_{dim}^{2} \cdot \frac{I_i^2}{L_2^2} \cdot \cos(\theta_2) \quad (3.37)$$

f_{dim} denotes the dimming fraction of the luminaire, I_i is the initial lumen output of the lamp, L_i is the linear distance from each lamp to the workplane point of interest. θ_i represents the angle from the normal of the lamp to the workplane measuring point, and the scripts 1 and 2 denote lamps 1 and 2.

3.4. Key Performance Indicator Assessment

The RC model developed for this study is programmed into python using the finite difference method to simulate transmitted solar radiation and daylight, temperature profiles, and daily and peak heating loads. Experiments were completed and data for exterior solar radiation, illuminance, ground temperature, adjacent zone temperature, exterior temperature, and relative humidity were used to calibrate the simulation model. Several experiments were completed on different days to collect data for different clusters of exterior conditions such as the available solar radiation and daylight (i.e., clear, semi cloudy, and cloudy days) and temperature (i.e., mild, cold, very cold days). The model was validated on a test completed from February 28th to March 2nd, which was a mild and cloudy day. Model verification will be explained in further detail in Chapter 4.

Energy Performance

Upon validating the RC model, different flexibility strategies will be simulated compared to a reference T_{sp} case of nighttime setback. Different preheating durations before the peak demand periods will be simulated to estimate the energy flexibility of the perimeter zone. One of the main objectives of this thesis is to calculate the energy benefits of these specific set of integrated building systems, in terms of energy flexibility and energy efficiency. The $\overline{BEFI}$ (kW) and $\overline{BEFIP}$ (%) quantify energy flexibility of the energy demand, when compared to a reference case (Athienitis

et al. 2020). Equations (3.38) and (3.39) were originally shown in Chapter 2 are reiterated for clarity:

$$\overline{\mathrm{BEFI}}(\mathrm{t},\mathrm{Dt}) = \frac{\int_{\mathrm{t}}^{\mathrm{t+Dt}} \mathrm{P_{ref}dt} - \int_{\mathrm{t}}^{\mathrm{t+Dt}} \mathrm{P_{flex}dt}}{\mathrm{Dt}} \tag{3.38}$$

$$\overline{\overline{\mathrm{BEFIP}}}(\mathrm{t},\mathrm{Dt}) = \frac{\int_{\mathrm{t}}^{\mathrm{t+Dt}} \mathrm{P_{ref}dt} - \int_{\mathrm{t}}^{\mathrm{t+Dt}} \mathrm{P_{flex}dt}}{\int_{\mathrm{t}}^{\mathrm{t+Dt}} \mathrm{P_{ref}dt}} \tag{3.39}$$

P_{ref} is the average power consumption of the reference case, P_{flex} is the average power consumption of the flexible, or near-optimal, case, Dt represents the duration of flexibility, which in this case will be the peak demand periods of 6-9AM and 4-8PM, and t is the onset of the flexibility window. To calculate the average power consumption during the peak demand periods we use the following equation, where n represents the number of timesteps during the flexibility window and the subscript 'case' represents the reference or flexible case:

$$\mathrm{P_{case}} = \frac{\sum_{\mathrm{t}}^{\mathrm{Dt}} \mathrm{q_{aux}}}{\mathrm{n}} \tag{3.40}$$

The daily heating loads may be calculated, where the subscript 'case' represents the reference or flexible case:

$$\mathrm{Q_{h,case}} = \int_{\mathrm{t}}^{\mathrm{t+Dt}} \mathrm{q_{aux}} \cdot \mathrm{dt} \tag{3.41}$$

The reduction in heating demand energy is calculated with the following equations, in terms of (W), (3.42), and (%), (3.43):

$$\overline{Q_h} = Q_{h,ref} - Q_{h,flex} \tag{3.42}$$

$$\overline{Q_h P} = \frac{Q_{h,ref} - Q_{h,flex}}{Q_{h,ref}} \cdot 100\% \tag{3.43}$$

$Q_{h,ref}$ represents the heating load of the reference control strategy case and $Q_{h,flex}$ is the heating load of the thermal zone subjected to the flexible case for energy efficiency or energy flexibility.

Workplane Illuminance

The metric of Useful Daylight Illuminance (UDI) categorizes clusters of illuminance ratings that are useful for occupants. Table 3.10. shows the UDI clusters for offices (IESNA, 2012; IESNA, 2000) from Chapter 2, for convenience:

Table 3.10. Useful Daylight Illuminance Ratings

Useful Daylight Illuminance	
Range	Rating
<300 Lux	Insufficient
300-500 Lux	Supplementary (Requires Top-up)
500-2500 Lux	Sufficient
>2500 Lux	Exceeded (Potential for Glare)

The useful daylight illuminance will calculate the percentage of time daylight may provide sufficient illuminance for a desired point on the workplane, given by the following equation:

$$UDI_E = \frac{n_E \cdot dt}{t_{wd}} \cdot 100\% \tag{3.44}$$

n_E represents the number of data points that achieved a sufficient workplane illuminance (500-2500 lux), dt the timestep used for measurements (6 min or 0.1 hr), and t_{wd} represents the total time of the workday. The radiosity method allows the simulation model to predict the workplane illuminance with the measured exterior illuminance on the surface of the window. To achieve a

sufficient workplane illuminance rating the luminaires in the zone may be controlled via dimming to 'top-up' the available daylight in the zone.

$$\mathrm{E_{suff}} = \mathrm{E_{dl}} + \mathrm{E_{art}} \tag{3.45}$$

When conducting experiments, the electrical lighting was turned off to obtain a daylighting reading for workplane illuminance. Using the initial lumen output and location of the luminaires with the location of the sensor (i.e., working point) the necessary lighting can be calculated based on different dimming levels of the installed luminaires. To calculate the energy to power the artificial lighting the following equation is used:

$$\mathrm{P_l(t)} = \mathrm{f^1_{dim}(t)} \cdot \mathrm{P_{L1}(t)} + \mathrm{f^2_{dim}(t)} \cdot \mathrm{P_{L2}(t)} \tag{3.46}$$

$P_l(t)$ is the power output of the lamps at time t and $P_{L1}(t)$ is the power output of lamp 1 at time t and $P_{L2}(t)$ is the power output of lamp 2 at time t. Equations (3.41-3.43) may be used to calculate the energy performance benefits when switching from the reference lighting case to the dimming control strategy. Occupancy hours are assumed to be from 8AM-5PM and the reference case for lighting energy flexibility will consider the lights to be undimmable (i.e., 0% or 100%) during these times. Controlling the artificial light in terms of dimming percentage combined with the daylight transmitted into the zone will be the flexible case.

Total Energy Flexibility

Equations (3.38 and 3.39) calculate the energy flexibility of the hydronic radiant floor, bifacial STPV, or the controlled lighting loads. Therefore, by combining the flexibility of these systems we can calculate a total $\overline{BEFI(P)}$ with $i = (HRFH, STPV, Lighting\ Load)$:

$$\overline{\mathrm{BEFI_{tot}}} = \frac{\sum_i \left(\int_t^{t+Dt} P_{ref} dt - \int_t^{t+Dt} P_{flex} dt \right)_i}{Dt} \tag{3.47}$$

$$\overline{\mathrm{BEFI(P)_{tot}}} = \frac{\sum_i \left(\int_t^{t+Dt} P_{ref} dt - \int_t^{t+Dt} P_{flex} dt \right)_i}{\left(\int_t^{t+Dt} P_{ref} dt \right)_i} \tag{3.48}$$

Thermal Comfort

In test cell 4 of the FBL, thermal comfort had to be measured with the dynamic heating in the zone. Thermocouples were added to each wall and window surface to calculate the T_{pr} (equation 3.26). A relative humidity sensor (Vaisala: Model HMD83D) was added to the zone to obtain the variable relative humidity. The operative temperature was calculated from equations (3.27) and (3.28), to evaluate the precision of both models described in (ASHRAE, 2010). When obtaining the operative temperature and RH, these data points were applied to figure (3.15), to assess if the zone is within the boundary limits of thermal comfort. These data points can be used to calculate a comfort percentage throughout the workday. The following figure was developed using the CBE Thermal Comfort Tool (Tartarini et al. 2020) and (ASHRAE, 2010a). It shows acceptable ranges of operative temperatures based on clothing levels of 1.0 clo and 0.5 clo are shown for a PMV range of ± 1, to allow less stringent constraints on energy performance compared to the acceptable PMV range given in (ASHRAE 2010a), ± 0.5. This thermal comfort model is calibrated with measured RH.

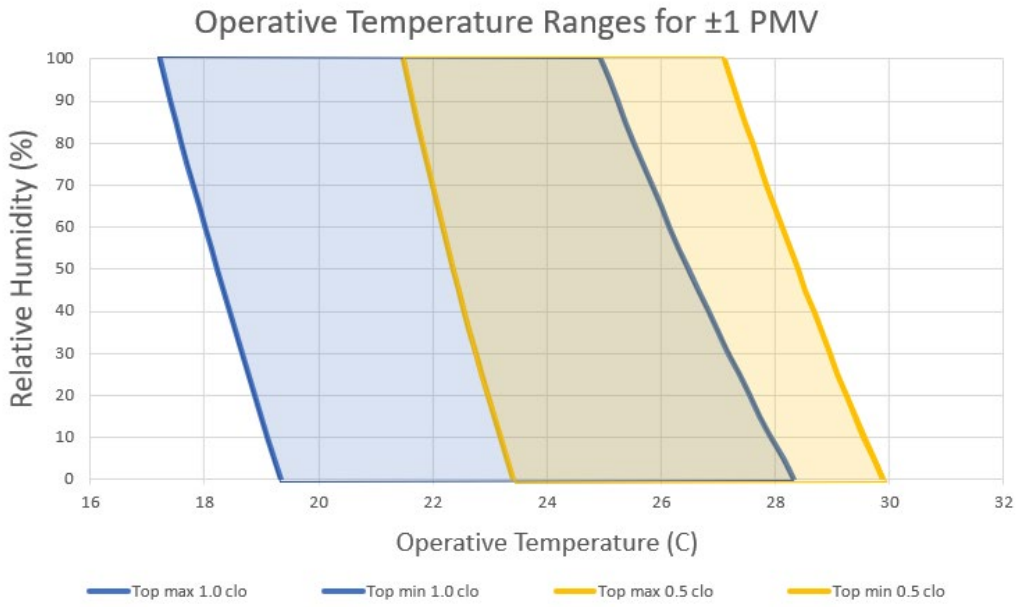

Figure 3.15. Operative Temperature Ranges for ±1 PMV. I_{cl} = 1.0 (blue), I_{cl} = 0.5 (yellow).

The blue coloured curves represent the upper and lower boundaries of the operative temperature for a clothing level of 1.0 clo, while the yellow boundaries represent 0.5 clo, at differing levels relative humidity. Like the UDI calculation, the percentage of time an occupant feels thermal comfort can be calculated for the workday.

$$\mathrm{PC} = \frac{\mathrm{n_{TC}} \cdot \mathrm{dt}}{\mathrm{t_{wd}}} \cdot 100\% \tag{3.49}$$

n_{TC} represents the number of data points within the boundaries of thermal comfort, dt is the timestep of measurements, which is 6 minutes, and t_{wd} is the total time of the workday.

Measuring Glare

The glare analysis in this study must be done experimentally with the method proposed by Nazzal (2005) which calculates the 'new' daylight glare index (DGI_n). Three vertical illuminance sensors are necessary for this method and the schematic for the sensors is shown in figure (3.16).

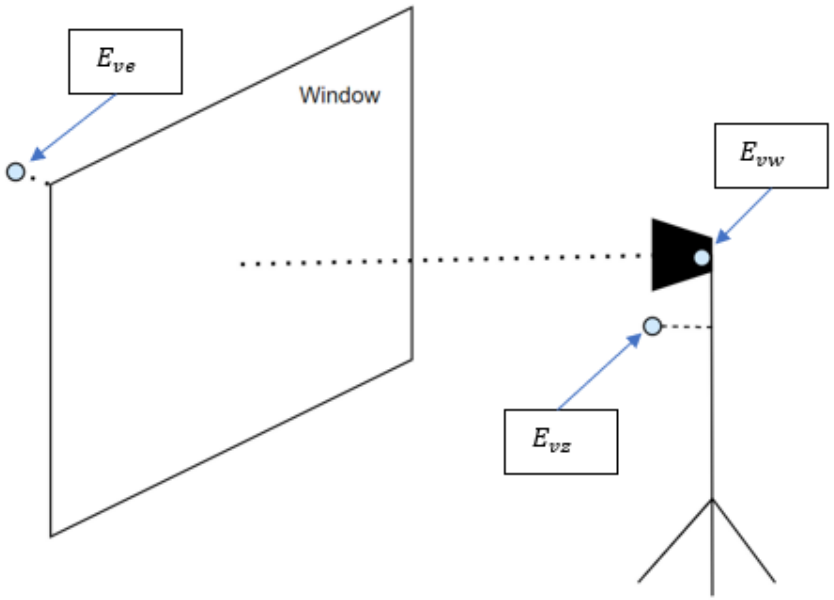

Figure 3.16. Sensor installation for glare analysis.

E_{vw} (lux) is the vertical illuminance reading from the window at the observation point, which is shielded to allow the sensor to 'see' only the window. E_{vz} (lux) is the vertical illuminance reading of the zone, which is unshielded to consider the reflected bounces of light due to the enclosure surfaces. E_{ve} is the vertical illuminance reading of the exterior photometer, which is unshielded. The illuminance values will be measured every minute for one hour and the DGI_n value will be calculated for this period to obtain the glare index over this testing period. This equation is repeated from chapter 2 for convenience, shown below:

$$\mathrm{DGI_N} = 8 \cdot \log_{10}\left(0.25 \cdot \left(\frac{\left[\sum\left(\mathrm{L_{ext}^2} \cdot \gamma_{\mathrm{pN}}\right)\right]}{\left[\mathrm{L_{surr}} + 0.07 \cdot \left(\sum\left(\mathrm{L_{win}^2} \cdot \omega_{\mathrm{N}}\right)\right)^{0.5}\right]}\right)\right) \qquad (3.50)$$

To calculate the solid angles ω_N and γ_{pN}, the width of the window, w_{win}, the height of the window, h_{win}, and the perpendicular distance from the window to the observation point, d_{win-p}, are required. Using these dimensions, we can find:

$$X = \frac{w_{win}}{2 \cdot d_{win-p}} \quad (3.51a) \qquad Y = \frac{h_{win}}{2 \cdot d_{win-p}} \quad (3.51b)$$

$$A = \frac{X}{\sqrt{(1 + X^2)}} \quad (3.51c) \qquad B = \frac{Y}{\sqrt{(1 + X^2)}} \quad (3.51d)$$

$$C = \frac{Y}{\sqrt{(1 + Y^2)}} \quad (3.51e) \qquad D = \frac{X}{\sqrt{(1 + Y^2)}} \quad (3.51f)$$

X and Y are the coordinates of the measuring sensor with respect to the window and the terms A, B, C, and D are used for the configuration factor calculation, which is given by the following equation:

$$\varphi_i = \frac{(A \cdot \tan^{-1}(B) + C \cdot \tan^{-1}(D))}{\pi} \quad (3.52)$$

Now, the solid angles ω_N and γ_{pN}:

$$\omega_N = \frac{(a \cdot b \cdot \cos(\tan^{-1}(X)) \cdot \cos(\tan^{-1}(Y)))}{d^2} \quad (3.53)$$

$$\gamma_{pN} = 2\pi \cdot \varphi_i \quad (3.54)$$

The solid angle estimation for ω_N is accurate to 1% for $X, Y < 0.5$ and accurate to 5% for $X, Y < 1$, while γ_{pN} is accurate to 1% for $X, Y < 0.1$ (Nazzal, 2005). To calculate the vertical luminances, three illuminance readings are required: the average vertical luminance of the window from the observation point, L_{win}, the average vertical luminance of the surroundings, L_{surr}, and the average exterior vertical luminance, L_{ext}. These variables are calculated with the following equations:

$$L_{win} = \frac{E_{vw}}{2\pi \cdot \varphi_i} \quad (3.55)$$

$$L_{surr} = \frac{E_{vz}}{\pi} \tag{3.56}$$

$$L_{ext} = \frac{E_{ve}}{\left(2(\pi - 1)\right)} \tag{3.57}$$

The glare perception scale initially shown in Chapter 2 is repeated below for convenience. The objective of this method is to maintain glare perception below 24 (Just Uncomfortable). This method tests for the worst-case scenario for glare perception.

Table 3.11. Glare Perception Scale with Daylight Glare Index.

DGI	Glare Criterion	DGI	Glare Criterion	DGI	Glare Criterion
<16	Imperceptible	20	Just Acceptable	26	Uncomfortable
16	Just Perceptible	22	Acceptable	28	Just intolerable
18	Perceptible	24	Just Uncomfortable	>28	Intolerable

Results for this glare testing method may be found in Appendix C rather than in the experimental results chapter.

Chapter 4: Experimental Results, Model Verification & Discussion

In this results chapter, we present the findings from our analyses of energy flexibility, energy efficiency, thermal comfort, and visual comfort. Results were achieved through the study of bifacial semi-transparent photovoltaic windows, motorized shading devices, and hydronic radiant floor heating systems in perimeter zones. Through data collection and analysis, we have obtained valuable insights into the performance of these technologies. Our analysis of energy flexibility reveals the system's responsiveness to different control strategies, showcasing its ability to adapt to varying energy demands. The energy efficiency analysis demonstrates significant energy

savings through the utilization of the PV window and control of the motorized shading system. Moreover, the evaluation of thermal comfort indicates the system's effectiveness in maintaining an acceptable PMV range while optimal energy performance was achieved. Additionally, the visual comfort analysis highlights the successful reduction of glare potential and enhancement of daylight availability through the shading system and PV window configurations. These results collectively validate the positive impact of the implemented technologies on building sustainability and occupant well-being.

4.1 Model Verification

To measure the accuracy of this model, a statistical evaluation was conducted. Equations (4.1) and (4.2) define the root mean square error ($RMSE$) and the coefficient of variation of root mean square error ($CVRSME$), respectively.

$$\mathrm{RMSE} = \sqrt{\frac{\sum_{i=1}^{n}(M_i - P_i)^2}{n}} \tag{4.1}$$

$$\mathrm{CVRSME} = \left(\frac{\mathrm{RMSE}}{M_m}\right) \cdot 100\% \tag{4.2}$$

The terms P_i represents the simulation prediction and M_i is the measured value, at timestep 'i'. M_m symbolizes the arithmetic mean of the measured values for the series of data analyzed. The denominator, 'n', represents the total number of data points for a sequence of data that was analyzed (Montgomery, 2013 and Tina et al., 2020).

Table 4.1. Models and their physical variables to be validated.

Model	Physical Variables	Error Metrics
RC Thermal Network Model	Room Air Temperature ($T1$), Floor Surface Temperature ($T2$), Average Wall Surface Temperature ($T6$)	RMSE
		CVRMSE
Daylighting Model	Workplane Illuminance (E_{wp})	RMSE
		CVRMSE

The RMSE and CVRMSE are outlined in table (4.2) for three different order models of the hydronic floor: 2C, 3C, and 4C. For the heating load, the difference between the daily total for measured and simulated will evaluate the error. The measured heating load may be found in figure (E.1) in Appendix E and the assumption associated with its calculation. The exact measured heating load was difficult to obtain, as there were issues with the software attached to the thermal energy meter. Therefore, based on the acquired data from the thermocouple attached to the PEX pipe, an assumption was made that heating was applied when this temperature was above 33 °C (see Figure E.2). Furthermore, to compensate for high fluctuations in the measured supply and return temperatures, a 5-point rolling average was applied to the data points to obtain the daily heating profile.

4.1.1 RC Thermal Network Model

This model was verified through experiment from February 28th – Mar 2nd. On March 2nd, a night setback temperature setpoint strategy was employed with a 22 °C setpoint from midnight to 6 am and 8pm to midnight. A setpoint increase of 2 degrees to 24 °C from 6am – 8pm. The model was initially programmed with a hydronic floor of order 2 (2C), providing a very good accuracy for the floor surface temperature and good predictions for the average wall surface and air temperatures. Initially, an exterior temperature sensor was installed outside of the FBL, but there were errors seen during periods of increased solar radiation. A radiation shield was applied to the

sensor, but it was decided that the error was too high, therefore, the data from the weather station at the Trudeau International Airport was used. See figure (4.1) for the exterior conditions.

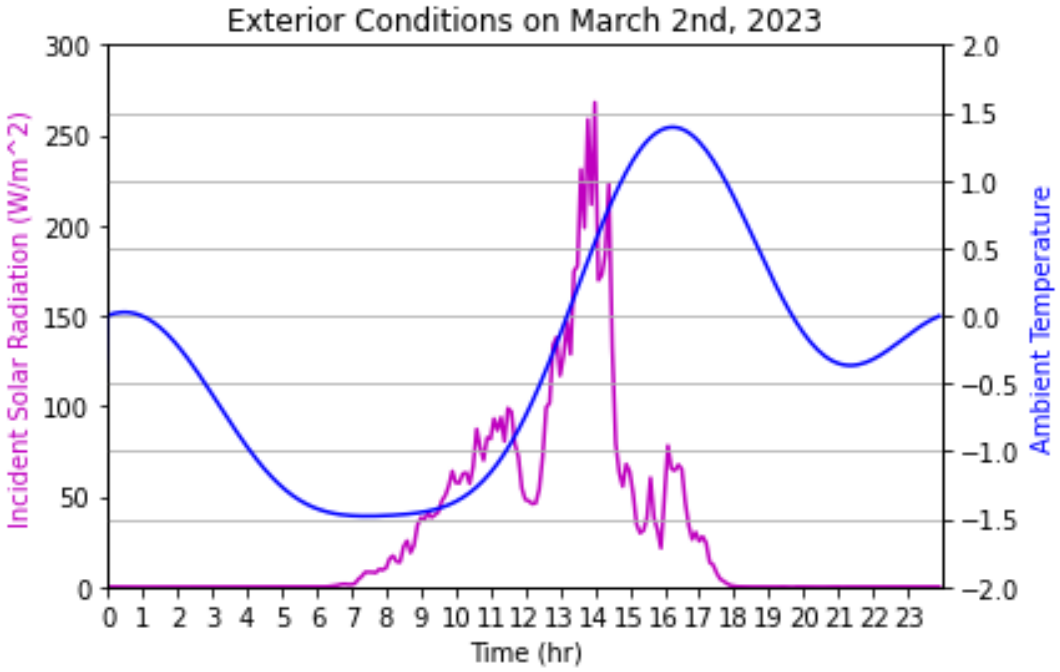

Figure 4.1. Exterior Conditions on March 2nd, 2023. Temperature and Horizontal Radiation.

Another assumption of this model includes an 'airtight' zone with ach = 0.75 h^{-1}, where this was due to central air heating dampers being closed, which also recycles the air. These dampers were closed as heating was applied with warm air being pumped into the room, resulting in inaccurate readings of air and wall temperatures where the study is focused on heating from the radiant floor. Low air exchange between the outdoors and most air changes between zones was assumed (Fisk & Faulkner, 1992). The minimum total air changes for the floor area in test cell 4 was calculated to be 0.378 h^{-1} (ASHRAE, 2010c). See figure (4.2) for the simulated and measured values for the air, floor surface, and average wall surface temperatures. The simulated values are the solid curves while the measured values are the dashed curves.

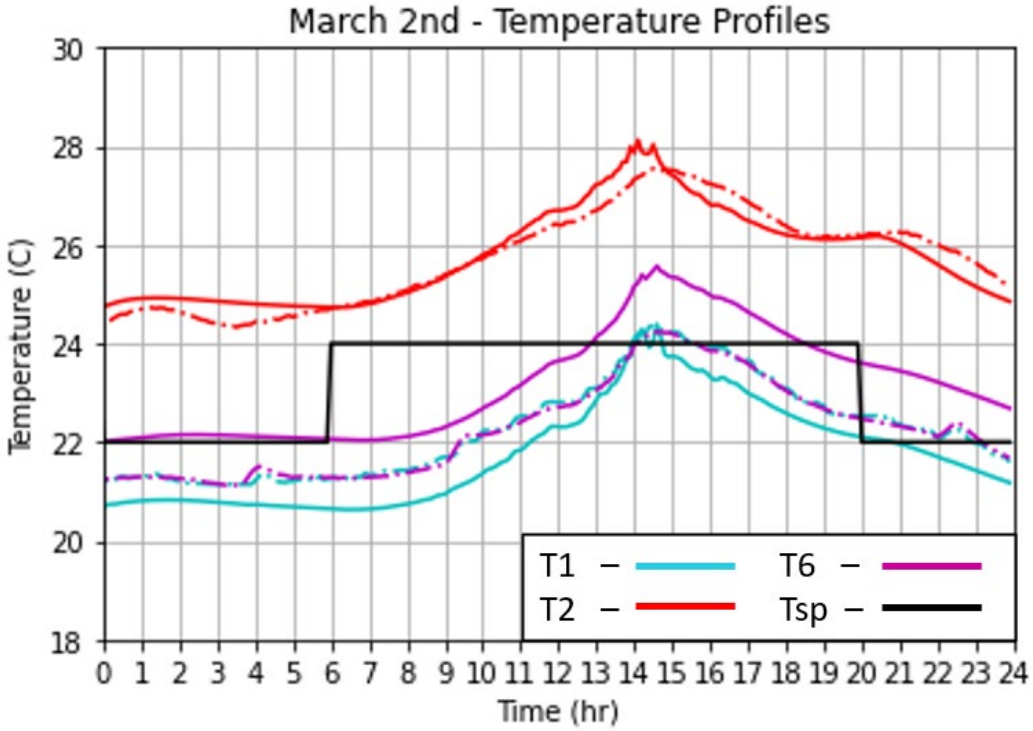

Figure 4.2. Model verification from Mar 2nd, 2023, experiment for Air, Floor, and Avg. Wall temperatures.

The RMSE for the floor temperature was 0.30 °C, while the CVRMSE was 1.14%. The room air temperature had a good prediction with an RMSE of 0.53 °C and a CVRMSE of 2.39%. The average wall surface temperature was overpredicted in the model but still considered acceptable, having an RMSE of 0.95 °C and a CVRMSE of 4.25%. The higher error for the average wall surface temperature was potentially due to the lumped unheated surfaces into node 6 in the model. Each wall surface had an adjacent zone with a unique configuration of the façade, materials, geometry, and occupancy, which may lead to distinctive thermal dynamics within each wall. The following table shows the goodness of fit when the concrete layer is discretized into 2 to 4 sublayers. As the order of the model increases the error for the air temperature decreased while the error for the floor surface and wall surface temperature increased. Therefore, the 2C model was used for simulations as it had the lowest collective errors.

Table 4.2. Goodness of fit for different Hydronic Radiant Floor models.

Parameter (T)	**Metric**	**Concrete Capacitances**		
		$2C$	$3C$	$4C$
Room Air	RMSE (°C)	0.53	0.49	0.49
	CVRMSE (%)	2.39	2.22	2.20
Floor Surface	RMSE (°C)	0.30	0.33	0.43
	CVRMSE (%)	1.14	1.29	1.66
Average Wall Surface	RMSE (°C)	0.95	1.02	1.04
	CVRMSE (%)	4.25	4.59	4.65

Heating Sources

Figure (4.3) shows the internal heating sources used for model verification and results. The heating load, q_{aux}, transmitted solar gains, q_{solar}, and validation internal gains, q_{int_val}, were the heating profiles found and used for model verification. The internal gains are shown for both verification and simulation models, as in the case of the March 2nd test the laptop was on for the entire experiment to collect data. For the simulation model, the internal gains, q_{int}, considers a person, lighting, and a laptop on for working hours of 8AM-5PM.

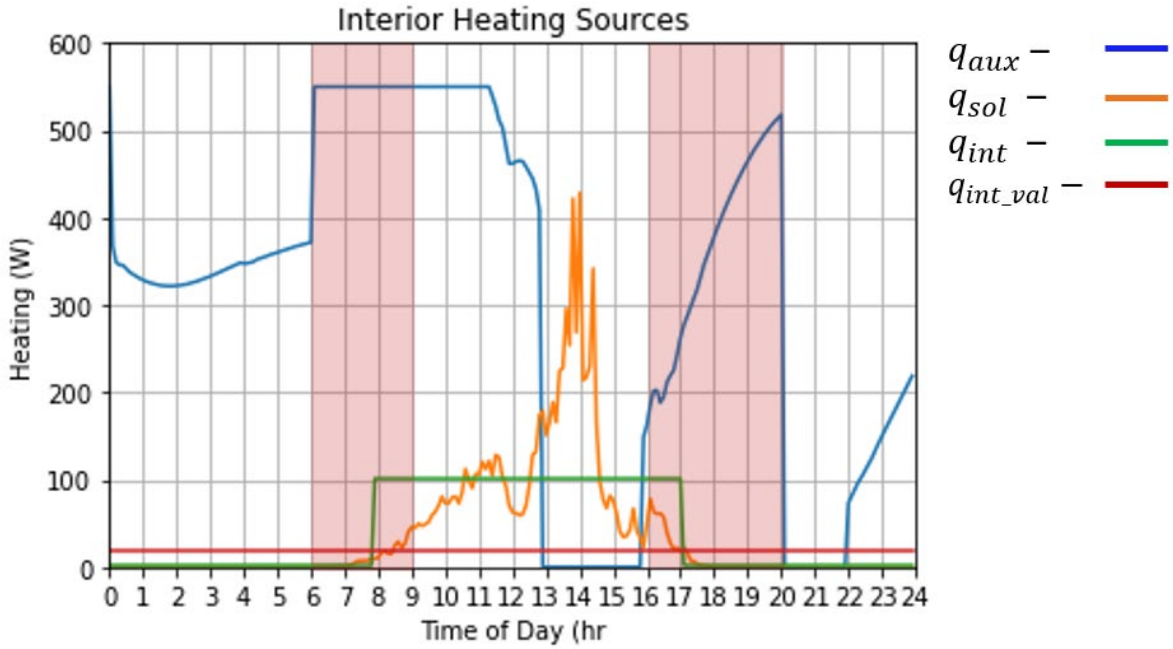

Figure 4.3. Interior heating sources: Auxiliary heating, solar gains, and internal gains.

The heating load in the simulation model had a daily load of 7.48 kWh and the measured daily load was 7.79 kWh, giving a difference of 0.31 kWh (3.98%). Increasing the order of the hydronic radiant floor RC model reduced the simulated daily heating loads causing higher error from the measured total, see table (4.3).

Table 4.3. Relative Error of Daily Heating Loads from different Concrete Models.

Metric	**Concrete Capacitances**		
	2C	**3C**	**4C**
Qh Measured (kWh)	7.79		
Qh Simulated (kWh)	7.48	7.23	7.04
Relative error (%)	3.98	7.19	9.88

4.1.2. Daylighting

Similarly, on March 2nd, daylighting tests were conducted to measure the workplane illuminance. To measure the validity of the model, daylighting hours from 7AM to 5PM were considered, rather than an entire day. This day had overcast exterior conditions for the majority of the day, before

1:30PM and after 2:30PM. Figure (4.4) below shows the exterior horizontal illuminance measured on the façade.

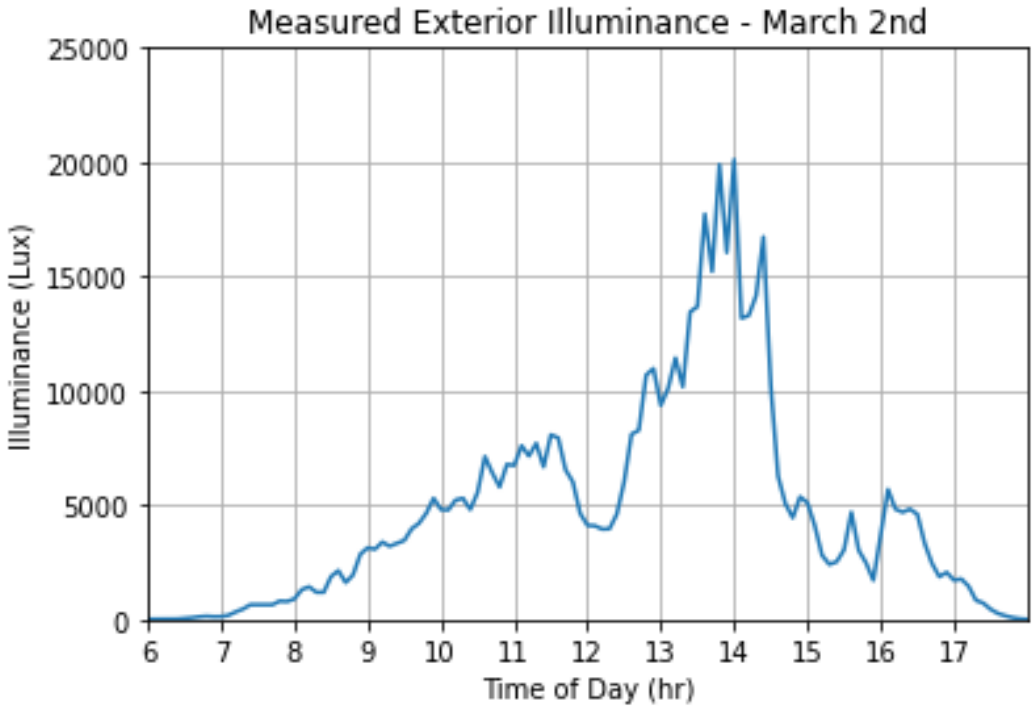

Figure 4.4. Measured Exterior Illuminance – March 2nd, 2023.

The model accurately predicted the workplane illuminance with an RMSE of 34.82 Lux and a CVRMSE of 7.0%, using the 3-surface radiosity method. The point on the workplane where the sensor was positioned was 1.55 meters from the window. A static blind tilt angle of 90° was maintained throughout the day, as the venetian blinds were still manually operated at the time of the experiment, leading to the limitation for model verification at only a horizontal blind tilt angle. For the March 2nd test the installed roller shade was left fully open to allow the zone to harvest the minimal solar gains and daylight available. See figure (4.5) for the daylighting model verification.

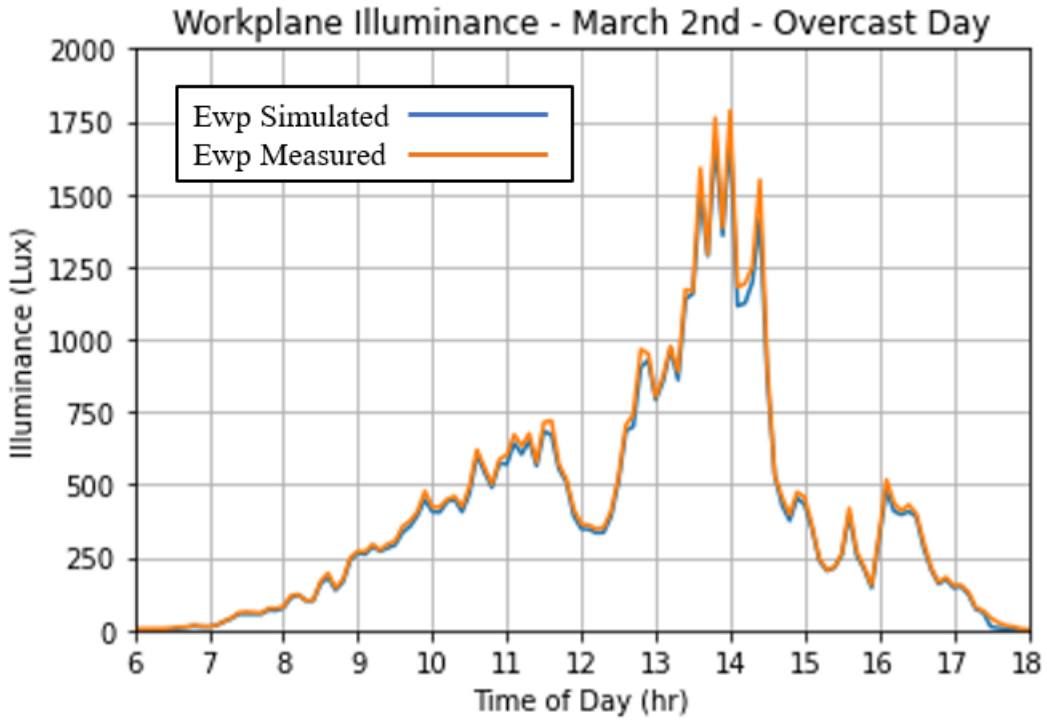

Figure 4.5. Workplane Illuminance – March 2nd, 2023. Measured vs. Simulated Results

4.2. Energy Performance

4.2.1. Hydronic Radiant Floor Heating System

This experiment was conducted on February 28th – March 2nd and the following results are being reported for March 2nd, which was a mild and overcast day, providing reduced solar gains for passive heating (see figure 4.1). A nighttime setback was employed on this day and is considered the reference case for flexibility calculations (see T_{sp} in figure 4.2) and considers internal gains from a person, a laptop, and artificial lights. The heating load in the morning peak period, 6-9 AM, was shown to be 1.63 kWh, while the evening period, 4-8 PM, had a load of 1.17 kWh. Daily heating loads and the BEFI(P) are shown in figure (4.6), when simulating different preheating durations (1-6 hours) before the morning and evening peak demand periods. These preheating strategies were employed and simulated for the cases of buildings with limited control of setpoints.

The thermostats installed at the FBL had four available setpoint changes in a day, therefore, simple preconditioning strategies were simulated. Near optimal (NO) strategies developed by Jalilov & Athienitis (2021) were also simulated for buildings with advanced control capabilities. The near optimal case in the table was developed for a mild and cloudy day.

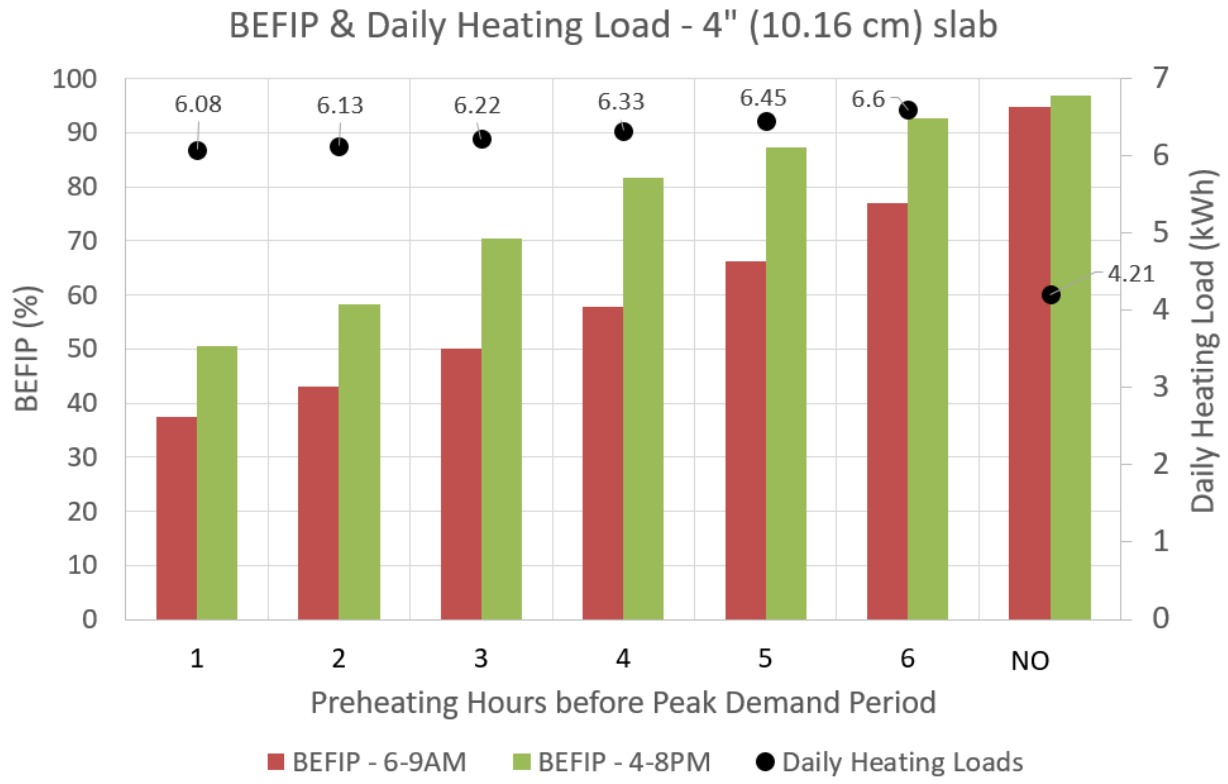

Figure 4.6. BEFI(P) and Qh results for March 2nd experiment in both peak demand periods for 10.16 cm (4") slab.

All flexibility cases reduced the daily heating load ($Q_{h,ref} = 6.97$ kWh), where the maximum reduction was due to the near optimal case from Jalilov & Athienitis (2021). The maximum energy shifted in the morning peak period was 76.9% from a 6-hour preheating period from 12-6AM and 94.8% from the near optimal case. The energy in the evening peak period could be shifted greater than 80% after 4 hours of preheating before 4PM or 96.8% using the near optimal temperature setpoint strategy. The evening period required lower preheating durations to shift the heating loads due to the transmitted solar gains, although reduced on an overcast day.

Other factors that resulted in longer durations for shift the heating loads from the peak morning period include the low supply temperature from the water heater and the concrete properties of the hydronic system. The supply temperature of the water heater was kept at the lowest setting of 43 °C and resulted in low auxiliary heating applied to the bottom of the slab. The concrete installed was lightweight concrete having a density of 1995 kg/m^3, which resulted in a low thermal conductivity of 0.872 $W/m \cdot K$ and specific heat capacity of 913 $J/kg \cdot K$. The equations used for these properties can be found in Appendix D. With lightweight concrete, the thermal lag is increased, therefore, after a certain slab thickness, the load shifting capabilities from simple preconditioning is significantly reduced shown in figure (4.7). Simulations show that for a slab thickness above 4" the BEFIP will drop well below 75% for a 6 hour preheat duration. The maximum BEFIP occurs for the 3" slab with increasing preheating durations in the morning. The near optimal temperature setpoint strategy for a mild and cloudy day provided load shifting above 90% for all simulation cases of 3" through 7" slab thicknesses as lower preheating was induced before the peak demand periods, compared to the standard 1-6 preheat durations. The smallest slab thickness simulated was 3" as a 2" slab was considered to have insufficient depth with the floor insulation installed.

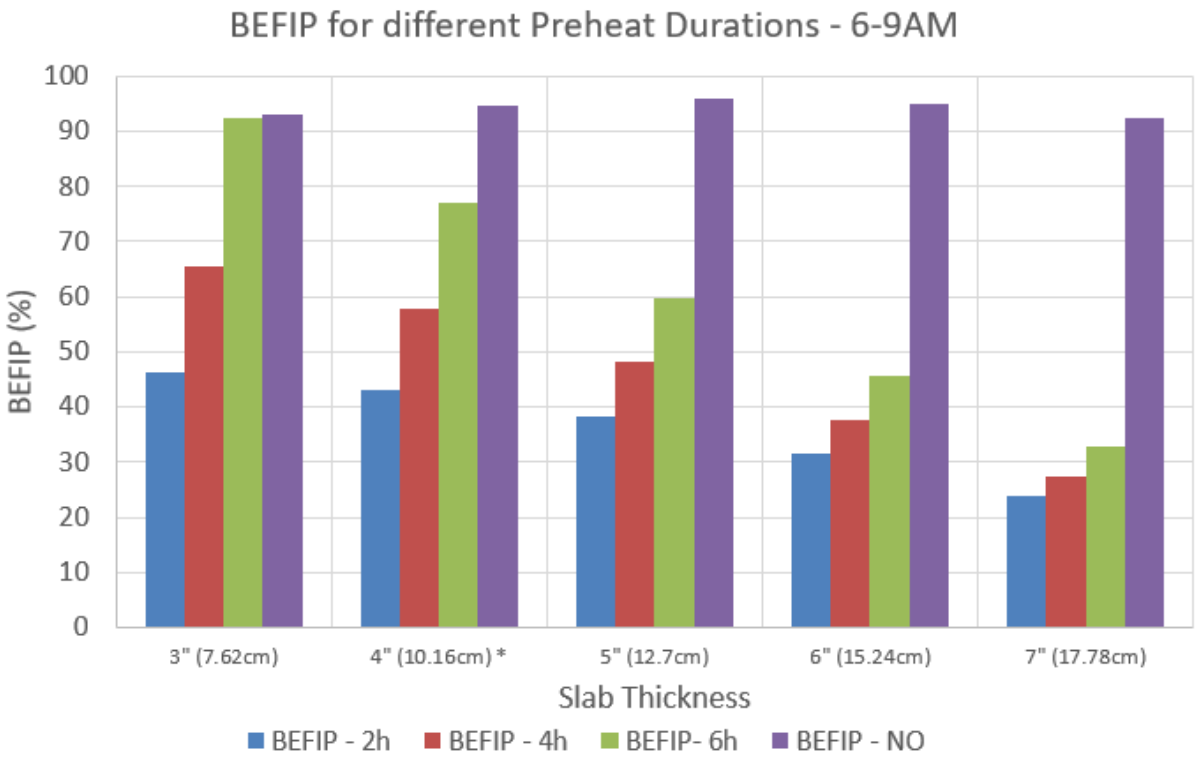

Figure 4.7. BEFIP (%) for different slab thicknesses and preheat durations.

4.2.2. Semi-Transparent PV Window Production

The PV windows were not ready for testing, as the windows were not hooked up to the inverters, therefore, this section estimates the generated electricity from the bifacial STPV window. The PV production from the STPV window was simulated for both clear and cloudy days. Using King's and Evans' models, we can estimate the PV production for an STPV window using equations (3.14) through (3.20). Furthermore, the estimated PV production from the incremental bifacial PV cells is compared to the monofacial generation for both types of day. One section is triple glazed and one section is quadruple glazed. The electric power generation for the bifacial PV window is given by Pel_bf, the generation of the front and back side of the PV cells are given as Pel_f and Pel_b, respectively.

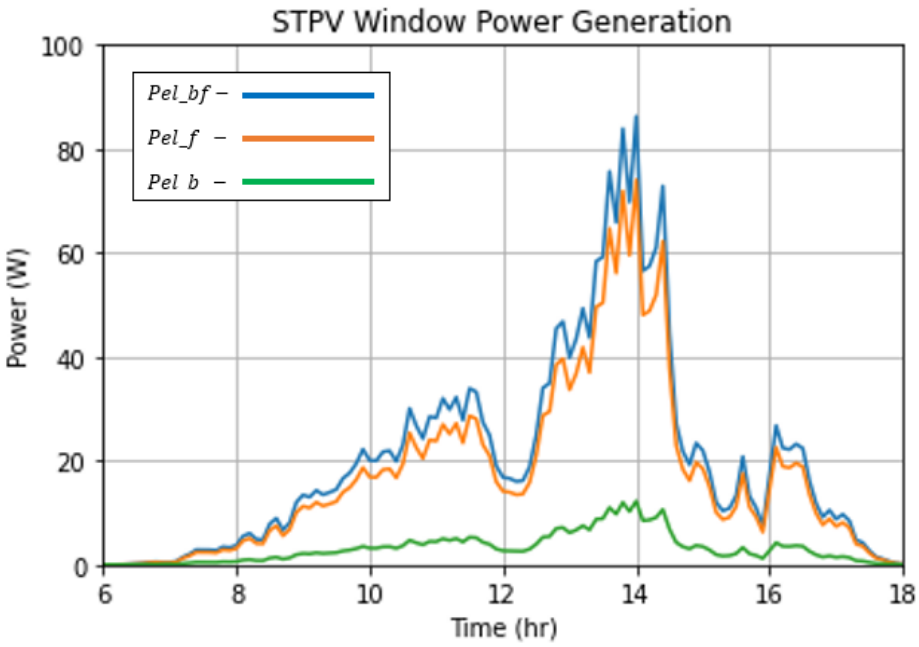

Figure 4.8. Power Production from STPV Window on Cloudy Day – March 2nd, 2023.

Figure (4.8) shows the power production for a cloudy day, low daily power generation was expected, and the calculated daily energy generation was 0.243 kWh (0.137 kWh/m^2). The effect of the bifacial cells increased the daily energy production by 16.6%. The percentage increase from the bifacial cells was calculated to be 14.0% for a clear day (see figure C.4 in Appendix C), which is a lower increase compared to a cloudy day. During the heating season there is low available solar radiation and sunlight during the morning peak (6-9AM) and evening peak (4-8PM) demand periods. This means the energy flexibility may improve only slightly for the heating demand. On the cloudy day simulation for March 2nd an average power of 9.14 Wh was generated in the morning peak period, while 21.98 Wh was generated in evening peak period. A clear day was simulated on March 2nd and the PV window could generate 130.26 Wh and 48.45 Wh in the morning and evening peak demand periods, respectively.

Packing Factor

The design variable of these active solar windows is the packing factor, and we can simulate the expected electricity production, increase of production from monofacial to bifacial, and transmitted solar gains from different packing factors. Simulations were based on the allowable size of the PV cells at the FBL, which had dimensions of width and height of 15.68 cm x 15.68 cm. These PV cells were in a row of 6 to span the total width of the window section. Figure (4.9) shows the electrical energy produced and increased production when switching from monofacial to bifacial PV cells. The thermal energy transmitted, or solar gains, must be considered when designing the PF, and through simulations, the transmitted thermal energy will decrease linearly with an increasing packing factor. Furthermore, the opaque PV cells simultaneously act as a shading system for daylight. By increasing the packing factor, the available area for transmissible daylight will decrease. Therefore, the daylighting availability in the zone decreases along with the potential for glare.

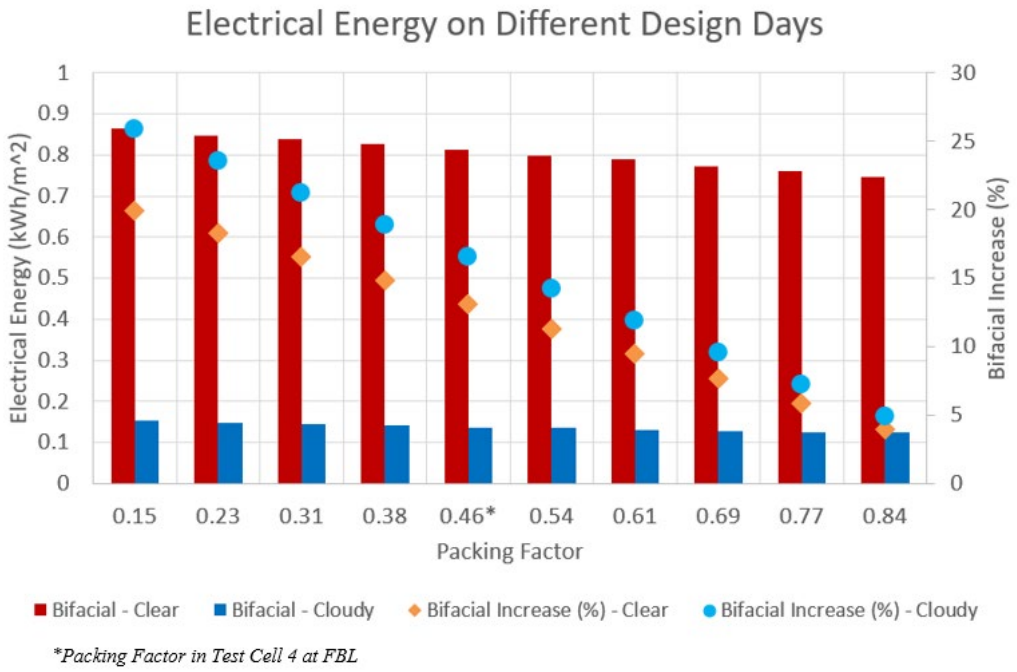

Figure 4.9. Electrical Energy (kWh) of Bifacial STPV Window and Increase of Bifacial Output Compared to Monofacial on Clear and Cloudy Days.

4.2.3. Lighting Energy

Table (4.4) shows the simulation results of the lighting energy needed to maintain a sufficient illuminance level at the workplane height, 0.8m, for a point 1.55 meters from the window in the center of the room. Two luminaires are installed in test cell 4 are 45.33-W LED lamps with 6120 initial lumens per lamp. These luminaires are operated with a motion sensor and can be on or off. The motion sensor was covered during experiments to obtain the daylighting availability only. Different control strategies simulated include a reference case of always on during working hours (8-5PM), on/off which will turn the lights on when the workplane illuminance drops below 500 lux, and two dimming strategies based on the workplane illuminance target of 500 lux. The dimming curves were modeled using the manufacturer specifications (e.g., 50% dimming = $45.33 \cdot 0.5$ W), where 45.33 W is the power output of one lamp when turned on. Simulations were completed for clear and cloudy days with four different blind control strategies. During the clear day simulation, the roller shade was considered closed as when it was open there was very high risks for glare. The UDI results are shown in table (4.6) in the occupant comfort section.

Table 4.4. Daily Lighting Loads from Blind Tilt Angle and Artificial Lighting Dimming Strategies.

Blind Control		**Horizontal**	**Always Open**	**Cut-Off**	**Hybrid PD Open**
Lighting Control		Cloudy			
Reference: Always on Occupancy	Q_l (kWh)	0.83			
On/Off		0.51	0.44	0.54	0.54
5 Dimming Levels		0.29	0.22	0.33	0.30
7 Dimming Levels		0.24	0.19	0.27	0.25
Lighting Control		Clear (Roller Shade Closed for Glare)			
Reference: Always on Occupancy	Q_l (kWh)	0.83			
On/Off		0.08	0.05	0.22	0.10
5 Dimming Levels		0.05	0.02	0.12	0.05
7 Dimming Levels		0.04	0.02	0.10	0.03

On a cloudy day, the energy required to power the lamps for working hours is 0.83 kWh. By combining the daylight transmitted through the window and controlled lighting loads, the lighting demand is reduced. The always open blind strategy should be used during overcast days to transmit the limited illuminance incident on the window and the roller shade should be kept fully open. On clear days the always open strategy will produce the lowest daily lighting load but the risk for glare increases, therefore, the hybrid strategy should be used to minimize the risk of glare and reduce the lighting energy simultaneously. Furthermore, by implementing dimming control strategies of the artificial lights, the lighting load during the peak demand periods can be reduced. On clear days, the lighting can be shifted 100%, considering the beginning of the workday is at 8AM, while on cloudy days, the reduction is lower at 31.8% in the morning peak period. Similarly, in the evening peak demand period, the lighting load can shift 79.3% on clear days while maintaining visual comfort and 53.9% on cloudy days, based on the March 2nd experiment.

4.2.4. Combined BEFI(P)

The table below shows the BEFI(P) results for the combination of the hydronic radiant floor, lighting loads based on the blind tilt angle, and semi-transparent PV window. The STPV section shows the shifted power (W) and the increase of energy generation when switching from monofacial to bifacial PV cells (%).The optimal T_{sp} for each case was the setpoint strategies from Jalilov and Athienitis (2021), the highest reduction in energy from the artificial lights was due to a 7-dimming level strategy, and the optimal blind control strategy for clear days was a hybrid strategy while the always open strategy provided optimal results on cloudy days. The heating and lighting loads were able to be shifted 100% on clear days, therefore, the STPV generation was shown as >100% in table (4.5). In real situations this available power may be used for plug loads, appliances, etc.

Table 4.5. Combined BEFI 6-9AM for different design days in the heating season – near optimal cases.

Design Day	BEFI-HRFH		BEFI-LL		BEFI-STPV*		BEFI-TOT	
	(W)	(%)	(W)	(%)	(W)	(%)**	(W)	(%)
Clear-Mild (Hyb)	550.0	100.0	30.2	100.0	43.4	14.0	**580.2**	**>100.0**
Cloudy-Mild (AO)	515.7	94.8	9.6	31.8	3.1	16.6	**525.6**	**94.9**
Clear-Very Cold (Hyb)	550.0	100.0	30.2	100.0	50.0	14.6	**580.2**	**>100.0**
Cloudy-Very Cold (AO)	109.3	19.9	9.6	31.8	3.2	16.8	**118.8**	**20.5**

** STPV window energy generation.*
*** Average increase % of monofacial to bifacial PV cells.*

Table (4.5) describes the cases optimal combinations of control strategies based on the design day based on energy performance and occupant comfort. For all types of days, the temperature setpoint strategies developed by Jalilov & Athienitis (2021) had the maximum shifting capabilities for the heating loads. On clear days, the hybrid blind control strategy should be employed to simultaneously improve energy performance and maintain comfort. Additionally, for buildings having high WWRs and based on these results, roller shades should be closed to reduce potential discomfort. On cloudy days, the always open blind strategy should be used to harvest the minimal solar gains and daylight available.

For the 'very cold and cloudy' simulation the shifting ability of the slab was much lower compared to clear or milder days, as significant heat losses were seen through the large windows. In this study, the supply temperature from the water heater was kept at the minimum setting of 43 °C and further cooled by mixing with the return water from the hydronic loop. The supply temperature of the tank should be increased to provide more heating to the base of the slab. Similarly, the flow rate of the system may be increased to improve the heating provided by the hot water.

4.3. Occupant Comfort

4.3.1. Thermal Comfort

This section shows the results of thermal comfort, in terms of operative temperature versus relative humidity. The boundaries of operative temperatures at different relative humidities are plotted with calculated operative temperature points, based on measured air temperature, plane radiant temperature, and relative humidity. The percentage of time within the 'comfort zone' will be calculated for clear and cloudy conditions. Figure (4.11) shows the data points of the operative temperature and relative humidity throughout the workday based on the March 2nd test with a nighttime setback control strategy employed on a mild winter day. This figure shows the results of the operative temperature calculated from both measured and simulated temperatures. Internal gains were omitted for a person and lighting for the calculation to compare to the measured results. The bounds of the recommended PMV range of ±0.5 from ASHRAE (2010a) are the blue curves and the expanded PMV range of ±1 is the orange curves. For this comfort analysis, the relative humidity measurements during the test were used in all simulations, as RH was not programmed into the finite difference equations.

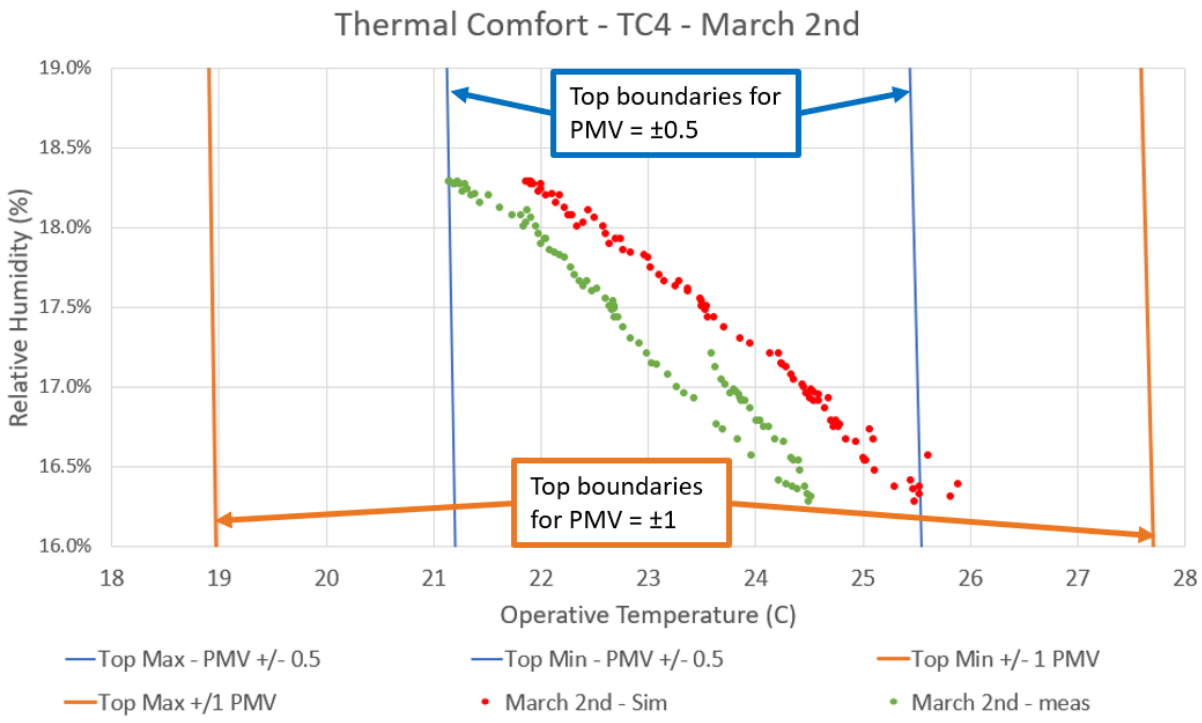

Figure 4.11. Operative Temperature vs. Relative Humidity results for March 2nd, 2023, for different simulations. March 2nd.

Based on the timestep of 6 mins (0.1 hours) for simulations and measurements, 94.4% of the day was within a ±0.5 range and 100% of the day was within a ±1 PMV range. Therefore, 5.6% of the workday was 'slightly warm' ($+0.5 < PMV < +1$). The measured values maintained a PMV range of ±0.5 throughout the entire workday. The error between the simulated and measured operative temperature values result from the average wall surface temperature having the larger prediction error.

Thermal Comfort for different Design Days

Figure (4.12) shows the results of occupant comfort and daily heating loads for the 'optimal' case for each design day. For the analysis below, internal gains from an occupant, laptop, and lighting were added to the RC thermal network to simulate an actual office space. A person doing light work in an office produces 64-70 W (ASHRAE, 2017), the LED lights were assumed to produce 17.2 W (Kim et al., 2018), and laptop was assumed to produce 20 W of heat (Menezes et al., 2014).

With low interior air speeds, it is assumed that 60% of the internal gains will be radiant heat (ASHRAE, 2017). Figure (4.12) shows the heating loads and thermal comfort percentages for simulations with an assumed occupant during the hours of 8AM-5PM. This table shows the cases of the reference test and the combined control strategies which provided the optimal energy performance and occupant comfort. The results in this table include internal gains for when an occupant is present. The abbreviations of NSB and NO represent the nighttime setback and near optimal temperature setpoints, respectively. Similarly, AO and Hyb PD represent the always open and hybrid peak demand period control strategies.

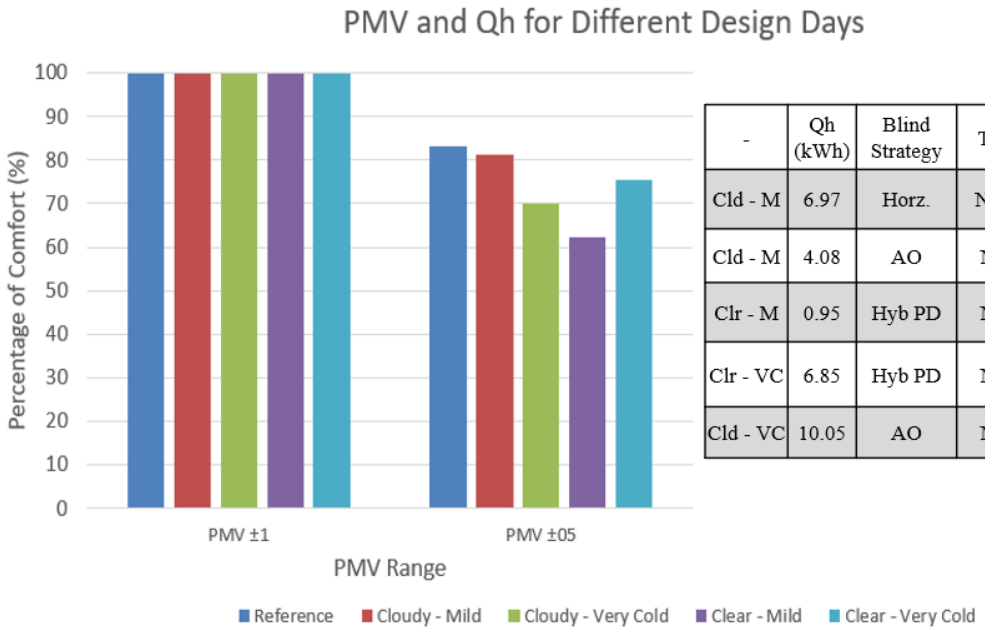

-	Qh (kWh)	Blind Strategy	Tsp.	PMV ±1 (%)	PMV ±0.5 (%)
Cld - M	6.97	Horz.	NSB	100	83.3
Cld - M	4.08	AO	NO	100	81.1
Clr - M	0.95	Hyb PD	NO	100	62.2
Clr - VC	6.85	Hyb PD	NO	100	75.6
Cld - VC	10.05	AO	NO	100	70

Figure 4.12. Thermal Comfort and Daily Heating Loads for Different Design Days.

The always open strategy reduced the daily heating loads even further compared to the hybrid strategy, but there was an overheating issue due to excessive solar gains. The hybrid strategy angles itself as the always open strategy during the peak demand periods, therefore, helps improve energy flexibility of the building. Furthermore, the incident solar gains on the TAB system allows for increased passive heating with the stored thermal energy.

4.3.2. Visual Comfort

The experiment to assess the glare in the zone using the DGI_n method had to be completed separately and is described in Appendix C. The glare potential (GP) based on the workplane illuminance above 2500 Lux was calculated and is shown in table (4.7). The UDI for different blind control strategies is described; horizontal, always open (AO), cut off (CO), and hybrid, meaning always open during the peak demand periods and cut off during the remainder of the day. Simulation results for the roller shade fully open and fully closed is shown for the clear day. With the open roller shade in high WWRs there is a high potential for glare, even with a cut off blind strategy employed.

Table 4.6. UDI and Glare Potential based on 38.7% WWR and different blind control strategies for different exterior conditions.

WWR = 38.66%	**Horizontal**	**Always Open**	**Cut Off**	**Hybrid**
	Clear (Roller Shade Closed for Glare)			
$UDI_{500-2500}$ (%)	90.1	71.4	73.6	87.9
$GP_{>2500}$ (%)	0	23.1	0	0
	Clear (Roller Shade Open)			
$UDI_{500-2500}$ (%)	18.7	15.4	22.0	19.8
$GP_{>2500}$ (%)	78.0	82.4	73.6	78.0
	Cloudy (Roller Shade Open)			
$UDI_{500-2500}$ (%)	38.5	46.2	34.1	34.1
$GP_{>2500}$ (%)	0.0	0.0	0.0	0

The WWR present in test cell 4 is near the maximum allowable WWR from ASHRAE, (2017) of 40%. Reducing the WWR will ultimately reduce the potential for glare but increase the lighting energy required to maintain a sufficient workplane illuminance of between 500-2500 Lux.

4.4. Conclusions

This chapter discusses the proposed model and its verification from experimental work completed from February 28th to March 2nd. The key conclusions found in these results are explained below:

- Each modelling approach of the hydronic floor had very similar errors of room air, floor surface, and wall surface temperature. Therefore, simulations were completed with the 2nd order model for reduced complexity.
- All simulated preheating durations, from 1 to 6 hours, before each peak demand period will reduce the daily heating load of the perimeter zone, in addition to the energy flexibility benefits. For optimal energy performance benefits, near optimal strategies from Jalilov & Athienitis (2021) should be used in buildings with advanced control capabilities.
- To obtain a significant shifted heating load in the morning peak demand period, higher preheating times are required compared to the evening peak demand period, due to the lack of solar gains. 6 hours of preheating could shift 76.9% of the heating load in the morning whereas 4 hours of preheating could shift 80% of the energy in the evening peak period on a cloudy day.
- Significant reductions in BEFI(P) results are seen with slab thicknesses above 4" (10.16cm) due to excess thermal storage, especially for a lightweight concrete mixture which has a higher thermal lag compared to normal weight concrete. From this study the desired range of 3" (7.62 cm) to 4" (10.16 cm) was found for the slab thickness of LWC and its ability to shift heating loads based on simple preheating strategies. The 5" slab simulation only shifted 60% of the heating load after 6 hours of preheating.
- During the heating season, the STPV window's effect on energy flexibility is minimal due to later sunrise and earlier sunset times.
- The daylighting model showed higher errors when compared to the heating results. This study used a 3-surface radiosity model for workplane illuminance calculations, where a 7-

surface model, hybrid ray tracing, or ray tracing model would be expected to reduce the errors discussed.

- The need for artificial lighting is reduced with high glazing areas typically seen in office perimeter zones. Cloudy days can provide sufficient workplane illuminance (>500 Lux) without the need for artificial lighting. See figure (4.5) and table (4.6).

- Thermal comfort was achieved to 100% of a PMV range of ±1 on the experiment conducted on March 2nd and validated with the model. When applying different flexibility strategies, the perimeter zone maintained thermal comfort for all cases.

Chapter 5: Conclusions & Future Directions

This thesis developed a methodology for the design and predictive control of active solar windows and radiant floor heating for perimeter zones in commercial buildings. The model was validated through experiments throughout the heating season at an outdoor test facility in Montreal, Quebec, the Future Building's Lab (FBL). The three systems investigated in this thesis include bifacial semi-transparent photovoltaic windows, motorized venetian blinds, and a hydronic radiant floor.

The resistance-capacitance (RC) model created is of 3rd order with two capacitances in the hydronic floor and the 3rd capacitance modelled into the lumped wall surfaces. A sensitivity analysis of the concrete floor capacitances was completed with 2-4 concrete capacitances and all three models had very similar error. Therefore, to minimize complexity, a 2nd order hydronic floor and 3rd order zone model was used for simulations. The daylighting model used in this thesis was a 3-surface radiosity model and provided acceptable predictions of the workplane illuminance. Key design variables and near-optimal control strategies of the systems were investigated and simulated for all systems in the perimeter zone, shown in table (5.1):

Table 5.1. Integrated systems: design and control variables.

System	Design Variable	Control Variable
Bifacial STPV Window	Packing Factor (PF); Window-to-wall ratio (WWR)	-
Motorized Venetian Blinds	-	Blind Tilt Angle (β)
Hydronic Radiant Floor	Slab Thickness (L_{slab})	Temperature Setpoint (Tsp)
Artificial Lighting	-	Dimming (%)

These systems were designed and controlled to optimize the combination of energy performance and occupant comfort. The energy performance indicators include energy flexibility and efficiency while the occupant comfort indicators include thermal and visual comfort. Simulations were completed for different environmental conditions of clearness (e.g., clear and overcast) and exterior temperature (e.g., mild and very cold). In all cases the near optimal temperature setpoint strategies developed by Jalilov and Athienitis (2021) provided minimum daily and peak heating loads, while maintaining thermal comfort within the desired PMV range.

Based on the March 2nd experiment, which had a nighttime setback strategy employed, the daily heating load was reduced by 39.6% when implementing near-optimal control strategies for a cloudy and mild day. Similarly, the peak heating loads were reduced by 94.8% and 96.8% in the morning and evening critical periods. The daily lighting load could be reduced by 77% when using near-optimal control of the shading system and artificial luminaires. The peak lighting loads can reduce by 31.8% and 53.9% in the morning and evening peak periods, respectively. Furthermore, the addition of renewable energy systems can further improve the reduction in daily and peak loads, although minimal on cloudy days in the heating season.

Using simple control strategies for energy flexibility, such as preheating before the peak demand periods, hydronic slabs above 4” had reduced shifting abilities due to excessive thermal mass causing higher thermal lags. The 5” slab reduced the morning peak load by 60% with a 6 hour

preheat duration. Simulating increasing slab thicknesses, the BEFIP maintained greater than 90% when using near optimal control strategies from Jalilov & Athienitis (2021), as these strategies relied less on preconditioning. Considering the hydronic system installed at the FBL had limited control capabilities, basic flexibility strategies were investigated for buildings that may lack advanced controllers.

The STPV window installed at the FBL is a bifacial opaque-spaced PV window with a packing factor of 46%. Based on simulations throughout the heating season, the bifacial PV cells can improve the energy generated by 16.6-17% on cloudy days and 13-14.5% on clear days when compared to monofacial PV cells for a PF of 46%.

5.1. Limitations & Future Directions

Limitations

- The thermocouples were mounted with steel poles to provide further stability when the concrete was poured. The heavy concrete and workers walking through the wet concrete may have bumped the sensors off their intended measuring points, causing possible sources of error.
- Initial installation of the window wall had the venetian blinds with manual-based control and the task was to automate these blinds. Due to time constraints, blind tilt angles were manually changed periodically throughout the day, to resemble automation.
- The thermostats used installed with the radiant floor allow programmable schedules for each day of the week, which can help improve your energy efficiency and shift the heating demands away from the peak demand periods. This thermostat has a constraint that restricts setpoint changes to a maximum of 4 per day, instead of allowing changes on an hourly

basis. These setpoint changes correspond to a typical homeowner's daily routine: waking up, heading to work, coming back from work, and going to sleep.

- Visual comfort experiments for workplane illuminance and glare had to be conducted separately as three illuminance sensors were available.
- Energy generation from STPV window was simulated based on results of standard testing conditions. The PV windows were not hooked up to the inverters at the time of the experiments.

Future Directions

There is considerable future research that can be completed with this system set-up. The current research focuses on improving energy performance in the heating season, as space heating currently accounts for the greatest share of energy demands in commercial buildings in Quebec. The fastest growing energy end-use is space cooling (IEA 2018), appliances, and plug loads (GlobalABC et al., 2019), therefore, future projects related to this study should consider both shoulder and cooling seasons. Additionally, perimeter zones may have high cooling demands in the heating season at high latitudes in buildings with high window to wall ratios. Improvements of this model may include the Rheem heat pump/water heater installed in the FBL which can provide cooling to the zones. During clear days the operative temperatures were often nearing the upper limit of the PMV boundary of +1 and would have exceeded the allowable boundary without proper shading from the venetian blinds and the roller shade. Occupants have a restricted view to the outdoors in these cases.

The conflicting needs for more daylight and the need to reduce excess solar gains and avoid glare is an important topic that is studied in this thesis but needs further research, including other design and control options such as electrochromic glazing. By applying a voltage to this system, the

optical properties will change, and this system can be considered a battery (Sibilio et al., 2016). Electrochromics have shown to reduce up to 60% of artificial lighting loads, reduce cooling loads up to 20%, and the peak power up to 26%. Furthermore, these systems may reduce visual discomfort due to windows (Casini, 2018). This technology has the potential to satisfy the key performance indicators outlined in this thesis of energy flexibility, energy efficiency, thermal comfort, and visual comfort.

Optimizing the electricity generation for STPV windows is another topic that needs further study, such as the control of the blind tilt angle for optimal electricity production. Optical properties of venetian blinds have been modelled based on different blind tilt angles which may be optimized for electricity production (Tzempelikos, 2008). In the current model, blind tilt angle strategies were implemented for the trade off between transmission and shading to improve energy performance and maintain occupant comfort.

In terms of interior environmental quality (IEQ), a focus on the literature for thermal and visual quality is described in this study. Air quality is another vital factor which contributes to an acceptable interior environment and should be a topic of integration for future work. With the recent emergence of the COVID-19 pandemic and the expected increase in frequency of extreme epidemics (Marani et al., 2021), ensuring optimal air quality should be a significant discussion in future research and building projects.

5.2. Contributions

- This study presents a methodology for the design and predictive control of active solar windows and radiant floor heating systems in commercial buildings. This methodology provides a systematic approach to optimize energy performance and occupant comfort in

perimeter zones. Furthermore, the developed model is validated through experiments conducted at the Future Building's Lab (FBL) in Montreal, Quebec. By validating the model in an outdoor test facility, the research ensures its accuracy and reliability in real-world conditions.

- This study investigates three systems: bifacial semi-transparent photovoltaic windows, motorized venetian blinds, and hydronic radiant floors. The analysis and evaluation of these systems contribute to understanding their potential in enhancing energy performance and occupant comfort in perimeter zones of commercial buildings.
- This study performs a sensitivity analysis and determines that a simplified 2nd order hydronic floor model and 3rd order zone model provide comparable results to more complex models. This finding allows for reduced complexity in simulations and practical implementation of the models.
- This study proposes near-optimal temperature setpoint strategies that have been previously developed by Jalilov and Athienitis (2021). These strategies minimize daily and peak heating loads while maintaining thermal comfort within desired ranges. The research highlights the limitations of excessive thermal mass in hydronic slabs and proposes design considerations for buildings with limited control capabilities.

International Peer-Reviewed Conference Papers

- **Hill, J.R.**, Athienitis, A.K. (2023). Methodology for Predictive Control of Zones with STPV Windows, Motorized Shades, and Hydronic Floor Heating for High-Performance Buildings. Proceedings of the 5th International Conference on Building Energy and Environment (COBEE), Montreal, CA, July 25-29, 2022.

- **Hill, J.R.**, Athienitis, A.K., Larochelle-Martin, G. (2023). Methodology for Design and Predictive Control of Zones with STPV Windows and Motorized Venetian Blinds, and Hydronic Floor Heating for Net-Zero Energy Buildings, ASHRAE Winter Conference 2023, Atlanta, US, February 4-8, 2023. Presented on Feb. 8th.

References

ACI. (2002). ACI 122-02 - Guide to Thermal Properties of Concrete and Masonry Systems. Farmington Hills, US: American Concrete Institute.

Akinci, B., Garrett, J. H., & Akin, Ö. (2011). Identification of functional requirements and possible approaches for self-configuring intelligent building systems. Gaithersburg, MD: National Institute of Standards and Technology.

Al-Masrania, S. M., Al-Obaidi, K. M. (2019). Dynamic shading systems: A review of design parameters, platforms and evaluation strategies. *Automation in Construction*, *102*, 195-216.

Al-Masrania, S. M., Al-Obaidi, K. M., Zalina, N. A., & Aida Isma, M. I. (2018). Design optimisation of solar shading systems for tropical office buildings: Challenges and future trends. *Solar Energy*, *170*, 849-872.

Al-Tamimi, N. A., & Fadzil, S. F. S. (2011). The potential of shading devices for temperature reduction in high-rise residential buildings in the tropics. *Procedia Engineering*, *21*(3-4), 273-282.

Altan, H., Hajibandeh, M., Tabet Aoul, K. A., & Deep, A. (2016). Chapter 8: Passive Design, ZEMCH: Toward the delivery of Zero energy mass custom homes, SPRINGER, 2016, 209–236.

ASHRAE. (2010a). ASHRAE Standard 55—Thermal Environmental Conditions for Human Occupancy. Atlanta, US: American Society of Heating Refrigeration and Air Conditioning Engineers, Inc.

ASHRAE. (2010b). ASHRAE Standard 90.1- Energy Standard for Sites and Buildings Except Low-Rise Residential Buildings. Atlanta, US: American Society of Heating Refrigeration and Air Conditioning Engineers, Inc.

ASHRAE. (2010c). ASHRAE Standard 62.1 – Ventilation for Acceptable Indoor Air Quality. Atlanta, US: American Society of Heating Refrigeration and Air Conditioning Engineers, Inc.

ASHRAE. (2016). ASHRAE Standard 90.1 – Performance Rating Method Reference Manual. Atlanta, US: American Society of Heating Refrigeration and Air Conditioning Engineers, Inc.

ASHRAE Handbook. (2017). Fundamentals – SI Edition. Atlanta, US: American Society of Heating Refrigeration and Air Conditioning Engineers, Inc.

ASHRAE Handbook. (2019). Heating, Ventilating, and Air-Conditioning Applications – SI Edition. Atlanta, US: American Society of Heating Refrigeration and Air Conditioning Engineers, Inc.

Athienitis, A. K., & Stylianou, M. (1991). Method and Global Relationship for Estimation of Transmitted Solar Energy Distribution in Passive Solar Rooms. *Energy Sources*, *13*(3), 319-336.

Athienitis, A. K. (1997). Theoretical investigation of thermal performance of passive solar buildings with floor radiant heating. *Solar Energy*, *61*(5), 337-345.

Athienitis, A. K. (1999). Building Thermal Analysis. Electronic Mathcad Book - 2nd Edition - in Civil Eng. Library, Mathsoft Inc. Boston, U.S.A.

Athienitis, A. K., Tzempelikos, A. (2002). A Methodology for Simulation of Daylight Room Illuminance Distribution and Light Dimming for a Room with a Controlled Shading Device. *Solar Energy*, *72*(4), 271-281.

Athienitis, A. K., & W. O'Brien, Eds. (2015). Modelling, design and optimization of net-zero energy buildings. Berlin, Wiley Ernst & Sohn.

Athienitis, A. K., Dumont, E., Morovat, N., Lavigne, K., & Date, J. (2020). Development of a dynamic energy flexibility index for buildings and their interaction with smart grids. Proceedings of ACEEE Summer Study 2020 Conference on Energy Efficiency in Buildings, California, USA, August 17-21, 2020.

Bagheri, A., Feldheim, V., Thomas, D., & Ioakimidis, C. S. (2016). Coupling building thermal network and control system, the first step to smart buildings. Proceedings of IEEE International Smart Cities Conference (ISC2), Trento, IT, September 12-15, 2016.

Bagheri, A., Feldheim, V., & Ioakimidis, C. S. (2018). On the Evolution and Application of the Thermal Network Method for Energy Assessments in Buildings. *Energies*, *11*, 890.

Bahaj, A.S., James, P., & Jentsch, M. F. (2008). Potential of emerging glazing technologies for highly glazed buildings in hot arid climates. *Energy Build., 40*, 720–731.

Bambara, J., Athienitis, A. K., & Eicker, U. (2021). Decarbonizing Local Mobility and Greenhouse Agriculture through Residential Building Energy Upgrades: A Case Study for Quebec. *Energies*, *14*, 6820.

Beji, C., Merabtine, A., Mokraoui, S., Kheiri, A., Kauffmann, J., & Bouaziz, N. (2020). Experimental study on the effects of direct sun radiation on the dynamic thermal behaviour of a floor-heating system. *Solar Energy*, *204*, 1-12.

Bellia, L., Marino, C., Minichiello, F., & Pedace, A. (2014). An overview on solar shading systems for buildings. Proceedings of the 6th International Conference on Sustainability in Energy and Buildings (SEB), Cardiff, UK, June 25-27, 2014.

Belussi, L., Barozzi, B., Bellazzi, A., Danza, L., Devitofrancesco, A., Fanciulli, C., Ghellere, M., Guazzi, G., Meroni, I., Salamone, F., Scamoni, F., & Scrosati, C. (2019). A review of zero energy buildings and energy efficiency solutions. *Journal of Building Engineering*, *25*, e100772.

Brideau, S., Beausoleil-Morrison, I., & Kummert, M. (2015). Collection and Storage of Solar Gains Incident on the Floor in a House During the Heating Season. *Energy Procedia*, *78*, 2274-2279.

Brooks, J., Kumar, S., Goyal, S., Subramany, R., & Barooah, P. (2015). Energy-efficient control of under-actuated HVAC zones in commercial buildings. *Energy and Buildings*, *93*, 160-168.

Candanedo, J., Vallianos, C., Delcroix, B., Date, J., Saberi-Derakhtenjani, A., Morovat, N., John, C., & Athienitis, A. K. (2022). Control-oriented archetypes: A pathway for the systematic

application of advanced controls in buildings. *Journal of Building Performance Simulation*, *15*(4), 433-444.

Casini, M. (2018). Active dynamic windows for buildings: A review. *Renewable Energy*, *119*, 923-934.

CEN. (2011). CEN Standard EN 12464-1 – Light and Lighting - Lighting of Workplaces - Part 1: Indoor Workplaces. Brussels, BE. European Committee for Standardization.

Chaloeytoy, K., Ichinose, M., & Sasaki, R. (2019). Comparing the occupants' comfort between perimeter zone and interior zone in Asian office. Proceedings of Sustainable Built Environment Conference (SBE19), Volume 294, Tokyo, JP, August 6-7, 2019.

Chan, Y., & Tzempelikos, A. (2012). A hybrid ray-tracing and radiosity method for calculating radiation and illuminance distribution in spaces with venetian blinds. *Solar Energy*, *86*, 3109-3124.

Chauvel, P., Collins, J. B., Dogniaux, R., & Longmore, J. (1982). Glare from windows: current views of the problem. *Lighting Research & Technology*, *14*(1), 31-46.

Chen, M., Zhang, W., Xie, L., He, B., Wang, W., Li, J., & Li, Z. (2021). Improvement of the electricity performance of bifacial PV module applied on the building envelope. *Energy and Buildings*, *238*(1), e110849.

del Coz Diaz, J. J., Garcia-Nieto, P. J., Alvarez-Rabanal, F. P., Alonso-Martinez, M., Dominguez-Hernandez, J., & Perez-Bella, J. M. (2014). The use of response surface methodology to

improve the thermal transmittance of lightweight concrete hollow bricks by FEM. *Construction and Building Materials*, *52*, 331-344.

Deng, S., Wang, R. Z., & Dai, Y. J. (2014). How to evaluate performance of net zero energy building – A literature research. *Energy*, *71*, 1-16.

Dermardiros, V., Vallainos, C., Athienitis, A. K., & Bucking, S. (2017). Model-Based Control of a Hydronic Radiant Slab for Peak Load Reduction. Proceedings of 15th International Building Performance Simulation Association Conference (IBPSA), San Francisco, California, US, August 7-9, 2017.

Dincer, I., & Rosen, M. A. (2002). Thermal Energy Storage: System and Applications, New York, NY, 99-212.

Dubois, M. -C., & Flodberg, K. (2013). Daylight utilisation in perimeter office rooms at high latitudes: Investigation by computer simulation. *Lighting Research & Technology*, *45*, 52-75.

Duffie, J. A., Beckman, W. A., & Blair, N. (2020). Solar Engineering of Thermal Processes, Photovoltaics and Wind (5th ed.). John Wiley & Sons, Inc.

Eco Design Advisor. (2020). Passive Solar Design. <https://www.ecodesignadvisor.org.nz/passive-solar-design/.> (April 20, 2023)

El Sherbiny, S. M., Raithby, G. D., & Hollands, K. G. T. (1982). Heat Transfer by Natural Convection Across Vertical and Inclined Air Layers. *Journal of Heat Transfer*, *104*(1), 96.

EPA. (2000). Indoor Air Quality and Student Performance. Washington D.C.: United States Environmental Protection Agency, Indoor Environments Division Office of Radiation and Indoor Air.

Evans, D.L. (1981). Simplified method for predicting photovoltaic array output. *Solar Energy*, *27*, 555-560.

Fanger, P.O. (1988). Fundamentals of Thermal Comfort. *Advances In Solar Energy Technology*. 3056–3061.

Fisk, W. J., & Faulkner, D. (1992). Air Exchange Effectiveness in Office Buildings: Measurement Techniques and Results. Proceedings of International Symposium on Room Air Convection and Ventilation Effectiveness (ISRACVE), Tokyo, JP, July 22-24, 1992.

Foucquier, A., Robert, S., Suard, F., Stéphan, L., Jay, A. (2013). State of the art in building modelling and energy performances prediction: A review. *Renewable and Sustainable Energy Reviews*, *23*, 272-288.

Glaser, H. J. (2008). History of the development and industrial production of low thermal emissivity coatings for high heat insulating glass units. *Applied Optics*, *47*(13), C193-C199.

Global Alliance for Buildings and Construction (GlobalABC), International Energy Agency (IEA), and the United Nations Environment Program (UNEP). (2019). 2019 Global Status Report for Buildings and Construction: Towards a Zero-emission, Efficient, and Resilient Buildings and Construction Sector.

Gomez, E. V., Chicote, M. A., Martinez, F. J. R. & Gonzalez, A. T. (2017). Thermal behaviour of an active slab: experimental study for TABs applications. Proceedings of the 9th International Conference on Applied Energy, Cardiff, UK, August 21-24, 2017.

Goral, C. M., Torrance, K. E., Greenberg, D. P., & Battaile, B. (1984). Modeling the Interaction of Light Between Diffuse Surfaces. *Computer Graphics*, *22*(4), 75-84.

Government of Quebec. (2020). Framework policy on electrification and the fight against climate change. Quebec, QC.

Grynning, S., Time, B., & Matusiak, B. (2014). Solar shading control strategies in cold climates – Heating, cooling demand and daylight availability in office spaces. *Solar Energy*, *107*, 182-194.

Guili, V. -D., Pos, O. -D., & Carli, M. -D. (2012). Indoor Environmental Quality and Pupil Perception in Italian Primary Schools. *Building and Environment*, *56*, 333-345.

Guo, H., Aviv, D., Loyola, M., Teitelbaum, E., Houchois, N., & Meggers, F. (2019). On the understanding of the Mean Radiant Temperature within both the indoor and outdoor environment, a critical review. *Renewable and Sustainable Energy Reviews*,*117*, e109207.

Hachem-Vermette, C. (2020). Solar Buildings and Neighborhoods: Design Considerations for High Energy Performance, Cham, CH: Springer Nature Switzerland AG, 101–132.

Hee, W. J., Alghoul, M. A., Bakhtyar, B., Elayeb, O. K., Shameri, M. A., Alrubaih, M. S., & Sopian, K. (2015). The role of window glazing on daylighting and energy saving in buildings. *Renewable and Sustainable Energy Reviews*, *42*, 323-343.

Hill, J. R., & Athienitis, A. K. (2023). Methodology for Design and Predictive Control of Zones with STPV Windows and Motorized Venetian Blinds, and Hydronic Floor Heating for Net-Zero Energy Buildings. *ASHRAE Transactions* (In Press).

Hopkinson, R. G. (1972). Glare from daylighting in buildings, *Applied Ergonomics*, 3(4):206-215.

Hottel, H. C. (1976). A Simple Model for Estimating the Transmittance of Direct Solar Radiation Through Clear Atmospheres. *Solar Energy*, *129*(18).

Hughes, J. F., Van Dam, A., McGuire, M., Sklar, D. F., Foley, J. D., Feiner, S. K., & Akeley, K. (2013). Computer Graphics: Principles and Practice (3rd ed.), Boston, US: Addison-Wesley.

Hydro Quebec. (2020). Highlights of the 2020 Progress Report for the 2020-2029 Procurement Plan. Montreal, Quebec.

Hydro Quebec. (2019). Overview of Hydro-Quebec's Energy Resources. Montreal, Quebec.

IEA. (2018). The Future of Cooling: Opportunities for energy efficient air conditioning. Paris, FR: International Energy Agency.

IESNA. (2000). The IESNA Lighting Handbook: Reference & Application. New York, NY: Illuminating Engineering Society of North America.

IESNA. (2012). LM-83-12 IES Spatial Daylight Autonomy (sDA) and Annual Sunlight Exposure (ASE). New York, NY: 2012.

Incropera, F., Bergman, T., Lavine, A., & Dewitt, D. (2011). Introduction to Heat Transfer (6th ed.). John Wiley & Sons, Inc.

Ingersoll, J., & Huang, J. (1985). Heating energy use management in residential buildings by temperature control. *Energy and Buildings*, *8*(1), 27-35.

ISO-7730. (2005). Ergonomics of the Thermal Environment – Analytical determination and interpretation of thermal comfort using calculation of the PMV and PPD indices and local thermal comfort criteria. Geneva: International Organization for Standardization.

Jalilov, E., & Athienitis, A. K. (2021). Heuristic model-based predictive control strategies for an institutional net-zero energy building. Proceedings of the 16th Conference on Sustainable Development of Energy, Water, and Environment Systems (SDEWES), Dubrovnik, HR, October 10-15, 2021.

James, P., Jentsch, M., & Bahaj, A. (2009). Quantifying the added value of BIPV as a shading solution in atria. *Solar Energy*, *83*, 220–231.

Joe, J., & Karava, P. (2019). A model predictive control strategy to optimize the performance of radiant floor heating or cooling systems in office buildings. *Applied Energy*, *245*, 65-77.

Johnsen, K., & Winther, F. V. (2015). Dynamic facades, the smart way of meeting the energy requirements. *Energy Procedia*, *78*, 1568-1573.

Kapsis, K., & Athienitis, A. K. (2015). A study of the potential benefits of semi-transparent photovoltaics in commercial buildings. *Solar Energy*, *115*, 120-132.

Katipamula, S., & Brambley, M. R. (2005). Methods for Fault Detection, Diagnostics, and Prognostics for Building Systems – A Review, Part I. *HVAC&R Research*, *11*(1), 3-25.

Kensek, K., & Hansanuwat, R. (2011). Environment control systems for sustainable design: a methodology for testing, simulating, and comparing kinetic facade systems. *Journal of Creative Sustainable Architecture & Built Environment*, *1*, 27-46.

Khorasanizadeh, H., Sheikhzadeh, G. A., Azemati, A. A., & Shirkivand Hadavand, B. (2014). Numerical study of air flow and heat transfer in a two-dimensional enclosure with floor heating. *Energy and Buildings*, *78*, 98-104.

Kim, J. H., Parl, Y. J., Yeo, M. S., & Kim, K. W. (2009). An experimental study on the environmental performance of the automated blind in summer. *Building and Environment*, *44*(7), 1517-1527.

Kim, H., Parl, K. -s., Kim, H. -y., & Song, Y. -s. (2018). Study on variation of internal heat gain in office buildings by chronology. *Energies*, *11*(4), 1013.

King, D. L., Boyson, W. E., & Kratochvil, J. A. (2004). Photovoltaic array performance model. Report SAND2004-3535. Sandia National Laboratories, Albuquerque, NM, and Livermore, CA.

Kolokotsa, D., Rovas, D., Kosmatopoulos, E., & Kalaitzakis, K. (2011). A roadmap towards intelligent net zero- and positive-energy buildings. *Solar Energy*, *85*, 3067-3084.

Konstantoglou, M., & Tsangrassoulis, A. (2016). Dynamic Operation of Daylighting and Shading Systems: A Literature Review. *Renewable Energy and Sustainable Energy Reviews*, *60*, 268-283.

LANL. (2002). LANL Sustainable Design Guide. Santa Fe, NM: Los Alamos National Laboratory.

LBNL. (2019). Lawrence Berkeley National Laboratory. WINDOW 7.7. <https://windows.lbl.gov/software/window> (January 23, 2023)

Lee, S., & Lee, K. S. (2019). A study on the Improvement of the Evaluation Scale of Discomfort Glare in Educational Facilities. *Energies*, *12*(17), 3265.

Lim, T., Yim, W. -S., & Kim, D. -D. (2022). Analysis of the Thermal and Cooling Energy Performance of the Perimeter Zones in an Office Building. *Buildings, 12*(2), 141.

Liu, B. Y. H., & Jordan, R. C. (1960). The Interrelationship and Characteristic Distribution of Direct, Diffuse and Total Solar Radiation. *Solar Energy*, *4*(3), 1-19.

Lorenzo, E. (2021). On the historical origins of bifacial PV modelling. *Solar Energy*, *218*, 587-595.

Luo, Y., Zhang, L., Bozlar, M., Liu, Z., Guo, H., & Meggers, F. (2019). Active building envelope systems toward renewable and sustainable energy. *Renewable and Sustainable Energy Reviews*, *104*, 470-491.

Ma, P., & Wang, L. -S. (2012). Effective heat capacity of interior planar thermal mass (iPTM) subject to periodic heating and cooling. *Energy and Buildings*, *47*, 44-52.

Magrini, A., Lentini, G., Cuman, S., Bodrato, A., & Marenco, L. (2020). From nearly zero energy buildings (NZEB) to positive energy buildings (PEB): The next challenge - The most recent European trends with some notes on the energy analysis of a forerunner PEB example. *Developments in the Built Environment*, *3*, e100019.

Manning, M., Swinton, M. C., Szadkowski, F., Gusdorf, J., & Ruest, K. (2007). The effects of thermostat setback and setup on seasonal energy consumption, surface temperatures, and recovery times at the CCHT twin house research facility. *ASHRAE Transactions*, *113*(1), 630-641.

Manz, H. (2008). On minimizing heat transport in architectural glazing. *Renewable Energy*, *33*(1), 119-128.

Marani, M., Katul, G. G., Pan, W. K., & Parolari, A. J. (2021). Intensity and Frequency of Extreme Novel Epidemics. Proceedings of the National Academy of Sciences, *118*(35), 1-4.

Mařík, K., Rojíček, J., Stluka, P., & Vass, J. (2011). Advanced HVAC Control: Theory vs. Reality. IFAC Proceedings Volumes, *44*(1), 3108–3113.

McDowall, R. (2007). Fundamentals of HVAC Systems – SI Edition. Atlanta, GA: American Society of Heating, Refrigeration and Air-Conditioning.

Menezes, A. C., Cripps, A., Buswell, R. A., Wright, J., & Bouchlaghem, D. (2014). Estimating the energy consumption and power demand of small power equipment in office buildings. *Energy and Buildings*, *75*, 199-209.

Michael, P. R., Johnston, D. E., & Moreno, W. (2020). A conversion guide: Solar Irradiance and Lux Illuminance. *Journal of Measurements in Engineering*, *8*(4), 153-166.

Moe, K. (2010). Thermally Active Surfaces in Architecture. Princeton Architectural Press.

Montgomery, D. (2013). Design and Analysis of Experiments (8th Ed.). John Wiley & Sons.

Navarro, L., Gracia, A, -d., Colclough, S., Browne, M., McCormack, S. J., Griffiths, P., & Cabeza, L. F. (2016). Thermal energy storage in building integrated thermal systems: A review. Part 1. Active storage systems. *Renewable Energy*, *88*, 526-547.

Nazzal, A. A. (2005). A new evaluation method for daylight discomfort glare. *International Journal of Industrial Ergonomics*, *35*(4), 295-306.

NFRC. (2010). Technical Interpretations Manual. Greenbelt, MD: National Fenestration Rating Council.

Ning, B., Schiavon, S., & Bauman, F. S. (2017). A novel classification scheme for design and control of radiant system based on thermal response time. *Energy and Buildings*, *137*, 38-45.

Nourozi, B., Ploskic, A., Chen, Y., Chui, J. N-W., & Wang, Q. (2020). Heat transfer model for energy-active windows - An evaluation of efficient reuse of waste heat in buildings. *Renewable Energy*, *162*, 2318-2329.

Péan, T. Q., Salom, J., & Costa-Castelló, R. (2019). Review of control strategies for improving the energy flexibility provided by heat pump systems in buildings. *Journal of Process Control*, *74*, 35–49.

Pless, S., & Torcellini, P. (2010). Net-Zero Energy Buildings: A Classification System Based on Renewable Energy Supply Options. Technical Report NREL/TP-550-44586. Golden, CO: National Renewable Energy Laboratory.

Poirazis, H., Blomsterberg, Å., & Wall, M. (2008). Energy simulations for glazed office buildings in Sweden. *Energy and Buildings*, *40*(7), 1161-1170.

Prívara, S., Cigler, J., Váňa, Z., Oldewurtel, F., Sagerschnig, C., & ŽáčEková, E. (2013). Building modeling as a crucial part for building predictive control. *Energy and Buildings*, *56*, 8–22.

Ramos, J. S., Moreno, M. P., Delgado, M. G., Dominguez, S. A., & Cabeza, L. F. (2019). Potential of energy flexible buildings: Evaluation of DSM strategies using building thermal mass. *Energy and Buildings*, *203*, e109442

Rhee, K.-N., & Kim, K. W. (2015). A 50 year review of basic and applied research in radiant heating and cooling systems for the built environment. *Building Environment*, *91*, 640-650.

Romani, J., de Gracia, A., & Cabeza, L. F. (2016). Simulation and Control of Thermally Active Building systems (TABS). *Energy and Buildings*, *127*, 22-42.

Roth, K. W., Westphalen, D., Feng, M. Y., Llana, P., & Quartararo, L. (2005). Energy Impact of Commercial Building Controls and Performance Diagnostics: Market Characterization, Energy Impact of Building Faults and Energy Savings Potential. Cambridge, US: A Report for Building Technologies Program.

Saberi-Derakhtenjani, A., Candanedo, J. A., Chen, Y., Dehkordi, V. R., & Athienitis, A.K. (2015). Modeling approaches for the characterization of building thermal dynamics and model-based control: A case study. *Science and Technology for the Built Environment*, *21*, 824-836.

Sartori, I., Napolitano, A., & Voss, K. (2012). Net zero energy buildings: a consistent definition framework. *Energy and Buildings*,*48*, 220-232.

Sibilio, S., Rosata, A., Scorpio, M., Iuliano, G., Ciampi, G., Vanoli, G.P., & de Rossi, F. (2016). A Review of Electrochromic Windows for Residential Applications. *International Journal of Heat and Technology*, *34*(2), S481-S488.

Skandalos, N., & Karamanis, D. (2015). PV glazing technologies. *Renewable and Sustainable Energy Reviews*, *49*, 306-322.

Soria, B., Gerritsen, E., Lefillastre, P., & Broquin, J.-E. (2016). A study of the annual performance of bifacial photovoltaic modules in the case of vertical facade integration. *Energy Science and Engineering*, *4*(1), 52-68.

Statistics Canada. (2022). Provincial and Territorial Energy Profiles – Quebec. https://www.cer-rec.gc.ca/en/data-analysis/energy-markets/provincial-territorial-energy-profiles/provincial-territorial-energy-profiles-quebec.html

Szokolay, S. (2014). Introduction to architectural science: The basis of sustainable design (3rd ed.). London, UK: Routledge.

Tariku, F., Kumaran, M., & Fazio, P. (2008). Thermostat setback effect in whole building performance. Building Physics Symposium, Leuven, BE, October 29-31, 2008.

Tartarini, F., Schiavon, S., Cheung, T., & Hoyt, T. (2020). CBE Thermal Comfort Tool: Online tool for thermal comfort calculations and visualizations. SoftwareX, 12.

Tina, G. M., Scavo, F. B., & Gagliano, A. (2020). Multilayer Thermal Model for Evaluating the Performances of Monofacial and Bifacial Photovoltaic Modules. *IEEE Journal of Photovoltaics*, *10*(4), 1035-1043.

Tzempelikos, A. (2008). The impact of venetian blind geometry and tilt angle on view, direct light transmission and interior illuminance. *Solar Energy*, *82*, 1172-1191.

van Moeseke, G., Bruyere, I., & De Herde, A. (2007). Impact of control rules on the efficiency of shading devices and free cooling for office buildings. *Building Environment*, *42*(2), 784-793.

Vijayan, D. S., Sivasuriyan, A., Patchamuthu, P., & Jayaseelan, R. (2022). Thermal Performance of Energy-efficient Buildings for Sustainable Development. *Environmental Science and Pollution Research*, *29*(34), 51130-51142.

Wang, L. -S., Ma, P., Hu, E., Giza-Sisson, D., Mueller, G., & Guo, N. (2014). A study of building envelope and thermal mass requirements for achieving thermal autonomy in an office building. *Energy and Buildings*, *78*, 79-88.

Wienold, J., & Christoffersen, J. (2005). Towards a new daylight glare rating. Proceedings of the 10 Europäischer Lichtkongress, Berlin, Germany, September 19-21, 2005.

Wienold, J., & Christoffersen, J. (2006). Evaluation methods and development of a new glare prediction model for daylight environments with the use of CCD cameras. *Energy and Buildings*, *38*, 743-757.

Whitmore, J., & Pineau, P. -O. (2021). State of Energy in Quebec 2021. Chair in Energy Sector Management, HEC Montreal, prepared for the Ministry of Energy and Natural Resources, 26,38.

Yuan, S., Vallianos, C., Athienitis, A. K., & Rao, J. 2018. A study of hybrid ventilation in an institutional building for predictive control. *Building and Environment*, *128*, 1-11.

Yucel, K. T., Basyigit, C., & Ozel, C. (2003). Thermal insulation properties of expanded polystyrene as construction and insulating materials. Proceedings of 15th Symposium on Thermophysical Properties, Boulder, US, July 22-27, 2003.

Zhao, O., Zhang, W., Xie, L., Wang, W., Chen, M., Li, Z., Li, J., Wu, X., Zeng, X., & Du., S. (2022). Investigation of indoor environment and thermal comfort of building installed with bifacial PV modules. *Sustainable Cities and Society*, *76*: e103463.

Zhou, H., & Brooks, A.L. (2019). Thermal and mechanical properties of structural lightweight concrete containing lightweight aggregates and fly-ash cenospheres. *Construction and Building Materials*, *198*, 512-526.

Zoller, A. (1913). Hohle Glasscheibe. German Patent Application. No. 387655.

Appendix A: Python Programming Code

A.1. Thermal Resistance-Capacitance Model

```
"""
Created on Tue Sep 20 15:05:28 2022
Thermal Simulation model for Test Cell 4 (or test cell 3 with adjustments)
author: John R. Hill
"""
import matplotlib.pyplot as plt
import numpy as np
import pandas as pd
"""
Zone Dimensions
"""
Lslab = 0.102     # m; Concrete slab thickness
Linsul = 0.06985 # m; Insulation thickness
H = 2.855         # m; height of zone
W = 3.403         # m; width of zone
L = 3.050         # m; depth of zone
He = 3.048        # m; external height
Af = W*L          # m; Floor Area
Afc = (W-0.1016)*(L-0.1016)  # Concrete floor area (W-Wins) * (L-Wins)
Vol = H * Af      # m^3; Zone volume
"""
Window, Door, and PV dimensions
"""
Awin = 3 * 1.954 * 0.986 # m^2; window area
Ad = 1.8                 # m^2; Door area
Acell = (0.15675)**2     # m^2; PV cell area
APV = 2 * 36 * Acell     # m^2: Total PV cell areas
CR = APV/(Awin * 2/3)
WWR = (Awin-APV)/(He*W)
print('Window-to-Wall Ratio =', "{:.2f}".format(WWR*100), '%')
WWR_PV = (Awin-APV)/(H*W)
"""
# Wall Net Areas
"""
A1 = W * H - Awin            # m^2; South (window) wall
A2 = L * H                   # m^2; West wall
A3 = A2                      # m^2; East Wall
A4 = W * H - Ad              # m^2; North (back) wall
A5 = L * W                   # m^2; Ceiling
A6 = A5                      # m^2; Floor
A7 = Awin                    # m^2; Window
Aw = A1 + A2 + A3 + A4 + A5  # m^2; Total Wall Area
"""
gypsum board (wall) properties
"""
L1 = 0.026         # 2 layers
```

```
rho1 = 800          # density (kg/m^3)
k1 = 0.16           # thermal conductivity (W/mK)
c1 = 750            # specific heat (J/kgK)
L2 = L1; L3 = L1; L4 = L1; L5 = L1
rho2 = rho1; rho3 = rho1; rho4 = rho1; rho5= rho1
k2 = k1; k3 = k1; k4 = k1; k5 = k1
c2 = c1; c3 = c1; c4 = c1; c5 = c1
"""
Window R-value COG
"""
RDG = 0.686    # Thermal Resistance DG
fDG = 0.28     # weighting factor
RTG = 1.112    # Thermal Resistance TG
fTG = 0.28     # weighting factor
RQG = 1.383    # Thermal Resistance QG
fQG = 0.28     # weighting factor
ff  = 1 - (fDG + fTG + fQG)  # frame ratio
Rwina = 1/((fDG/RDG)+(fTG/RTG)+(fQG/RQG)+(ff/2)) # m^2*k/W
"""
Wall and window Azimuth angle
"""
psi = 0                              # deg (South Facing)
alpha_s = 0.3                        # wall absorptances
h1 = 8.3; h2 = h1; h3 = h1; h4 = h1 # Coefficients for surfaces (W/m^2*K)
h5 = 9; h6 = 9.3; h7 = 8.3
hsurf = np.array([h1, h2, h3, h4, h5, h6, h7])
"""
Infiltration Conductance
"""
ach = 0.325    # 1/h; assuming low ach to outdoors (local air exchange)
ach2 = 0.425   # 1/h; assuming higher air exchange between other zones
cpa = 1000     # J/kgK. cpa at const vol = 718; # cpa at const pressure =
1000
rhoa = 1.2     # kg/m^3
Uinf = (ach  * Vol * rhoa * cpa)/3600   # W/K
Uadj = (ach2 * Vol * rhoa * cpa)/3600   # W/K
"""
Wall Resistances (m^2*K/W)
"""
R1 = 6.377             # RSI
R2 = 2; R3 = 2; R4 = 2 # Interior Walls assumed to be 2 RSI
R5 = 2.284             # RSI; Ceiling & Roof Thermal Resistance
"""
Concrete Floor Mass Properties and dimensions
"""
em   = 0.92    # emissivity of concrete (LWC)
L6   = 0.1016  # m; effective slab thickness
k6   = 0.872   # W/m*K; thermal conductivity (LWC, using 0.872)
rho6 = 1995    # kg/m^3; density of concrete (LWC using 1995)
c6   = 913     # J/kg*K; Specific Heat (LWC, using 913)
Rins = 1.77    # K/W; insulation under slab (1.77 from manufacturer)
R6 = (L6/k6) + (1/h6) + Rins # Thermal Resistance
"""
```

```
wall conductances
"""
u1 = 1/(R1-(L1/k1)-(1/h1))
u6 = 1/(R6-(L6/k6)-(1/h6))
"""
Location Data and Solar Calcs
"""
LAT = 45.5                    # deg; Latitude
beta = 90                     # deg; tilt angle (vertical STPV window)
nd = np.array([60, 60, 61])   # day number (Mar 1-2) )
rhog = 0.95                   # ground reflectance with snow

aa = np.pi/180                # for saving space below (rad to deg)
delta = 23.45 * np.sin(360 * ((284+nd)/365)*np.pi/180)
delta = np.repeat(delta,240) # declination angle
ts = (np.arccos(-np.tan(LAT*aa)*np.tan(delta*aa)))*(1/15)*(1/aa) # sunset
time
x = 3
itd = np.reshape((np.tile(np.arange(0,240),(x,1))),x*240)/10
#itc = np.arange(0, 720)/10   # time array
t_it = (itd-12)               # solar time for solar radiation calculations
ha = 15 * t_it                # hour angles
ha_den = ha - 1*10**-5
has = ts * 15                 # hour angle at sunset
# solar altitude
alpha = np.arcsin(np.cos(LAT*aa) * np.cos(delta*aa) * np.cos(ha*aa) +
                  np.sin(LAT*aa) * np.sin(delta*aa))*(abs(t_it) < abs(ts))
zenith = 90 - (alpha/aa)      # zenith angle
phi = np.arccos((np.sin(alpha)*np.sin(LAT*aa)
-np.sin(delta*aa))/(np.cos(alpha)*np.cos(LAT*aa)))*((ha*aa)/abs((ha*aa)-
1*10**-6))
phi[np.logical_and(phi>90,phi<270)] = 0
phi[360] = 0; phi[120] = 0    # Gives nan
# incidence angles
cos_incidence = np.cos(alpha)*np.cos(abs(phi))*np.sin(beta*aa)
- np.sin(alpha)*np.cos(beta*aa)
incidence = np.arccos((cos_incidence + abs(cos_incidence))/2)
LON = 73.6 # deg; Longtitude
beta = 90  # deg; tilt angle (vertical STPV window)
"""
Import solar radiation data from excel
"""
ita = np.arange(0,720)/10
solrad = pd.read_excel('feb 28-mar2 - test.xlsx', 'Sheet1', usecols = 'CI')
solrad = solrad.values.tolist()
solrad = np.array(solrad[195:675])
solrad1 = solrad[0:240]
solrad2 = solrad[240:480]
solrad = np.array([solrad1, solrad1, solrad2])
solrad = np.reshape(solrad, (720,1))
"""
Clear Day - Hottel (1976)
"""
```

```
A = 0.058 # km; altitude
r0 = 1.03; r1 = 1.01; rk = 1                  # Hottel Const: Midlat (win)
a0 = r0 * (0.4237 - 0.00821 *(6-A)**2)
a1 = r1 * (0.5055 + 0.00595 *(6.5-A)**2)
ak = rk * (0.2711 - 0.01858 *(2.5-A)**2)
tb = a0 + a1 * np.exp(-ak/np.cos(zenith*aa)) # Beam Transmittance
td = 0.2710 - 0.2939 *tb                      # Diffuse Transmittance
Ssc = 1362                                    # W/m2; Solar Constant
Sonn = Ssc*(1+0.033*np.cos(360*(nd/365)*aa)) # W/m2; norm SR outside atm
Sonn = np.repeat(Sonn, 240)
Soh = Sonn * np.sin(alpha)                    # W/m2; Horizontal ET SR
Sn = tb * Sonn
Sb = Sonn * tb * np.cos(incidence)            # W/m^2; Beam radiation
Sds = Sonn * np.sin(alpha) * td * ((1 + np.cos(beta*aa))/2)
# W/m2; Diffuse Sky Radiation with view factor to window (Sds)
Sdg = (Sonn * np.sin(alpha)* (td + tb) * rhog * ((1-np.cos(beta*aa))/2))
#W/m2; Ground reflected solar radiation (Sdg)
St = Sb + Sds + Sdg  # W/m2; Total Incident Solar Radiation
St = np.reshape(St, (720,1))
Sth = Sonn * np.sin(alpha) * (tb + td)        # W/m2; Total Horz. SolRad.
Sth = np.reshape(Sth, (720,1))
"""
Glazing Properties
"""
kL = 0.02                          # extinction coefficient * glazing thickness
ng = 1.53                          # refractive index
# angle of refraction and component reflectivity
incidence_p = np.arcsin(np.sin(incidence)/ng)
bb = (np.sin(incidence - incidence_p) / np.sin(incidence + incidence_p)) ** 2
cc = (np.tan(incidence - incidence_p) / np.tan(incidence + incidence_p)) ** 2
r_it = 0.5 * (bb + cc)             # component reflectivity
a_it = np.exp(-kL / (1 - (np.sin(incidence) / ng) ** 2) ** 0.5)

# Beam transmittance, tau, reflectance, rho, absorptance, alpha of glazing:
# Single Glazing
tau_it = ((1 - r_it) ** 2 * a_it) / (1 - r_it ** 2 * a_it ** 2)
rho_out_it = r_it +(r_it *(1 - r_it)**2 *(a_it)**2)/ (1-(r_it**2)*(a_it)**2)
alphag_s = 1 - rho_out_it - tau_it
# Double Glazing
tau_eff_d_it = (tau_it) ** 2 / (1 - (rho_out_it) ** 2)
# absorptances of glazings
alpha_in = alphag_s * (tau_it) ** 2 / (1 - (rho_out_it)**3)
alpha_mid = alphag_s * ((tau_it) / (1 - (rho_out_it) ** 2))
+alphag_s*alpha_in
alpha_out = alphag_s
tau = np.reshape(tau_eff_d_it, (720,1))
tau = tau
tau2 = tau[240:480]
tau3 = tau[480:720]
tau = np.array([tau2, tau2, tau3])
tau = np.reshape(tau, (720,1))
"""
blind control strategies
```

```
"""
dnt = np.arctan((np.tan(alpha))/(np.cos(phi))) # Profile Angle
"""
Horizontal
"""
beta_hz = 90
"""
Cut-Off Clear
"""
beta_CO = np.zeros(len(ita))
for i in range(len(ita)):
    if dnt[i]/aa > 45:
        beta_CO[i] = 90
    else:
        beta_CO[i] = 180 - 2 * dnt[i]/aa
"""
Always Open Clear
"""
beta_AO  = 90 - (dnt/aa)/2
"""
Hybrid Strategy
"""
beta_hyb = np.zeros(len(ita))

for i in range(len(beta_hyb)):
    if t_it[i] >= -6 and t_it[i] <= -3:
        beta_hyb[i] = beta_AO[i]
    elif t_it[i] >= 4 and t_it[i] <= 8:
        beta_hyb[i] = beta_AO[i]
    else:
        beta_hyb[i] = beta_CO[i]
"""
setting control strategy
"""
beta_set = beta_hz    # degrees; 90 deg = horizontal
"""
Transmittance due to blinds - Clear day
"""
ab = (-(beta_set-80)**2)/1900  # Change (beta_set) for dif beta strategies
ba = np.exp(ab)
c = (-4.917*10**-7)*((incidence/aa)**4)
e = (0.00009)*((incidence/aa)**3)
f = (-0.00567)*((incidence/aa)**2)
g = 0.13 * incidence/aa
tau_bl_TG = 0.55 * (ba) * (c + e + f + g - 0.00437)
tau_bl_QG = 0.55 * (ba) * (c + e + f + g - 0.00437)
tau_bl = (tau_bl_QG +tau_bl_TG)/2
"""
Transmittance due to blinds - Cloudy Day
"""
taubl = np.zeros(len(tau_bl)) # Change (beta_set) for dif beta strategies
tau_bl_dif = (4.5 * 10 **12 *(beta_set**-6))/(np.exp(335/beta_set)-1) + taubl
tau_bl_dif_TG = tau_bl_dif
```

```
tau_bl_dif_QG = tau_bl_dif
tau_bl_dif =(tau_bl_dif_TG + tau_bl_dif_QG)/2
"""
Transmittance of view section
"""
tauDG = np.zeros(len(ita))
tauDG =  tau * 0.8 # low-E
"""
Total transmitted Solar Radiation
    * 'solrad'[i] is the solar radiation data incident on the window,
      change to 'St'[i] for perfectly clear day.
"""
tauwin = np.zeros(len(ita))
for i in range(len(ita)):
    if solrad[i] <= 0.25 * St[i]:
        tauwin[i] = tau[i] * tau_bl_dif[i]
    elif solrad[i] > 0.25 * St[i] and St[i] <= 0.70:
        tauwin[i] = tau[i] * ((tau_bl_dif[i] + tau_bl[i])/2)
    else:
        tauwin[i] = tau_bl[i]
"""
Transmittance of Shade
"""
tauwin = np.reshape(tauwin, (720,1))
taush  = np.zeros(len(ita)) + 1
taush[0:480] = 0.05
taush[480:720] = 1
taush = np.reshape(taush,(720,1))
"""
Transmitted sol radiation (change to Sth for clear day)
"""
G_it = solrad * (Awin-APV) *  ((2/3)* tauwin + (1/3) * tauDG * taush)
Gao_it = alpha_out * solrad2
Gam_it = alpha_mid * solrad2
Gai_it = alpha_in * solrad2
S = np.array(G_it) # Transmitted Solar Radiation array
"""
Exterior Temperature Mar 1-2 2023
"""
Tambx = pd.read_excel('MTL mar1-2.xlsx', 'Sheet1', usecols = 'C')
Tambx = Tambx.values.tolist()
Tamb1 = Tambx[0:24]
Tamb2 = Tambx[24:48]
Tamb = np.array([Tamb1, Tamb1, Tamb2])
Tamb = np.repeat(Tamb,10)
nTo = 23
t = np.linspace(0, 21, nTo+1)
To1 = np.array([-0.5,-1.2,-1.3,-1.3,-1.4,-1.4,-1.7,-2,-1.1,-0.3,0,-0.1,1,1.7,
                2,2.3,1.9,2,2.1,1.6,1.6,0.5,0.9,0])
To = np.array([0,0,-0.2,-0.3,-0.8,-1.1,-1.3,-1.3,-1.2,-1.3,-1.3,-1.3,-1.3,
               -1,0,0.6,0.8,0.9,0.9,1.1,0.9,0.9,-0.2,-1.2])
Dt_crit = 360
Ton = np.sum(To * np.exp(-2j * np.pi * np.arange(4).reshape(-1, 1) / 24 * t)/
```

```
            (nTo + 1), axis=1)
Ton1 =  np.sum(To1 * np.exp(-2j *np.pi*np.arange(4).reshape(-1,1)/24* t)/
              (nTo + 1), axis=1)
print("The mean daily temperature is %4.3f degC" % Ton[0].real)
time = np.linspace(0, 3*24*3600, int(3*24*3600/Dt_crit))
To = Ton[0].real+2*np.sum((Ton[1:]*np.exp(1j*2*np.pi *np.arange(1, 4)/
                          24*time.reshape(-1,1)/3600)).real,axis=1)
To1 = Ton1[0].real + 2 * np.sum((Ton1[1:]*np.exp(1j*2*np.pi*np.arange(1,4)/
                          24*time.reshape(-1,1)/3600)).real,axis=1)
Ta1 = To1[0:480]
Ta1 = np.reshape(Ta1, (480,1))
Taa1 = np.ravel(Ta1)
Ta2 = To[480:720]
Ta2 = np.reshape(Ta2, (240,1))
Taa2 = np.ravel(Ta2)
Ta = np.concatenate((Ta1, Ta2), axis=0)
Taa = np.concatenate((Taa1,Taa2), axis=0)
plt.plot((time/3600)-48, Taa)
plt.xlim(0,24)
plt.grid()
plt.show()
# Stefan Boltzmann Constant
SBC = 5.67 * (10) **-8
"""
Thermal Capacitances and resistances
"""
Cfloor = c6*rho6*Afc*L6                 # Floor Mass
C4 = Cfloor/2                           # Bottom Half the Floor Mass
C3 = C4                                 # Top Half of Floor mass
C5 = (c1*rho1*L1)*(A2 + A3 + A4 + A5)   # Wall Thermal Capacitance (Lumped)
Ro =  (L6/(4*k6*A6)) + (1/(u6*A6))      # 1/4 Fl. + conductance
R34 = L6/(2*k6*A6)                      # Half the therm. Res. of floor
R23 = R34/2                             # 1/4 Thermal Res. of floor
R56 = 0.5/((k2*A2/L2)+(k3*A3/L3)+(k4*A4/L4)+(k5*A5/L5)) # 1/2 TR of wall
R5o = (R56/2) + (1/((A2/R2)+(A3/R3)+(A4/R4)+(A5/R5)))   # 1/2 TR wall to
Adj.Z
R1o = (1/((Uinf) +  (Awin)/Rwina))      # Infiltration
R1i = 1/ Uadj                           # air changes to other zones
R7o = 1/(Awin/Rwina)
"""
Stability Test to select time step
"""
TS = ([(C3/((1/R23)+(1/R34))), (C4/((1/Ro)+(1/R34))),
(C5/((1/R56)+(1/R5o)))])
dtcrit = min(TS)
dt = 360         # dt < dtcrit; Selected ts must be < critical ts
"""
Relative Humidity
"""
RH = pd.read_excel('feb 28-mar2 - test - 2.xlsx', 'Sheet1', usecols = 'BL')
RH = RH.values.tolist()
RH = np.array(RH[195:675])
RH1 = RH[0:240]
```

```
RH2 = RH[240:480]
RH = np.array([RH1, RH1, RH2])
RH = np.reshape(RH*10, (720,1))    # Measured RH %
"""
Ground Temp & Adjacent cells
"""
Tadj = pd.read_excel('feb 28-mar2 - test - 2.xlsx', 'Sheet1', usecols = 'CX')
Tadj = Tadj.values.tolist()
Tadj = np.array(Tadj[195:675])
Tadj1 = Tadj[0:240]
Tadj2 = Tadj[240:480]
Tadj = np.array([Tadj1, Tadj1, Tadj2])
Tadj = np.reshape(Tadj, (720,1))  # Measured adjacent zone temperature (avg)
Tg  = 19                          # Ground Temperature
"""
Qaux
"""
qmax = 550    # W; based off Qwater (eqn 3.1) in thesis
Kp = qmax/2  # Proportional Control Constant
"""
Time series' for Finite Difference method
"""
Tsp = np.zeros(len(ita)); hcf = np.zeros(len(ita)); hrfwa =
np.zeros(len(ita))
hcw = np.zeros(len(ita)); hcc = np.zeros(len(ita)); hcwina
=np.zeros(len(ita))
hcwinwa = np.zeros(len(ita)); hrwinwa = np.zeros(len(ita))
hrwinf = np.zeros(len(ita))
T1 = np.zeros(len(ita)); T2 = np.zeros(len(ita)); T3 = np.zeros(len(ita))
T4 = np.zeros(len(ita)); T5 = np.zeros(len(ita)); T6 = np.zeros(len(ita))
T7 = np.zeros(len(ita)); qaux = np.zeros(len(ita))
"""
Temperature setpoint
"""
Tsp1 = Tsp + 23
Tspa = np.array([24, 24, 24, 24, 24, 24, 21, 21, 21, 23, 23, 23, 23, 23, 23
                 , 23, 21, 21, 21, 21, 23, 23, 23, 23])
Tsp = np.repeat(Tsp,10)
Tsp = np.tile(Tsp,2)
"""
Tsp Mild
"""
Tspmsemiclo = np.array([16,16,16,16,16,17,18,19,20,21,21.5,21,24,24,
                                  24,21.5,21.5,21.5,21.5,21.5,21.5,16,16,16])
Tspmclo = np.array([18,19,20,22,22,20,20,20,20,24,24,24,24,24,
                                        24,22,22,22,21.5,21.5,21.5,18,18,18])
Tspmsunny = np.array([12,12,12,12,13,14,15.5,16.5,17.5,21.5,21,24,24,24,24,
                                           22,22,22,22,21.5,21.5,14,14,14])
"""
Tsp Cold
"""
Tspcclo = np.array([22,22,24,24,24,24,20,20,20,24,24,24,24,24,24,
                                       20,20,22,21.5,21.5,21.5,18,18,18])
```

```
Tspcsc = np.array([18,20,24,24,24,24,19,20,21,22,23,23,23,23,23,22,22,21.5,
                                                    21.5,21.5,21.5,18,18,18])
Tspcsun = np.array([14,23,23,23,23,15,16,17,18,19,22.5,25,25,25,25,22,22,
                                                   22,22,21.5,21.5,14,14,14])
"""
Tsp Very Cold
"""
Tspvcsemiclo = np.array([24,24,24,24,24,24,19,19,20,23,23,24,24,24,24,

24,22,22,22,22,22,22,18,18])
Tspvcclo = np.array([24,24,24,24,24,24,20,20,20,24,24,24,24,24,24,24,20,22,

22,21.5,21.5,21.5,18,18])
Tspvcsun = np.array([14,24,24,24,24,15,16,17,18,19,22.5,25,25,25,25,24,22,

22,22,22,21.5,21.5,18,18])
"""
Reference Verification
"""
Tspb = np.array([24, 24, 24, 24, 24, 24, 22, 22, 22, 22, 24, 24, 24, 24, 24
                 , 24, 22, 22, 22, 22, 22, 22, 22, 22])
Tsp3 = np.array([24, 24, 24, 24, 24, 24, 21, 21, 21, 23, 23, 23, 23, 23, 23
                 , 23, 21, 21, 21, 21, 23, 23, 23, 23 ,24, 24, 24, 24, 24, 24
                 , 21, 21, 21, 23, 23, 23, 23, 23, 23, 23, 21, 21, 21, 21, 23
                 , 23, 23, 23, 22, 22, 22, 22, 22, 22, 24, 24, 24, 24, 24, 24
                 , 24, 24, 24, 24, 24, 24, 24, 24, 22, 22, 22, 22])
Tsp3 = np.repeat(Tsp3,10)
Tsp = np.array([Tspa, Tspa, Tspb])
Tsp = np.repeat(Tsp,10)
"""
Set Near Optimal Tsp
"""
Tsp_NO = np.array([Tspa, Tspa, Tspmclo])
Tsp_NO = np.repeat(Tsp_NO, 10)
"""
Internal Gains
"""
qint = np.zeros(len(ita))
qintla = 20          # 20 W for Laptop
qintper = 64         # 64-70 W for 1 person (1.1 - 1.2 met)
qintli =  17.2       # Assuming 17.2 W for LED lighting
qinttot = qintla + qintper + qintli

for i in range(len(qint)):
    if t_it[i] >= -4.1 and t_it[i] <=5:
        qint[i] = qinttot
    else:
        qint[i] = qintla  -18 # qintla - 18 for when laptop off at night
                              # Keep at 20 (laptop only) for Validation
"""
Finite Difference Method
"""
# Initial Estimates
```

```
T1[0] = 20; T2[0] = 23; T3[0] = 21; T4[0] = 19; T5[0] = 21; T6[0] = 22;
T7[0] = 10; hcf[0] = 2; hrfwa[0] = 5
hcw[0] = 2; hcc[0] = 0.8; hrwinwa[0] = 1; hcwina[0] = 1.8
for i in range(len(ita)-1):
    if T2[i] > T1[i]:
        hcf[i+1] = 1.52*((T2[i]-T1[i])**(1/3)) # Convective from floor to air
    else:
        hcf[i+1] = 0.59 * ((T1[i]-T2[i])/1)**(0.25)
    hrfwa[i+1] = em * SBC * 4 * ((((T2[i]+273)+(T6[i]+273))/2)**3)
                        # Radiation from floor to walls
    if T6[i] > T1[i]:
        hcw[i+1] = 1.31*((T6[i]-T1[i])**(1/3)) # Convective bw walls and air
    else:
        hcw[i+1] = 1.31*((T1[i]-T6[i])**(1/3))
    hrwinf[i+1]  = em * SBC * 2 *((((T2[i]+273)+(T7[i]+273))/2)**3)
                        # Radiation from window to floor
    hrwinwa[i+1] = em * SBC * 4 * ((((T7[i]+273)+(T6[i]+273))/2)**3)
                        # Radiation from window to walls
    if T7[i] > T1[i]:
        hcwina[i+1] = 1.31 *((T7[i]-T1[i])**(1/3)) # Conv. Window to air
    else:
        hcwina[i+1] = 1.31 * ((T1[i]-T7[i])*(1/3))
    T1[i+1] = (((T2[i]/(1/(A6*hcf[i])))+(T6[i]/(1/(Aw*hcw[i])))+(Taa[i]/R1o)+
                (T7[i] * Awin * hcwina[i]) +(Tadj[i]/R1i) + 0.4 * qint[i])/
               ((1/(1/(A6*hcf[i])))+(Aw*hcw[i])+(1/R1o)+
                (Awin * hcwina[i])+(1/R1i)))  # Room Air
    T2[i+1] =
(((T1[i]/(1/(A6*hcf[i])))+(T6[i]/(1/(A6*hrfwa[i])))+(T3[i]/R23)+
               (0.75*S[i])+(T7[i]*(Awin*hrwinf[i])) + 0.1 * qint[i])/
              ((1/(1/(A6*hcf[i])))+(A6*hrfwa[i])+(1/R23)+(Awin*hrwinf[i])))
                                            # Floor Surface
    T3[i+1] = ((dt/C3) * (((T4[i]-T3[i])/(R34))+((T2[i]-T3[i])/(R23))))+T3[i]
                                            # 1/4 deep into floor
    T4[i+1] = ((dt/C4)*(((T3[i]-T4[i])/(R34))+((Tg-
T4[i])/(Ro))+qaux[i]))+T4[i]
                                            # 1/4 above floor insulation
    T5[i+1] = ((dt/C5) * (((T6[i]-T5[i])/(R56)+(Tadj[i]-T5[i])/(R5o))))+T5[i]
                              # midway point bw wall surface and adjacent zones
    T6[i+1] =
(((T5[i]/R56)+(T2[i]/(1/(A6*hrfwa[i])))+(T1[i]/(1/(Aw*hcw[i])))+
               (0.25*S[i])+(T7[i]*(Awin*hrwinwa[i])) + 0.4 * qint[i])/
              ((1/R56)+(A6*hrfwa[i])+(Aw*hcw[i])+(Awin*hrwinwa[i])))
                                            # wall surface
    T7[i+1] = ((T2[i] * Awin*hrwinf[i]) + (T1[i] * Awin * hcwina[i]) +
               (T6[i] * Awin*hrwinwa[i])+(Taa[i]/R7o) + S[i] +
              0.1*qint[i])/(Awin*hrwinf[i] + Awin * hcwina[i] +
                            Awin*hrwinwa[i]+(1/R7o))
                                            # window surface
    if (Tsp3[i] - T1[i]) > 0.25:       # check Tsp
        qaux[i+1] = abs(min(qmax, Kp * (Tsp3[i]-T1[i])))
        if (29 - T2[i]) < 2:
            qaux[i+1] = 0
"""
```

```
Daily Heating Load
"""
import scipy.integrate as scint
Qheat2 = scint.trapezoid(qaux[int(3600/dt*24):int(3600/dt*24*2)]
                         ,ita[int(3600/dt*24):int(3600/dt*24*2)],axis=0)/1000
Qheat3 = scint.trapezoid(qaux[int(3600/dt*24*2):int(3600/dt*24*3)]
                         ,ita[int(3600/dt*24*2):int(3600/dt*24*3)]
                         ,axis=0)/1000
print('Qheat day 3 =', Qheat3, 'kWh')
# plot
fig, ax1 = plt.subplots()
place_1 = ax1.plot(ita-48, T2, 'r')
place_3 = ax1.plot(ita-48, T1, 'c')
place_5 = ax1.plot(ita-48, T6, 'm')
place_6 = ax1.plot(ita-48, Tsp3, 'k')
ax1.set_xlabel('Time (hr)')
ax1.set_ylabel('Temperature (C)', color='k')
#ax2.set_ylabel('Ambient Temperature (C)',color='b')
ax1.set_ylim(18,30)
plt.xlim(0,24)
plt.title('March 2nd - Temperature Profiles')
plt.xticks(np.arange(0,25,1))
plt.grid()
plt.show()
"""
For BEFI Calcs
"""
Pavg69 = (sum(qaux[540:570])/30) * 3
print('Pavg 6-9am =', Pavg69, 'Wh')
Pavg48 = (sum(qaux[640:680])/40) * 4
print('Pavg 4-8pm =', Pavg48, 'Wh')



"""
Thermal Comfort
"""
from shapely.geometry import Polygon
Tpr = (0.18*(T2+T6)+0.22*(T6+T6)+0.3*(T6+T7))/(2*(0.18+0.22+0.3))
hc_avg = (hcf + hcw + hcwina)/3
hr_avg = (hrfwa + hrwinf + hrwinwa)/3
Top = ((hc_avg * T1) + (hr_avg * Tpr))/(hc_avg + hr_avg)
Top = np.reshape(Top,(720,1))
Top = Top[560:650]
RH = RH[560:650]
RHmax = 3
RHtest =  RHmax*np.sin(np.pi * (np.arange(240) + 30) / 20 / ts[480:720]) + 20
Topmin1 = (RH/100 - 9.0584)/(-0.4692)
Topmax1 = (RH/100 - 8.3518)/(-0.2958)
Topmin05 = (RH/100 - 8.8596)/(-0.4104)
Topmax05 = (RH/100 - 8.5924)/(-0.3303)
TC1 = np.zeros(len(RH))
```

```
TC05 = np.zeros(len(RH))
for i in range(len(TC1)):
    if Top[i] >= Topmin1[i] and Top[i] <= Topmax1[i]:
        TC1[i] = 0.1 # 6 min = 0.1 hr
    else:
        TC1[i] = 0
for i in range(len(TC05)):
    if Top[i] >= Topmin05[i] and Top[i] <= Topmax05[i]:
        TC05[i] = 0.1 # 6 min = 0.1 hr
    else:
        TC05[i] = 0
TC1 = (sum(TC1)/9) * 100
print('Thermal comfort for PMV +/- 1:', "{:.2f}".format(TC1), '%')
TC05 = (sum(TC05)/9) * 100
print('Thermal comfort for PMV +/- 0.5:', "{:.2f}".format(TC05), '%')
TC05H = np.zeros(len(RH))
for i in range(len(TC05H)):
    if Top[i] > Topmax05[i]:
        TC05H[i] = 0.1  # 6 mins = 0.1 hr
TC05C = np.zeros(len(RH))
for i in range(len(TC05C)):
    if Top[i] < Topmin05[i]:
        TC05C[i] = 0.1  # 6 mins = 0.1 hr
TC05H = sum((TC05H)/9)*100
print('Thermal discomfort for PMV + 0.5 (Slightly Warm):'
      , "{:.2f}".format(TC05H), '%')
TC05C = sum((TC05C)/9)*100
print('Thermal discomfort for PMV - 0.5 (Slightly Cool):'
      , "{:.2f}".format(TC05C), '%')
TC1H = np.zeros(len(RH))
for i in range(len(TC1H)):
    if Top[i] > Topmax1[i]:
        TC1H[i] = 0.1  # 6 mins = 0.1 hr
TC1C = np.zeros(len(RH))
for i in range(len(TC1C)):
    if Top[i] < Topmin1[i]:
        TC1C[i] = 0.1  # 6 mins = 0.1 hr
TC1H = sum((TC1H)/9)*100
print('Thermal discomfort for PMV + 1 (Warm):', "{:.2f}".format(TC1H), '%')
TC1C = sum((TC1C)/9)*100
print('Thermal discomfort for PMV - 1 (Cool):', "{:.2f}".format(TC1C), '%')
"""
Thermal Comfort Plot

Bd1   = Boundary limits for +/- 1.0 PMV of T operative
Bd05  = Boundary limits for +/- 0.5 PMV of T operative
(x,y) = ('Top','RH%')
"""
Bd1 = [(19.34,0),(19.22,5),(19.1,10),(18.99,15),(18.88,20),(18.77,25)
       ,(18.66,30),(18.55,35),(18.44,40),(18.33,45),(18.22,50),(18.12,55)
       ,(18.01,60),(17.91,65),(17.8,70),(17.69,75),(17.59,80),(17.5,85)
       ,(17.4,90),(17.31,95),(17.22,100),(24.96,100),(25.1,95),(25.24,90)
       ,(25.38,85),(25.52,80),(25.68,75),(25.84, 70),(26,65),(26.14,60)
```

```
       ,(26.3,55),(26.48,50),(26.65,45),(26.83,40),(27,35),(27.17,30)
       ,(27.37,25),(27.55,20),(27.74,15),(27.94,10),(28.14,5),(28.32,0)]
Bd05 = [(21.64,0),(21.5,5),(21.36,10),(21.23,15),(21.1,20),(20.96,25),
        (20.84,30),(20.71,35),(20.58,40),(20.46,45),(20.34,50),(20.22,55)
        ,(20.09,60),(19.98,65),(19.86,70),(19.75,75),(19.64,80),(19.53,85)
        ,(19.42,90),(19.31,95),(19.2,100),(23.08,100),(23.2,95),(23.33,90)
        ,(23.46,85),(23.59,80),(23.73,75),(23.87,70),(24.01,65),(24.16,60)
        ,(24.3,55),(24.44,50),(24.6,45),(24.76,40),(24.92,35),(25.08,30)
        ,(25.24,25),(25.4,20),(25.58,15),(25.74,10),(25.92,5),(26.1,0)]

PMV1 = Polygon(Bd1)
PMV05 = Polygon(Bd05)
x,y = PMV1.exterior.xy
a,b = PMV05.exterior.xy
plt.plot(x, y, c="red")
plt.plot(a,b, c="black")
ax = plt.subplot()
ax.scatter(Top, RH)
plt.title('Top vs. RH')
plt.xlabel('Operative Temperature (C)')
plt.ylabel('Relative Humidity (%)')
plt.ylim([15,20])
plt.xlim([18,28])
plt.grid()
plt.show()
```

```
"""
Daylighting Model
"""
# Room dimensions
Lslab = 0.102    # m; concrete slab thickness
Linsul = 0.06985 # m: insulation thcikness
Hr = 2.855 # m; Room Height
Wr = 3.403                  # m; Room Width
Dr = 3.05                  # m; Room Depth
"""
# Window Dimensions
"""
Hwin = 1.954      # m; window height
Wwin = 0.986      # m; window width
Awins = Hwin*Wwin # m^2; Window Area - one section
Awin = 3 * Awins #+ (Hwin*Wwin)  # m^2; Total Window Area
"""
# PV dimensions
"""
APVc = (0.15675)**2   # m^2; Area of one PV cell
APVs = 36 * APVc      # m^2; Area of one PV section
APVt = 2 * APVs       # m^2; Total area of PV for TC4
```

```
Awin_PVs = Awins - APVs # m^2; Transmittable area of one PV section
Awint = 2 * Awin_PVs + 1 * Awins
"""
# Location Data and Solar Calcs
"""
LAT = 45.5 # deg; Latitude
beta = 90  # deg; tilt angle (vertical STPV window)
psi = 0    # deg; south facing window
nd = np.array([60, 61])    # day numbers (Mar 1 & 2)
rhog = 0.9 # ground reflectance with snow
"""
# Solar Calculations (Angles)
"""
aa = np.pi/180 # for saving space below
delta = 23.45 * np.sin(360 * ((284+nd)/365)*np.pi/180)
delta = np.repeat(delta,240) # declination angle
ts = (np.arccos(-np.tan(LAT*aa)*np.tan(delta*aa)))*(1/15)*(1/aa) #sunset time
x = 2
itd = np.reshape((np.tile(np.arange(0,240),(x,1))),x*240)/10
itc = np.arange(0,480)/10
itc1 = np.arange(0,240)/10
t_it = (itd-12)  # solar time for solar radiation calculations
ha = 15 * t_it   # hour angles
has = ts * 15    # hour angle at sunset
alpha = np.arcsin(np.cos(LAT*aa) * np.cos(delta*aa) * np.cos(ha*aa) +
                  np.sin(LAT*aa) * np.sin(delta*aa))*(abs(t_it) < abs(ts))
phi = np.arccos((np.sin(alpha) * np.sin(LAT*aa)
   - np.sin(delta*aa))/(np.cos(alpha)*np.cos(LAT*aa)))*((ha*aa)/abs((ha*aa)-
1*10**-6))
phi[np.logical_and(phi>90,phi<270)] = 0
phi[360] = 0; phi[120] = 0
gamma = phi - psi
# incidence angles
cos_incidence = np.cos(alpha)*np.cos(abs(gamma))*np.sin(beta*aa)
- np.sin(alpha)*np.cos(beta*aa)
incidence = np.arccos((cos_incidence + abs(cos_incidence))/2)

incidence2 = np.arccos((np.cos(alpha)*np.cos(abs(gamma))*np.sin(beta*aa)))
cos_inc2 = np.cos(incidence2)
"""
Illuminance under Overcast sky
"""
pg = 0.7
Ehov = 1000 * (0.3 + 21 * np.sin(alpha))
Ewov = 500 * (0.3 + 21 * np.sin(alpha)) * (1 + pg)
"""
# Illuminance under Clear Conditions
"""
Eo = 133800
c  = 0.21
fn = 1 + 0.033*np.cos(360*nd/365); fn = np.repeat(fn, 240)
m = (1/np.sin(alpha+0.0001))
```

```
Ehsun = Eo * fn * (np.exp(-c * m)) * np.sin(alpha)
Ehsky = 800 + 15500 * ((np.sin(alpha)))**(1/2)
Ehclr = Ehsky + Ehsun
Ewg = 0.5 * pg * Ehclr
Ewsky = 0.5 * Ehsky
Ewsun = Eo * fn * (np.exp(-c * m)) * np.cos(incidence2)
Ewclr = (Ewg + Ewsky + Ewsun)*(abs(t_it) < abs(ts))
import pandas as pd
df = pd.read_excel('feb 28-mar2 - test - 2.xlsx', 'Sheet2', usecols='E')
Ewe = df.values.tolist()
Ewe2 = Ewe[124:604]
Ewe = np.array(Ewe2); Ewe = df.values.flatten()
Ewe = Ewe[124:604]; Ewe = np.reshape(Ewe, (480,1))
Ewclr = np.array(Ewclr); Ewclr = np.reshape(Ewclr, (480,1))
"""
Exterior Luminous Exitance
"""
Mext =  Ewe * (Awin-APV) #Ewclr * 0.63 # 0.63 for horizontal component
"""
Glazing Properties
"""
kL = 0.02 # extinction coefficient * glazing thickness
ng = 1.53 # refractive index
# angle of refraction and component reflectivity
incidence_p = np.arcsin(np.sin(incidence)/ng)
bb = (np.sin(incidence - incidence_p) / np.sin(incidence + incidence_p)) ** 2
cc = (np.tan(incidence - incidence_p) / np.tan(incidence + incidence_p)) ** 2
r_it = 0.5 * (bb + cc) # component reflectivity
a_it = np.exp(-kL / (1 - (np.sin(incidence) / ng) ** 2) ** 0.5)
# Beam transmittance, tau, reflectance, rho, absorptance, alpha of glazing:
# Single Glazing
tau_it = ((1 - r_it) ** 2 * a_it) / (1 - r_it ** 2 * a_it ** 2)
rho_out_it = r_it+(r_it*(1-r_it)**2 *(a_it)**2)/(1-(r_it**2)*(a_it)**2)
alphag_s = 1 - rho_out_it - tau_it
# Double Glazing
tau_eff = (tau_it) ** 2 / (1 - (rho_out_it) ** 2) * 0.8
# absorptances of glazings
alpha_in = alphag_s * (tau_it) ** 2 / (1 - (rho_out_it)**3)
alpha_mid = alphag_s * ((tau_it) / (1 - (rho_out_it) ** 2))
+ alphag_s * alpha_in
alpha_out = alphag_s
"""
Blind control strategies
"""
# Profile angle
d = np.arctan((np.tan(alpha))/(np.cos(phi)))
dpr = d / aa
"""
Cut Off Strategy
"""
beta_CO = np.zeros(len(tau_eff))
for i in range(len(beta_CO)):
    if dpr[i] > 45:
```

```
        beta_CO[i] = 90
    else:
        beta_CO[i] = 180 - 2*dpr[i]
"""
Always Open Strategy
"""
beta_AO = 90 - dpr
"""
Hybrid Strategy
"""
beta_hyb = np.zeros(len(tau_eff))
for i in range(len(beta_hyb)):
    if t_it[i] >= -6 and t_it[i] <= -3:
        beta_hyb[i] = beta_AO[i]
    elif t_it[i] >= 4 and t_it[i] <= 8:
        beta_hyb[i] = beta_AO[i]
    else:
        beta_hyb[i] = beta_CO[i]
"""
Setting Control Strategy
"""
beta_set = beta_hz
"""
Transmittance due to blinds - Clear day - for DG
"""
ab = (-(beta_set-80)**2)/1900
ba = np.exp(ab)
c = (-4.917*10**-7)*((incidence2/aa)**4)
e = (0.00009)*((incidence2/aa)**3)
f = (-0.00567)*((incidence2/aa)**2)
g = 0.13 * incidence2/aa

tau_bl_TG = 0.55 * (ba) * (c + e + f + g - 0.00437) * 0.6
tau_bl_QG = 0.55 * (ba) * (c + e + f + g - 0.00437) * 0.36
tau_bl = (tau_bl_QG +tau_bl_TG)/2

## Add tau for extra glazings
"""
Transmittance due to blinds - Cloudy Day (Diffuse)
"""
tau = np.zeros(len(tau_bl))
tau_bl_dif = (4.5 * 10 **12 *(beta_set**-6))/(np.exp(335/beta_set)-1)+tau
tau_bl_dif_TG = tau_bl_dif * 0.6
tau_bl_dif_QG = tau_bl_dif * 0.36
tau_bl_dif =(tau_bl_dif_TG + tau_bl_dif_QG)/2

tau_semi = (tau_bl)*(5/10) + (tau_bl_dif)*(5/10)

tau_DG = np.reshape(tau_eff, (480,1))
tau_sh = np.zeros(len(itc))
tau_sh_open = np.zeros(len(itc)) + 1
tau_sh_open = np.reshape(tau_sh_open, (480,1))
#tau_sh[240:480] = tau_shade
```

```
tau_sh = np.reshape(tau_sh, (480,1))

tauwin = np.zeros(len(Ewe))
for i in range(len(tauwin)):
     if Ewe[i] < (0.7 * Ewclr[i]):
        tauwin[i] = tau_bl_dif[i]
     elif Ewe[i] >= (0.7 * Ewclr[i]):
        tauwin[i] = tau_bl[i]
tauwin = np.reshape(tauwin,(480,1))
"""
Interior Illuminance on Window
"""
Mwi = ((2/3) * Mext * tauwin + (1/3) * Mext * tau_sh_open * 1 *
tau_DG)/(Awin-APV)
"""
View Factors
"""
H = Hr/Wr
W = Dr/Wr
a = W * np.arctan(1/W); b = np.sqrt((H**2)+(W**2)); c = np.arctan(1/b)
d = H * np.arctan(1/H); A = 1 + W**2; B = 1 + H**2; C = 1 + W**2 + H**2
D = H**2 + W**2; E = W**2; G = H**2

f1 = a - b*c + d
f2 = A*B/C
f3 = ((E*C)/(A*D))**E
f4 = ((G*C)/(B*D))**G
f5 = np.pi*W

F21 = (f1+0.25*np.log(f2*f3*f4))/f5
# Wall and Floor areas
A1 = Hr * Wr    # Surface 1 = window + window wall
A2 = Dr * Wr    # Surface 2 = Floor
A3 = 2 * (Dr * Hr) + (A1) + A2  # Surface 3 = 2 side walls+Back wall+ceiling
# Surface Refelectance
rhowa = 0.65      # Check goodness of fit for different wall reflectances
rhofl = 0.25
rhowi = 0.15
# Effective reflectances
rho1 = (rhowa * (A1-Awin) + rhowi * Awin)/A1
rho2 = rhofl
rho3 = rhowa  # all walls + ceiling the same reflectance
# View Factors
F11 = 0;   F12 = F21 * (A2/A1); F13 = 1 - F12
F21 = F21; F22 = 0; F23 = 1 - F21
F31 = F13 * (A1/A3); F32 = F23 * (A2/A3); F33 = 1 - F31 - F32
"""
Radiosity Matrix
"""
R = np.array([[1-rho1*F11, -rho1*F12, -rho1*F13],
              [-rho2*F21, 1-rho2*F22, -rho2*F23],
              [-rho3*F31, -rho3*F32, 1-rho3*F33]])
from numpy.linalg import inv
```

```
Rinv = inv(R)
"""
Initial Luminous exitances
"""
M0 = Mwi/(1) * Rinv[0,0]
M1 = Mwi * Rinv[1,0]
M2 = Mwi * Rinv[2,0]
"""
Finding Illuminance on the Workplane
"""
DFW = 0
Wwint = 3 * Wwin # m; width of window
Hwp = 0.8        # m; Workplane height
S = 1.55         # m; Points on workplane at different distances from window
DWW = DFW - Hwp
y = (DWW + Hwin)
x = Wwint/2
z = S
Ac = np.arctan(x/z)
Bc = z/(np.sqrt((y**2)+(z**2)))
Cc = np.arctan(x/(np.sqrt((y**2)+(z**2))))
FS = (Ac-Bc*Cc)/(2*np.pi)
CFS1 = 2 * FS
CFS2 = 0 #np.zeros(len(CFS1))
CFS3 = 1 - CFS1 - CFS2
"""
Workplane Illuminance
"""
Ewp = (CFS1*M0 + CFS2*M1 + CFS3*M2)
Ewp = np.reshape(Ewp, (480,1))

df = pd.read_excel('feb 28-mar2 - test - 2.xlsx', 'Sheet2', usecols='C')
time = df.values.tolist()
time = time[124:604]
time = np.array(time)
df = pd.read_excel('feb 28-mar2 - test - 2.xlsx', 'Sheet2', usecols='D')
Ewp_meas = df.values.tolist()
Ewp_meas = Ewp_meas[124:604]
Ewp_meas = np.array(Ewp_meas)
SPm = sum(Ewp[70:170])/len(Ewp[70:170])
Mm = sum(Ewp_meas[70:170])/len(Ewp_meas[70:170])
Ewp1 = Ewp[0:240]
Ewp2 = Ewp[240:480]
Ewp1_meas = Ewp_meas[0:240]
Ewp2_meas = Ewp_meas[240:480]
Ewp2 = Ewp[240:480]

plt.plot(itc1, Ewp2, itc1, Ewp2_meas)
plt.xticks(np.arange(0,25, 1))
plt.axis([6,18, 0, 2000])
plt.title('Workplane Illuminance - March 2nd - Overcast Day')
plt.xlabel('Time of Day (hr)')
```

```
plt.ylabel('Illuminance (Lux)')
plt.grid()
plt.show()

SPm2 = sum(Ewp2[70:170])/len(Ewp2[70:170])
Mm2 = sum(Ewp2_meas[70:170])/len(Ewp2_meas[70:170])
EP2 = abs((SPm2-Mm2)/Mm2)*100
print('Error Percentage of February 3rd =', EP2)
D2 = Ewp2[70:170] - Ewp2_meas[70:170]
E2 = D2**2
F2 = np.sum(E2)
G2 = F2/len(Ewp2[70:170])
RMSE2 = np.sqrt(G2)
print('RMSE day 2 =', RMSE2, 'Lux')
CVRMSE2 = (RMSE2/Mm2)*100
print('CVRMSE day 2 =', CVRMSE2, '%')

Ewp1_data = pd.DataFrame(data=Ewp1)
Ewp1_data.to_excel('FromPython4.xlsx', 'Sheet1')
Ewp2_data = pd.DataFrame(data=Ewp2)
Ewp2_data.to_excel('FromPython5.xlsx', 'Sheet1')
"""
Artificial Lighting
"""
DL1 = 0.57 # m; distance from window to luminaire 1
DL2 = 2.57 # m; distance from window to luminaire 2
Hwp = 0.8  # m; height of the workplane
Hr  = 2.855 # m; Height of the room
Ds  = 1.55 # m; distance from window to working point on WP
Ll  = 0.56 # m; length of each luminaire
A = 1 # m^2; desk area
"""
Luminaire Specifications
"""
Io = 6120  # lumens; Initial lumen output of luminaire
Ef = 135   # lm/W; module efficacy
Pl = Io/Ef # W; Power output of each module
"""
Lighting Locations to Sensor location
"""
D1   = Ds - DL1 # Distance from Luminaire 1 to sensor (y-dir)
D2   = DL2 - Ds # Distance from Luminaire 2 to sensor (y-dir)
Hls  = Hr - Hwp # m; luminaire distance above sensor (z-dir)
L1 = np.sqrt((D1)**2 + (Hls)**2)  # m; linear distance from lum 1 to sensor
L2 = np.sqrt((D2)**2 + (Hls)**2)  # m; linear distance from lum 2 to sensor
theta1 = np.arccos(Hls/L1); theta2 = np.arccos(Hls/L2)
# rad; angle between lum 1 & 2 and sensor
eta1 = theta1; eta2 = theta2
# rad; angle between normal from sensor to Luminaire 1 & 2
omega1 = (A/L1) * np.cos(eta1); omega2 = (A/L2) * np.cos(eta2)
# sr; Solid angle between Luminaires and Workplane point
"""
Luminous Flux
```

```
"""
I1 = Io * omega1  # cd; Luminous Flux on Area from Lum 1
I2 = Io * omega2  # cd; Luminous Flux on Area from Lum 2
E1 = I1 * np.cos(theta1)/(L1**2)  # Illuminance from Luminaire 1 on wp pt.
E2 = I2 * np.cos(theta2)/(L2**2)  # Illuminance from Luminaire 2 on wp pt.
"""
Total Illuminanca from Luminaires
"""
Etot = E1 + E2 # Total Illuminance from Luminaires
"""
Occupancy
"""
occupancy = np.zeros(len(itc))
for i in range(len(occupancy)):
    if t_it[i] > -4.1 and t_it[i] <= 5:
        occupancy[i] = 1
    else:
        occupancy[i] = 0
occ_2 = occupancy[240:480]
"""
Uniform Daylight Index
"""
grS = np.zeros(len(itc))

for i in range(len(grS)):
    if Ewp[i] >= 500 and Ewp[i] < 2500:
        grS[i] = 1
    else:
        grS[i] = 0
grS_2 = grS[240:480]
UDIsuff = ((sum(grS_2 * occ_2) * 6)/sum(occ_2 * 6)) * 100
print('UDI Suff =', "{:.2f}".format(UDIsuff), '%')
grG = np.zeros(len(itc))
for i in range(len(grG)):
    if Ewp[i] >= 2500:
        grG[i] = 1
    else:
        grG[i] = 0

grG_2 = grG[240:480]
UDIg = ((sum(grG_2 * occ_2) * 6)/sum(occ_2 * 6)) * 100
print('UDI Glare=', "{:.2f}".format(UDIg), '%')
"""
Reference Control a (lights on during occupancy)
"""
Irefa = Pl * (1) * Ef * occupancy
"""
Reference Control b (lights on/off during occupancy)
"""
dimrefb = np.zeros(len(itc))
for i in range(len(itc)):
    if Ewp[i] > 500:
        dimrefb[i] = 1
```

```
    else:
        dimrefb[i] = 0
Irefb = Pl * (1 - dimrefb) * Ef * occupancy
"""
Dimming Control
"""
dim = np.zeros(len(tau_bl))
for i in range(len(dim)):
    if (500 - Ewp[i]) < 0:
        dim[i] = 1
    elif (500 - Ewp[i]) > 0 and (500 - Ewp[i]) <= 100:
        dim[i] = 0.75
    elif (500 - Ewp[i]) > 100 and (500 - Ewp[i]) <= 250:
        dim[i] = 0.5
    elif (500 - Ewp[i]) > 250 and (500 - Ewp[i]) <= 400:
        dim[i] = 0.25
    elif (500 - Ewp[i]) > 400:
        dim[i] = 0
Iflexa = Pl * (1-dim) * Ef * occupancy
dimfb = np.zeros(len(tau_bl))
for i in range(len(dim)):
    if (500 - Ewp[i]) < 0:
        dimfb[i] = 1
    elif (500 - Ewp[i]) > 0 and (500 - Ewp[i]) <= 100:
        dimfb[i] = 0.825
    elif (500 - Ewp[i]) > 100 and (500 - Ewp[i]) <= 200:
        dimfb[i] = 0.65
    elif (500 - Ewp[i]) > 200 and (500 - Ewp[i]) <= 300:
        dimfb[i] = 0.475
    elif (500 - Ewp[i]) > 300 and (500 - Ewp[i]) <= 400:
        dimfb[i] = 0.3
    elif (500 - Ewp[i]) > 400 and (500 - Ewp[i]) <= 500:
        dimfb[i] = 0.125
    else:
        dimfb[i] = 0

Iflexb = Pl * (1 - dimfb) * Ef * occupancy
plt.plot(itc-24, occupancy*100, itc-24, (1-dimrefb)*occupancy*100,'m-.',
         itc-24, (1-dim)*occupancy*100,itc-24, (1-dimfb)*occupancy*100,'g-.')
plt.xticks(np.arange(0,49,1))
plt.yticks(np.arange(0,101,12.5))
plt.axis([6,18, 0, 105])
plt.title('Dimming Strategies for Artificial Lights')
plt.ylabel('Dimming % (100% = ON)')
plt.xlabel('Time of Day (hr)')
plt.grid('both')
plt.show()
"""
Luminous Flux on Work Area
"""
# Reference a (on for occupancy hours)
I1a = Irefa * omega1
I2a = Irefa * omega2
```

```
# Reference b (on/off during occupancy hours)
I1b = Irefb * omega1
I2b = Irefb * omega2
# Flexible Dimming
I1f = Iflexa * omega1
I2f = Iflexa * omega2
# Flexible Dimming b
I1fb = Iflexb * omega1
I2fb = Iflexb * omega2
"""
Illuminance due to different Lighting Control
"""
# Reference a (occupancy)
E1a = I1a * np.cos(theta1)/(L1**2)  # Illuminance from Lum 1 on wp pt.
E2a = I2a * np.cos(theta2)/(L2**2)  # "" Lum 2
Earta = E1a + E2a
Earta = np.reshape(Earta, (480,1))
Etota = Ewp + Earta
# Reference b (on/off)
E1b = I1b * np.cos(theta1)/(L1**2)  # Illuminance from Lum 1 on wp pt.
E2b = I2b * np.cos(theta2)/(L2**2)  # "" Lum 2
Eartb = E1b + E2b
Eartb = np.reshape(Eartb, (480,1))
Etotb = Ewp + Eartb
# Flexible Dimming
E1f = I1f * np.cos(theta1)/(L1**2)  # Illuminance from Lum 1 on wp pt.
E2f = I2f * np.cos(theta2)/(L2**2)  # "" Lum 2
Eartf = E1f + E2f
Eartf = np.reshape(Eartf, (480,1))
Etotf = Ewp + Eartf
# Flexible Dimming b
E1fb = I1fb * np.cos(theta1)/(L1**2)  # Illuminance from Lum 1 on wp pt.
E2fb = I2fb * np.cos(theta2)/(L2**2)  # "" Lum 2
Eartfb = E1fb + E2fb
Eartfb = np.reshape(Eartfb, (480,1))
Etotfb = Ewp + Eartfb
plt.plot(itc-24,Etota,itc-24,Etotb,'m-.',itc-24,Etotf,itc-24,Etotfb,'g-.')
plt.title('Workplane Illuminance due to Dimming Strategies')
plt.ylabel('Workpane Illuminance (Lux)')
plt.xlabel('Time of Day (hr)')
plt.xticks(np.arange(0,25,1))
plt.axis([6,18, 0, 3000])
plt.grid()
plt.show()
"""
Power from different strategies
"""
Pa = 2 * Pl * occ_2
Qla = sum(Pa/91)*9.1
Pb = 2 * Pl * (occ_2) * (1 - dimrefb[240:480])
Qlb = sum(Pb/91)*9.1
Pf = 2 * Pl * (occ_2) * (1 - dim[240:480])
Qlf = sum(Pf/91)*9.1
```

```
Pfb = 2 * Pl * (occ_2) * (1 - dimfb[240:480])
Qlfb = sum(Pfb/91)*9.1
print('Qlrefa =', "{:.2f}".format(Qla/1000), 'kWh', 'Qlrefb =',
      "{:.2f}".format(Qlb/1000), 'kWh', 'Qlflexa =',
"{:.2f}".format(Qlf/1000),
      'kWh', 'Qlflexb =', "{:.2f}".format(Qlfb/1000), 'kWh' )
"""
Power during peak demand periods
"""
P69a = sum(Pa[60:90]/30)*3
P48a = sum(Pa[160:200]/40)*4

P69b = sum(Pb[60:90]/30)*3
P48b = sum(Pb[160:200]/40)*4

P69f = sum(Pf[60:90]/30)*3
P48f = sum(Pf[160:200]/40)*4

P69fb = sum(Pfb[60:90]/30)*3
P48fb = sum(Pfb[160:200]/40)*4
"""
BEFI Calculations
"""
"""
Flex 1
"""
BEFI1m = (P69a-P69f)/3
BEFIP1m = ((P69a-P69f)/(P69a))*100

BEFI1e = (P48a-P48f)/4
BEFIP1e = ((P48a-P48f)/(P48a))*100

print('BEFI for case 1 (5 dimming levels) flexibility ')
print('BEFI69 =', "{:.2f}".format(BEFI1m), 'W', '; BEFIP69 =',
"{:.2f}".format(BEFIP1m), '%')
print('BEFI48 =', "{:.2f}".format(BEFI1e), 'W', '; BEFIP48 =',
"{:.2f}".format(BEFIP1e), '%')
"""
Flex 2
"""
BEFI2m = (P69a-P69fb)/3
BEFIP2m = ((P69a-P69fb)/(P69a))*100
BEFI2e = (P48a-P48fb)/4
BEFIP2e = ((P48a-P48fb)/(P48a))*100
print('BEFI for case 2 (7 dimming levels) flexibility ')
print('BEFI69 =', "{:.2f}".format(BEFI2m), 'W', '; BEFIP69 =',
"{:.2f}".format(BEFIP2m), '%')
print('BEFI48 =', "{:.2f}".format(BEFI2e), 'W', '; BEFIP48 =',
"{:.2f}".format(BEFIP2e), '%')
```

A.2. STPV Generation

```
"""
```

```
Created on Mon Nov 7 15:17:48 2022
Power generation from PV using King's Model
@author: John Hill
"""
import numpy as np
import matplotlib.pyplot as plt
import pandas as pd
import scipy.integrate as scint
"""
monocrystalline PV Cell
"""
eta_ref = 0.18      # Efficiency
mu_pmp = -0.00456   #
"""
Coefficients for TG window
"""
a  = -2.88
b  = -0.0319  # s/m
dT = 11       # K
"""
Reference parameters and PV area
"""
Umet = 5              # m/s; wind speed
c0   = 1
Tref = 25             # C; reference temperature
Awin = 0.986 * 1.954  # m^2; One Window Section area
APVwin = 2*Awin     # m^2; PV window area
Awint = APVwin + Awin # m^2; Total Window Area
APV1 = 0.15675 ** 2   # m^2; One PV cell area
APV  = 36 * APV1      # m^2; One Window section PV area
APVTC4 = 2 * APV      # m^2;
Ag   = APVTC4         # m^2; Pv area
Iref = 1000           # W/m^2; reference irradiance
c1   = 1
CR = (APV/Awin)
tauR = (1-CR)
print('CR =', CR*100, '%', 'tauR =', tauR*100, '%')
"""
Environmental Parameters
"""
dt = 360    # sec
time = np.arange(0,240)/10

IPV_mar2 = pd.read_excel('feb 28-mar2 - test.xlsx', 'Sheet1', usecols = 'CI')
IPV_mar2 = IPV_mar2.values.tolist()
IPV_mar2 = np.array(IPV_mar2[435:675])
IPV_mar2 = np.reshape(IPV_mar2, (240,1))

plt.plot(time/10, IPV_mar2)
plt.grid()
plt.show()

Tamb = pd.read_excel('MTL mar1-2.xlsx', 'Sheet1', usecols = 'C')
```

```
Tamb = Tamb.values.tolist()
Tamb2 = Tamb[24:48]
Tamb = np.repeat(Tamb2,10)
Tamb = np.reshape(Tamb, (240,1))

plt.plot(time/10, Tamb)
plt.grid()
plt.show()

"""
Solar Angles
"""
aa = np.pi/180
LAT = 45.5 # deg; Latitude
beta = 90  # deg; tilt angle (vertical STPV window)
nd = np.array([60, 60, 61])     # day number (Mar 1-2) )
rhog = 0.95                     # ground reflectance
delta = 23.45 * np.sin(360 * ((284+nd)/365)*np.pi/180)
delta = np.repeat(delta,240)    # declination angle
ts = (np.arccos(-np.tan(LAT*aa)*np.tan(delta*aa)))*(1/15)*(1/aa) # sunset
time
x = 3
itd = np.reshape((np.tile(np.arange(0,240),(x,1))),x*240)/10
itc = np.arange(0, 720)/10  # time array
t_it = (itd-12)             # solar time for solar radiation calculations
ha = 15 * t_it              # hour angles
ha_den = ha - 1*10**-5
has = ts * 15               # hour angle at sunset
# solar altitude
alpha = np.arcsin(np.cos(LAT*aa) * np.cos(delta*aa) * np.cos(ha*aa)
+ np.sin(LAT*aa) * np.sin(delta*aa))*(abs(t_it) < abs(ts))
zenith = 90 - (alpha/aa)    # zenith angle
phi = np.arccos((np.sin(alpha) * np.sin(LAT*aa)
- np.sin(delta*aa))/(np.cos(alpha)*np.cos(LAT*aa)))*((ha*aa)/abs((ha*aa)-
1*10**-6))
phi[np.logical_and(phi>90,phi<270)] = 0
phi[360] = 0; phi[120] = 0
# incidence angles
cos_incidence = np.cos(alpha)*np.cos(abs(phi))*np.sin(beta*aa)
- np.sin(alpha)*np.cos(beta*aa)
incidence = np.arccos((cos_incidence + abs(cos_incidence))/2)
LON = 73.6 # deg; Longtitude
beta = 90  # deg; tilt angle (vertical STPV window)
"""
Clear Day - Hottel (1976)
"""
A = 0.058 # km; altitude
r0 = 1.03; r1 = 1.01; rk = 1 # Hottel Constants: Midlat (winter)
a0 = r0 * (0.4237 - 0.00821 *(6-A)**2)
a1 = r1 * (0.5055 + 0.00595 *(6.5-A)**2)
ak = rk * (0.2711 - 0.01858 *(2.5-A)**2)

tb = a0 + a1 * np.exp(-ak/np.cos(zenith*aa)) # Beam Transmittance
```

```
td = 0.2710 - 0.2939 *tb  # Diffuse Transmittance (Liu & Jordan 1960)
Ssc = 1362 # W/m2; Solar Constant
Sonn = Ssc * (1 + 0.033 * np.cos(360*(nd/365)*aa)) # W/m2; norm SR outside
atm
Sonn = np.repeat(Sonn, 240)
Soh = Sonn * np.sin(alpha)  # W/m2; Horizontal ET SR
Sn = tb * Sonn
Sb = Sonn * tb * np.cos(incidence) # W/m^2; Beam radiation
Sds = Sonn * np.sin(alpha) * td * ((1 + np.cos(beta*aa))/2)
# W/m2; Diffuse Sky Radiation with view factor to window
Sdg = (Sonn * np.sin(alpha)* (td + tb) * rhog * ((1-np.cos(beta*aa))/2))
#W/m2; Ground reflected solar radiation
St = Sb + Sds + Sdg  # W/m2; Total Incident Solar Radiation
St = np.reshape(St, (720,1))
Sth = Sonn * np.sin(alpha) * (tb + td) # W/m2; Total Horizontal Sol Rad
Sth = np.reshape(Sth, (720,1))
Sth2 = Sth[480:720]
IPV = IPV_mar2
"""
# Calculating Tback & Tcell
"""
aa = np.exp(a + ( b * Umet))
Tback = (c1 * IPV) * aa + Tamb
Tcell = Tback + (IPV/Iref) * dT
Pmod = c0*(eta_ref)*(1+mu_pmp*(Tcell-Tref))*(IPV*Ag)

plt.plot(time/10, Tcell, time/10, Tback)
plt.title('Tback and Tcell')
plt.grid()
plt.show()
"""
Backside PV generation
"""
tau1 = 0.7
tau2 = 0.7
tau3 = 0.7

rho1 = 0.1
rho2 = 0.1
rho3 = 0.1
rhobl = 0.9

IbTG = ((tau1 * rho1 + rhobl * tau1**3) * IPV_mar2) * tauR
IbQG = ((tau1 * rho1 + (rho2 * tau1**3) +
         (rhobl * tau1**5)) * IPV_mar2) * tauR

Itot = IbTG/2 + IPV_mar2 + IbQG/2
Ib = (IbTG/2 + IbQG/2)

plt.plot(time/10, IPV_mar2, time/10, Ib, time/10, Itot)
plt.grid()
plt.show()
```

```
aa = np.exp(a + ( b * Umet))

Tback = (c1 * Itot) * aa + Tamb

Tcell = Tback + (Itot/Iref) * dT

Pmod2 = c0*(eta_ref)*(1+mu_pmp*(Tcell-Tref))*((IPV*Ag)+(Ib*Ag))
"""
Electrical Losses
"""
EL1 = 0.05    # shading
EL2 = 0.05    # soiling
EL3 = 0.01    # light induced degredation
EL4 = 0.04    # inverter
EL5 = 0.02    # mismatch
EL6 = 0.01    # wiring
ELtot = (1-EL1)*(1-EL2)*(1-EL3)*(1-EL4)*(1-EL5)*(1-EL6)
Pel = Pmod*ELtot
Pel2 = Pmod2*ELtot
plt.plot(time, Pel2, time, Pel, time, (Pel2-Pel))
plt.xticks(np.arange(0,25,2))
plt.xlim([6,18])
plt.ylim([0,100])
plt.title('STPV Window Power Generation')
plt.xlabel('Time (hr)')
plt.ylabel('Power (W)')
plt.grid()
plt.show()
"""
Increase From mono- to bifacial
"""
Pinc = ((Pel2[70:175]-Pel[70:175])/Pel[70:175])*100
Pinc[45] = Pinc[5]
Pincav = sum(Pinc)/len(Pinc)
print('Average Percent increase of bifacial PV', Pincav, '%')
Pavg69 = sum(Pel[60:90]/30) * 3
print('Pavg69', Pavg69, 'Wh')
Pavg48 = sum(Pel[160:200]/40) * 4
print('Pavg48', Pavg48, 'Wh')
Pbi69 = sum(Pel2[60:90]/30) * 3
print('Pbi69', Pbi69, 'Wh')
Pbi48 = sum(Pel2[160:200]/40) * 4
print('Pbi48', Pbi48, 'Wh')
BEFI69 =(Pavg69*3-Pbi69*3)/3
BEFIP69 =(Pavg69*3-Pbi69*3)/(Pavg69*3)
Pgen_bf = scint.trapezoid(Pel2[int(0):int(3600/dt*24)],
                      time[int(0):int(3600/dt*24)], axis=0)/1000
print('P generated bf =', Pgen_bf, 'kWh')
Pgen_mf = scint.trapezoid(Pel[int(0):int(3600/dt*24)],
                      time[int(0):int(3600/dt*24)], axis=0)/1000
print('P generated mf =', Pgen_mf, 'kWh')
Pin_daily = (Pgen_bf-Pgen_mf)/(Pgen_mf)*100
print('Daily increase of bifacial PV', Pin_daily, '%')
```

```
"""
#Thermal Energy transmitted
"""
IPV_t_TG = IPV * tauR * (tau1)**3
IPV_t_QG = IPV * tauR * (tau1)**4

IPV_t = (IPV_t_TG + IPV_t_QG)/2

IPV_t = scint.trapezoid(IPV_t[int(0):int(3600/dt*24)],
time[int(0):int(3600/dt*24)], axis=0)/1000 #* 1e-6 * 3600 * 0.27778
print('Daily Thermal Energy =', IPV_t, 'kWh')

print('Total Daily Solar gains =', sum(IPV_t),'kW')
```

Appendix B: Control Strategies

B.1. Temperature Setpoint Strategies

This section describes the near-optimal temperature setpoints developed by Jalilov and Athienitis (2021). Figures (B.1-B.3) describe strategies for mild, cold, and very cold days, respectively. Each figure has strategies for sunny (clear), semi-cloudy, and cloudy days. Figure (B.2) is shown in chapter 3 as an example but is repeated below for convenience. These setpoint strategies are considered near optimal for their ability to improve both energy flexibility and reduce daily heating loads.

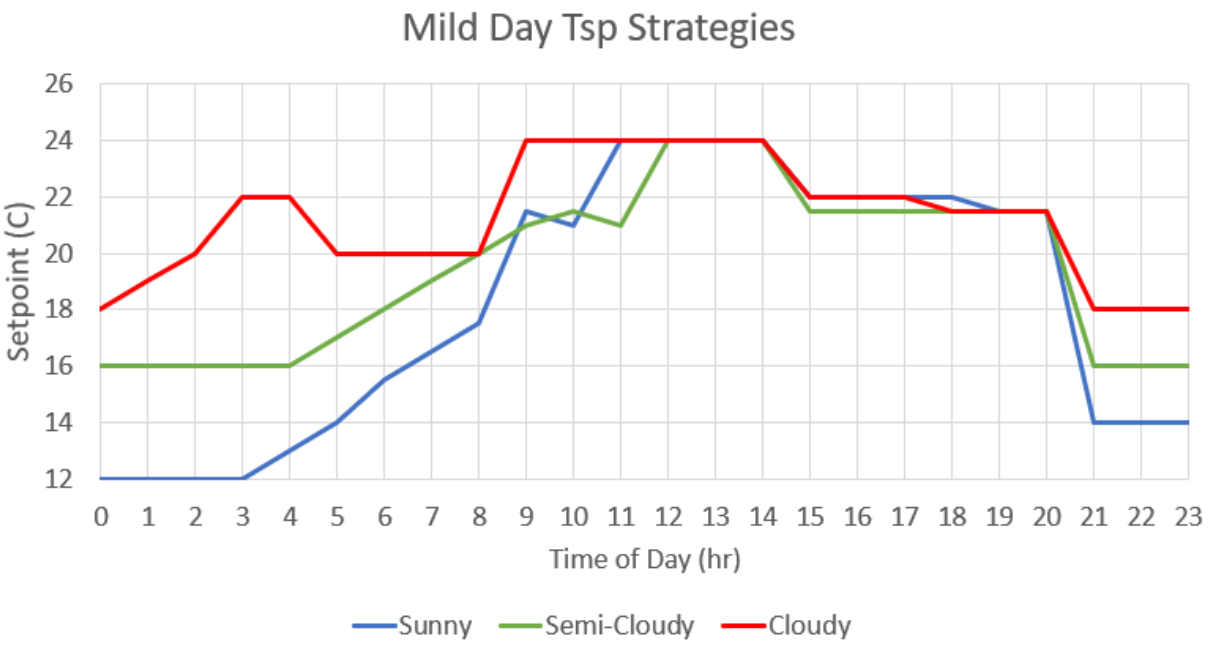

Figure B.1. Mild Day Temperature Setpoint Strategies for Different Solar Radiation Levels.

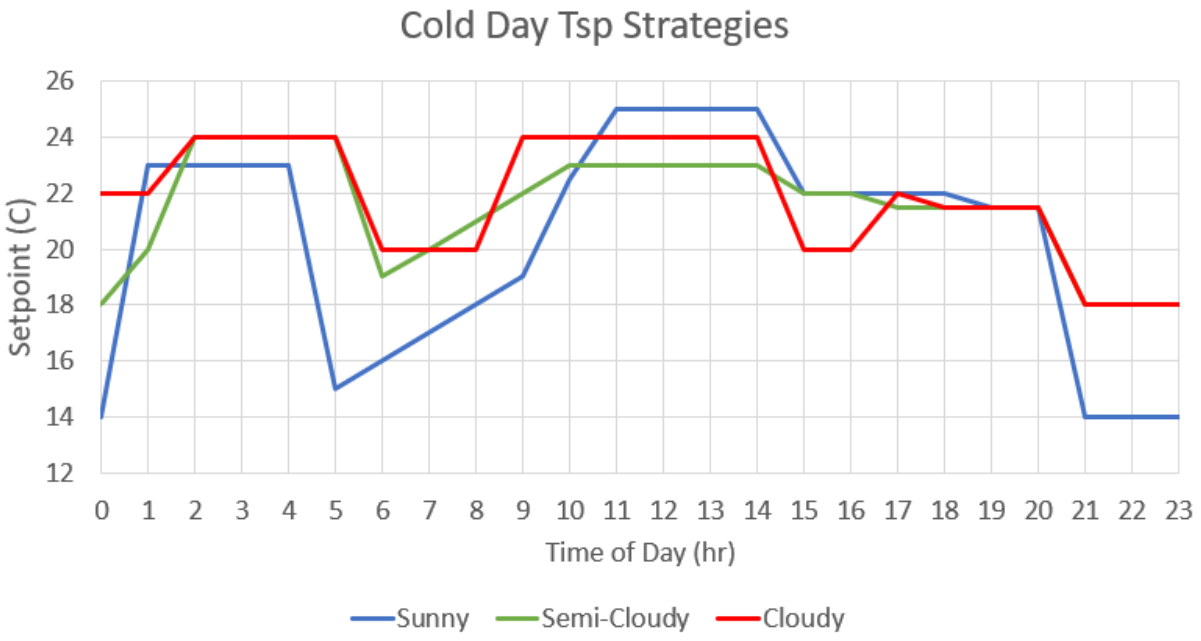

Figure B.2. Cold Day Temperature Setpoint Strategies for Different Solar Radiation Levels.

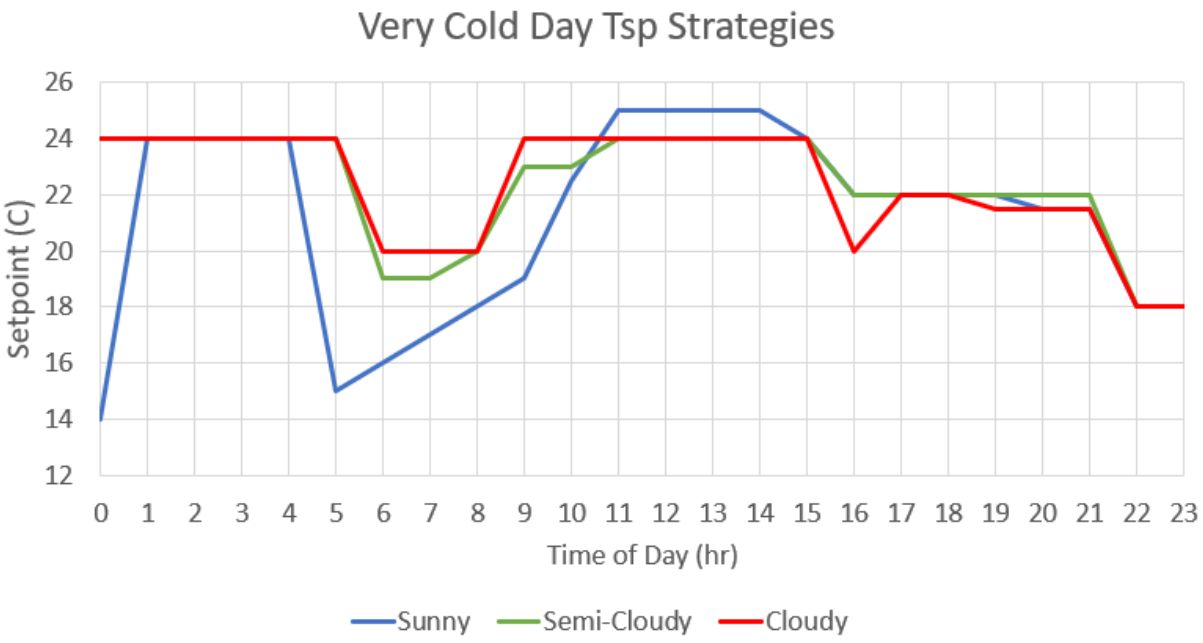

Figure B.3. Very Cold Day Temperature Setpoint Strategies for Different Solar Radiation Levels.

B.2. Artificial Light Dimming

This section describes the dimming of the artificial lights based on the workplane illuminance. The exterior conditions of exterior illuminance were collected with the Li-Cor photometer that was mounted on the aluminum panel of the STPV window. This data can be found in figure (4.4). Furthermore, simulations of dimming strategies below are based on a horizontal blind tilt angle (90°).

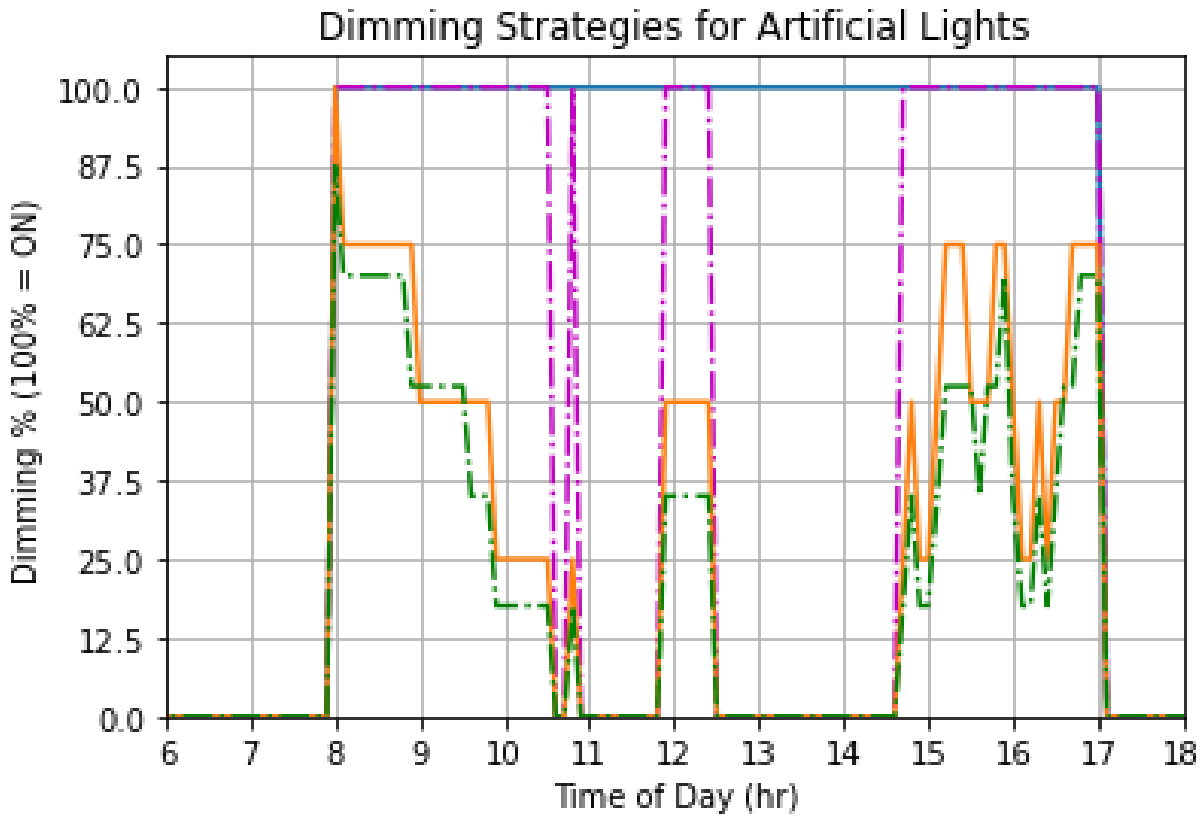

Figure B.4. Simulated Dimming Percentage of Artificial Lights on March 2nd.

The blue curve represents the artificial lights being on for the entire workday and the dashed magenta curve is the control strategy which turns the lights off once the workplane illuminance exceeds the targeted 500 lux. The orange and green dashed curves represent the control strategies of 5- and 7- dimming levels, respectively. Similarly, in figure (B.2), the corresponding workplane illuminance based on the control strategy is shown.

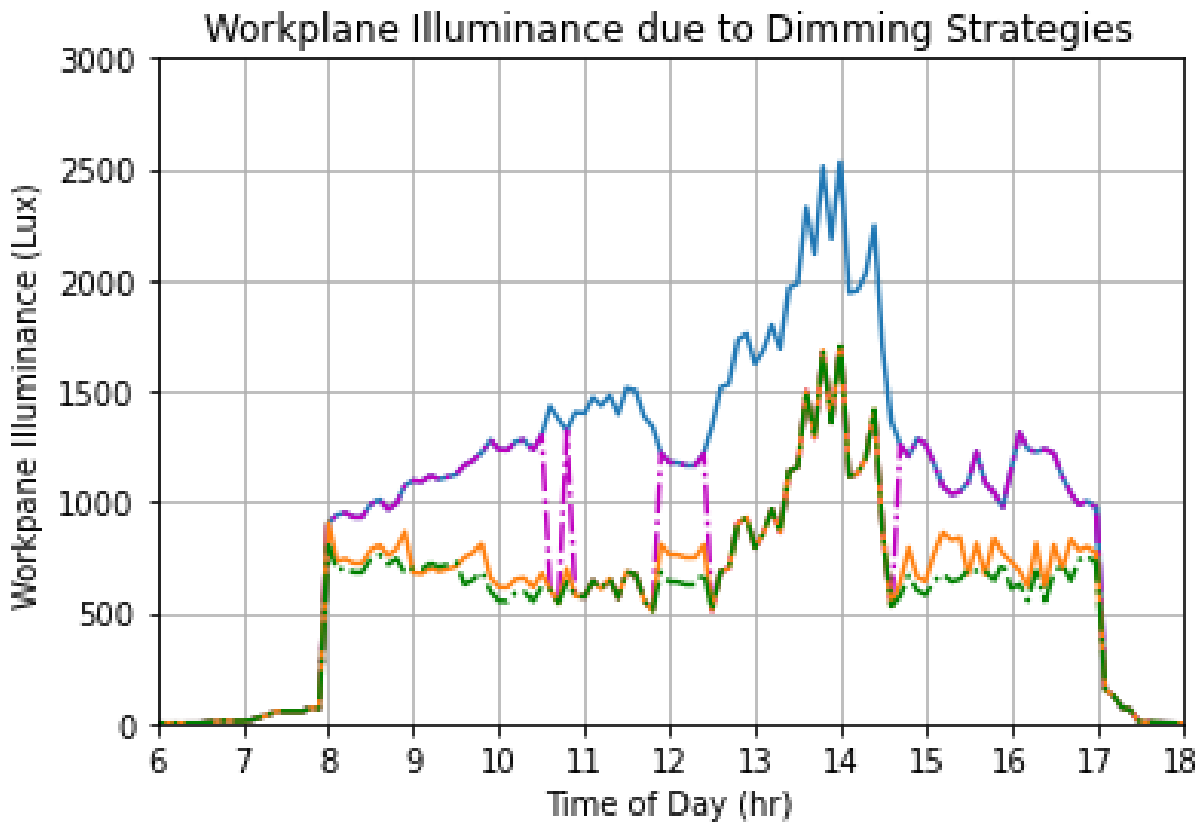

Figure B.5. Simulated Workplane Illuminance due to Dimming Strategies – March 2nd.

Appendix C: Methods and Results

C.1. Solar Geometry Calculations

The following equations describe the relevant solar geometry used in this thesis, the following equation is the apparent solar time, AST (min):

$$AST = LST + ET_n + 4 \cdot (LSM - LON) \tag{C.1}$$

LST is the local standard time (min), LSM is the local standard time meridian (deg), LON is the local longitude (deg), 4 represents the time required for 1 degree of rotation of the Earth, and ET is the equation of time (min), found by:

$$ET_n = \left(9.87 \cdot \sin\left(4\pi \cdot \frac{n-81}{364}\right) - 7.53 \cdot \sin\left(2\pi \cdot \frac{n-81}{364}\right) + 1.5 \cdot \sin\left(2\pi \cdot \frac{n-81}{364}\right)\right) \cdot min \quad \text{(C.2)}$$

where n represents the day of the year. The following equation calculates the hour angle (deg):

$$ha = (AST(hr) - 12 \cdot hr) \cdot \left(15 \frac{deg}{hr}\right) \quad \text{(C.3)}$$

The declination angle is equal to the angular position of the sun at solar noon with respect to the equator plane, for each day of the year:

$$\delta = 23.45(deg) \cdot \sin\left(360 \cdot \frac{284+n}{365} \cdot deg\right) \quad \text{(C.4)}$$

The solar altitude angle, α (deg), may be calculated based on the latitude, L (deg), declination angle, and hour angle. This is the angle between the sun rays and the horizontal:

$$\alpha = \sin^{-1}(cos(L) \cdot \cos(\delta) \cdot \cos(ha) + \sin(L) \cdot \sin(\delta)) \quad \text{(C.5)}$$

The solar azimuth, ϑ (deg), is the angle between the horizontal projection of the sun rays from due south:

$$\vartheta = \cos^{-1}\left(\frac{\sin(\alpha) \cdot \sin(LAT) - \sin(\delta)}{\cos(\alpha) \cdot \cos(LAT)}\right) \frac{ha}{|ha|} \quad \text{(C.6)}$$

The zenith angle, z (deg), may be calculated as:

$$z = 90 \cdot deg - \alpha(deg) \quad \text{(C.7)}$$

The solar surface azimuth angle, γ (deg), is equal to the angle between the projections of the sun rays and of the normal to the surface on the horizontal plane:

$$\gamma = \vartheta - \varphi \tag{C.8}$$

The incidence angle, θ (deg), is the angle between the sun rays and a line normal to the surface:

$$\theta = \cos^{-1}(cos(\alpha) \cdot \cos(|\gamma|) \cdot \sin(\beta) + \sin(\alpha) \cdot \cos(\beta)) \tag{C.9}$$

β (deg) is the tilt angle between the surface and the horizontal. In this study the tilt angle of the window is 90° and static, therefore, the incidence angle may be calculated as follows, as $\cos(90°) = 0$:

$$\theta = \cos^{-1}(cos(\alpha) \cdot \cos(|\gamma|) \cdot \sin(\beta)) \tag{C.10}$$

C.2. Hottel's Model

Hottel (1976) determines the beam radiation transmitted through a clear atmosphere. To calculate the transmittance of the atmosphere:

$$\tau_b = a_0 + a_1 \cdot exp\left(\frac{-a_k}{cos(z)}\right) \tag{C.11}$$

The constant a and subscripts $(0, 1, k)$ depend on the climate and altitude, A (km), and are given by the following three equations:

$$a_0 = r_0 \cdot (0.4237 - 0.00821 \cdot (6 - A)^2) \tag{C.12}$$

$$a_1 = r_1 \cdot (0.5055 + 0.00595 \cdot (6.5 - A)^2) \tag{C.13}$$

$$a_k = r_k \cdot (0.2711 - 0.01858 \cdot (2.5 - A)^2) \tag{C.14}$$

The following table gives the different constant values for different climates:

Table C.1. Constants for Hottel's Model.

Climate	r_0	r_1	r_k
Tropical	0.95	0.98	1.02
Midlatitudes (Summer)	0.97	0.99	1.02
Subarctic	0.99	0.99	1.01
Midlatitudes (Winter)	1.03	1.01	1.00

The solar constant $S_{sc} = 1353$ (W/m^2) and the day number, n, is used to find the normal solar radiation just outside the atmosphere:

$$S_{on_n} = S_{sc} \cdot \left(1 + 0.033 \cdot \cos(360 \cdot \frac{n}{365} \cdot deg)\right) \quad \text{(C.15)}$$

The extraterrestrial solar radiation on a horizontal surface may be calculated with the solar altitude or zenith angle:

$$S_{oh} = S_{on_n} \cdot \sin(\alpha) = S_{on_n} \cdot \cos(z) \quad \text{(C.16)}$$

The normal terrestrial beam radiation may be found:

$$S_n = \tau_b \cdot S_{on_n} \quad \text{(C.17)}$$

Liu & Jordan (1960) developed a correlation to determine the clear sky atmospheric diffuse transmittance for a horizontal plane:

$$\tau_d = 0.2710 - 0.2939 \cdot \tau_b \quad \text{(C.18)}$$

The beam solar radiation incident on an inclined surface is found with the incidence angle:

$$S_b = S_{on_n} \cdot \tau_b \cdot \cos(\theta) \tag{C.19}$$

The diffuse sky radiation incident on the surface is equal to the transmitted diffuse radiation by the view factor between the surface and the sky:

$$S_{ds} = S_{on_n} \cdot \sin(\alpha) \cdot \tau_d \cdot \left(\frac{1 + \cos(\beta)}{2}\right) \tag{C.20}$$

The ground reflected solar radiation may also be estimated with the following equation, based on a reflectance of the ground and the view factor between the ground and the surface:

$$S_{dg} = \left(S_{on_n} \cdot \sin(\alpha) \cdot (\tau_d + \tau_b) \cdot \rho \cdot \left(\frac{1 - \cos(\beta)}{2}\right)\right) \tag{C.21}$$

With the direct beam, diffuse sky, and ground reflected radiation portions, we can calculate a total instantaneous radiation incident on a surface:

$$S_t = S_b + S_{ds} + S_{dg} \tag{C.22}$$

The total horizontal radiation may also be calculated using the equation below:

$$S_{th} = S_{on_n} \cdot \sin(\alpha) \cdot (\tau_b + \tau_d) \tag{C.23}$$

To find the daily totals of incident solar radiation and using the sunrise and sunset times, t_s and $-t_s$, we must calculate the sunset hour angle, hs (deg):

$$hs = \cos^{-1}(-\tan(LAT) \cdot \tan(\delta)) \tag{C.24}$$

$$t_s = hs \cdot \frac{hr}{15 \cdot deg} \tag{C.25}$$

Similarly, the sunrise and sunset times may be calculated for an inclined surface:

$$t_{ss} = min[(hs), (\cos^{-1}(-\tan(LAT - \beta) \cdot \tan(\delta)))] \left(\frac{hr}{15 \cdot deg}\right) \quad \text{(C.26)}$$

Finally, we can find the daily totals of extraterrestrial solar radiation on a horizontal surface, H_{oh}, and the daily solar radiation incident on a south facing surface, H_t, respectively. Equation (C.28) is symmetrical about solar noon:

$$H_{oh} = \int_{-t_s}^{t_s} S_{oh} \cdot dt \quad \text{(C.27)}$$

$$H_t = 2 \cdot \int_{0}^{t_s} S_t \cdot dt \quad \text{(C.28)}$$

C.3. Solar Properties of Windows

The transmittance, τ, reflectance, ρ, and absorptance, α, of windows needs to be calculated to determine how much solar radiation is transmitted into the building, reflected to the environment, or absorbed in the glazing. The conservation of solar radiation can be given by:

$$\alpha + \rho + \tau = 1 \quad \text{(C.29)}$$

Snell's Law determines the component reflectivity based on glass thickness, L, refractive index of glass, ri, which is typically 1.51-1.53, and extinction coefficient, k, 6.96/m for clear plate glass:

$$sin(\theta') = \frac{\sin(\theta)}{ri} \quad \text{(C.30)}$$

The component reflectivity, r, and travelling distance, L', is given by:

$$r = \frac{1}{2} \cdot \left[\left(\frac{sin(\theta - \theta')}{sin(\theta + \theta')} \right)^2 + \left(\frac{tan(\theta - \theta')}{tan(\theta + \theta')} \right)^2 \right] \tag{C.31}$$

$$L' = \frac{L}{\sqrt{1 - \left(\frac{\sin(\theta)}{ri} \right)^2}} \tag{C.32}$$

where L is the horizontal distance through the glass pane. To find the intensity of solar radiation through the glazing layer the following equation is used:

$$S(L') = S_o \cdot b = S_o \cdot \exp(-k \cdot L') \tag{C.33}$$

where b is the fraction of solar radiation available after each reflection in the glazing. To find the transmittance and reflectance we use the following equations:

$$\tau = \frac{(1 - r)^2 \cdot b}{1 - r^2 \cdot b^2} \tag{C.34}$$

$$\rho = r + \frac{r \cdot (1 - r)^2 \cdot b^2}{1 - r^2 \cdot b^2} \tag{C.35}$$

We may then use equation (C.29) to find the absorptance of a glazing layer. For double glazed windows, the effective transmittance may be found using equation (C.36). See Figure C.1 for surface descriptions:

$$\tau_{eff} = \frac{\tau_i \cdot \tau_o}{1 - \rho_j \cdot \rho_k} \tag{C.36}$$

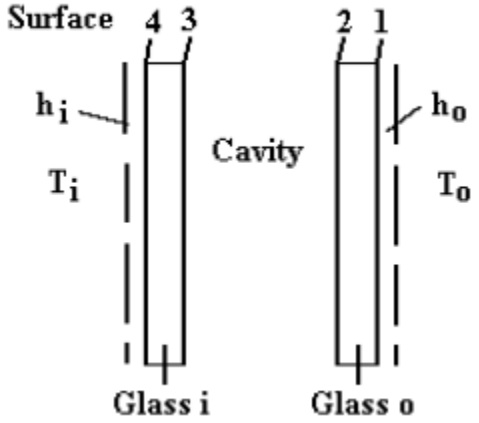

Figure C.1. Glazing Surfaces in a Double-Glazed Window (Athienitis, 1999).

τ_i and τ_o represent the transmittance of the inner and out glazing layers, ρ_j and ρ_k are the reflectance of surface '*j*' and '*k*'. To find the absorptance of each layer equations (C.37 and C.38) are used:

$$\alpha_o = \alpha_1 + \alpha_2 \cdot \frac{\tau_o \cdot \rho_3}{1 - \rho_2 \cdot \rho_3} \tag{C.37}$$

$$\alpha_i = \alpha_3 \cdot \frac{\tau_o}{1 - \rho_2 \cdot \rho_3} \tag{C.38}$$

Finally, to find the absorbed solar radiation in each glazing layer, the following equations may be determined:

$$S_{\alpha o} = \alpha_o \cdot S_t \tag{C.39}$$

$$S_{\alpha i} = \alpha_i \cdot S_t \tag{C.40}$$

C.4. Radiosity Equations

This section describes the equations used for calculating the view factors between the window, floor, wall, and ceiling surfaces in the test cells at the FBL. In figure (C.2a) you may find the view factor between parallel surfaces and in figure (C.2b) you may find the view factor between adjacent perpendicular surfaces.

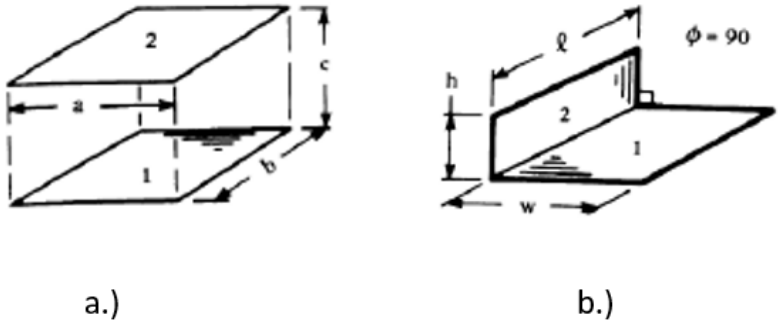

Figure C.2. Configurations for View Factors between surfaces.

We let $X = a/c$ and $Y = b/c$ for configuration (a), or equation (C.41), and $H = h/l$ and $W = w/l$ for configuration (b), or equation (C.42):

$$F_{1-2} = \frac{2}{\pi XY} \cdot \begin{bmatrix} ln\left[\frac{(1+X^2)\cdot(1+Y^2)}{1+X^2+Y^2}\right]^{1/2} - X\,tan^{-1}(X) - Y tan^{-1}(Y) \ldots \\ + X\sqrt{1+Y^2}\cdot tan^{-1}\cdot\left(\frac{X}{\sqrt{1+Y^2}}\right) + Y\sqrt{1+X^2}\cdot tan^{-1}\cdot\left(\frac{Y}{\sqrt{1+X^2}}\right) \end{bmatrix} \quad \text{(C.41)}$$

$$F_{1-2} = \frac{1}{\pi W} \cdot \begin{bmatrix} W tan^{-1}\left(\frac{1}{W}\right) - \sqrt{H^2+W^2}tan^{-1}(H^2+W^2)^{-\frac{1}{2}} + H tan^{-1}\left(\frac{1}{H}\right) \ldots \\ + \frac{1}{4} ln\left[\left[\frac{(1+W^2)(1+H^2)}{1+W^2+H^2}\right]\left[\frac{(1+W^2+H^2)(W^2)}{(1+W^2)(H^2+W^2)}\right]^{W^2}\left[\frac{(1+W^2+H^2)(H^2)}{(1+H^2)(H^2+W^2)}\right]^{H^2}\right] \end{bmatrix} \quad \text{(C.42)}$$

C.5. View Fraction with Results

To calculate the view to the outdoors we can use the method from Tzempelikos (2008). The height of the vertical projection of each slat surface on the vertical plane is found with:

$$S(\beta) = L \cdot \sin(\beta) + \delta \cdot cos(\beta) \quad \text{(C.43)}$$

L is the length of the blind slat, δ is the thickness of the blind slat, and β is the blind tilt angle. The projected shading fraction, F_b, is calculated by the following equation:

$$F_b = \frac{S(\beta)}{L} = \sin(\beta) + \frac{\delta}{L} \cdot cos(\beta) \quad \text{(C.44)}$$

The total projected window area shaded by the blinds, A_b, is found with:

$$A_b = A_{win} \cdot \frac{S(\beta)}{L} \quad \text{(C.45)}$$

A_{win} is the area of the window. To find the projected view of the opening, F_g, and the equivalent projected open area, A_g:

$$F_g = 1 - \frac{S(\beta)}{L} \tag{C.46}$$

$$A_g = A_{win} \cdot \left(1 - \frac{S(\beta)}{L}\right) \tag{C.47}$$

To calculate the projected open area and fraction based on the packing factor of the STPV window, we can use the following equations:

$$F_{STPV-bl} = \left(1 - \frac{A_{PV}}{A_{win}}\right) \cdot \left(1 - \frac{S(\beta)}{L}\right) \tag{C.48}$$

$$A_{STPV-bl} = A_{win} \cdot \left(1 - \frac{A_{PV}}{A_{win}}\right) \cdot \left(1 - \frac{S(\beta)}{L}\right) \tag{C.49}$$

The term $\left(1 - \frac{A_{PV}}{A_{win}}\right)$ equates to the packing factor of the window and A_{PV} is the total area of the PV cells. At the FBL the center section of the window is a clear glazing with an installed roller shade on the interior, therefore, an effective view fraction can be calculated with all three window sections. The effective view fraction can be found with:

$$F_{eff} = \left(\frac{2}{3}\right) \cdot F_{STPV-bl} + \left(\frac{1}{3}\right) \cdot F_{rs} \tag{C.50}$$

F_{eff} is the effective view fraction and F_{rs} is the view fraction from the roller shade section. $F_{rs} = 1$ when the shade is fully open and $F_{rs} = 0$ when the shade is fully closed. Figure (C.3) below shows the percentage of window which is shaded and the percentage of view to the outdoors at different blind tilt angles for both an open and closed roller shade. The subscript ‘o’ stands for an open roller shade while the subscript ‘c’ stands for a closed roller shade.

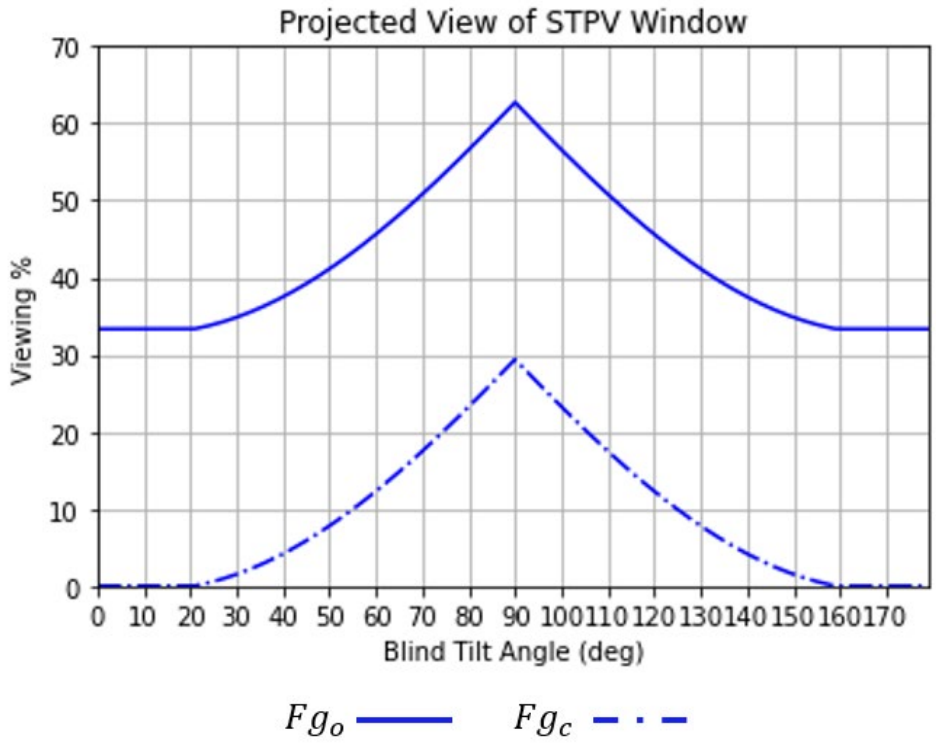

Figure C.3. Projected Shading & Viewing Percentage of Façade in Test Cell 4 at different blind tilt angles for open and closed roller shade.

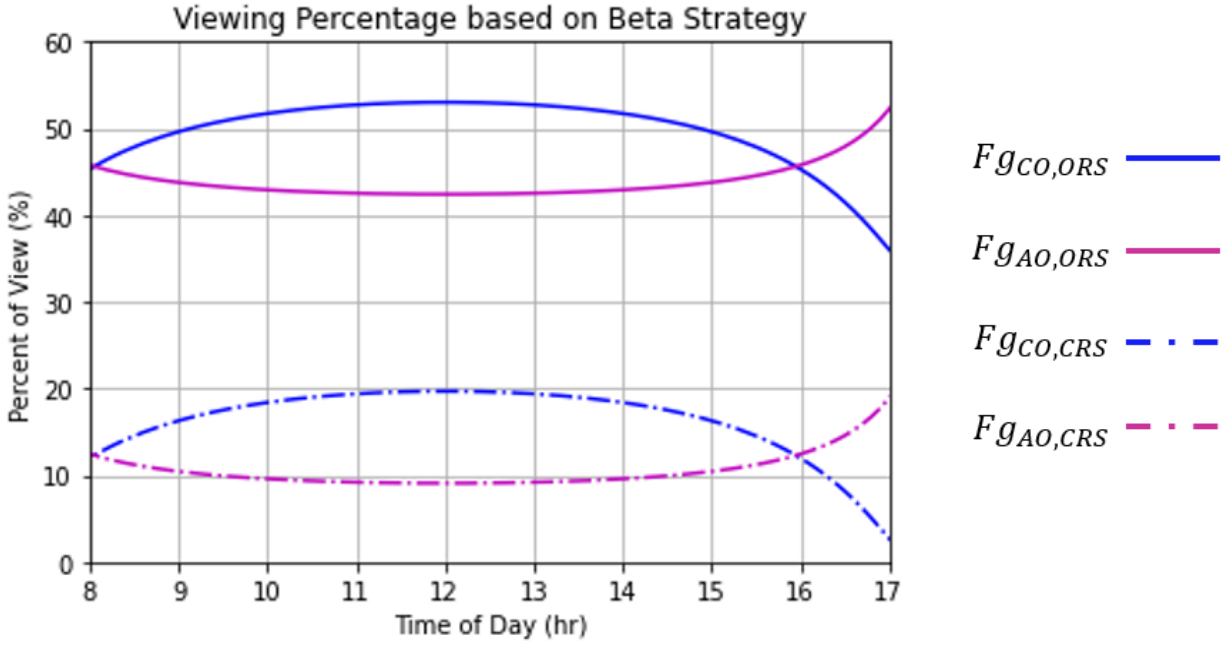

Figure C.4. View based on Two Blind Tilt Angle Strategies with Open and Closed Roller Shade.

Figure (C.4) shows the percentage of projected view for the STPV window based on the cut off and always open blind tilt angles strategies throughout the typical workday. The solid curves represent the viewing percentage when the roller shade is open in the viewing section and the dashed curves represent the viewing percentage when the roller shade is closed.

C.6. New Daylight Glare Index Results

Visual comfort tests were completed separately from the workplane illuminance tests due to sensor availability. Using the method proposed by Nazzal (2005) the 'new' daylight glare index can be calculated experimentally using three vertical photometers. Equations (3.35) through (3.42) are used for this analysis. The following figure shows the glare index and exterior illuminance versus the incidence angle on March 19th, 2023.

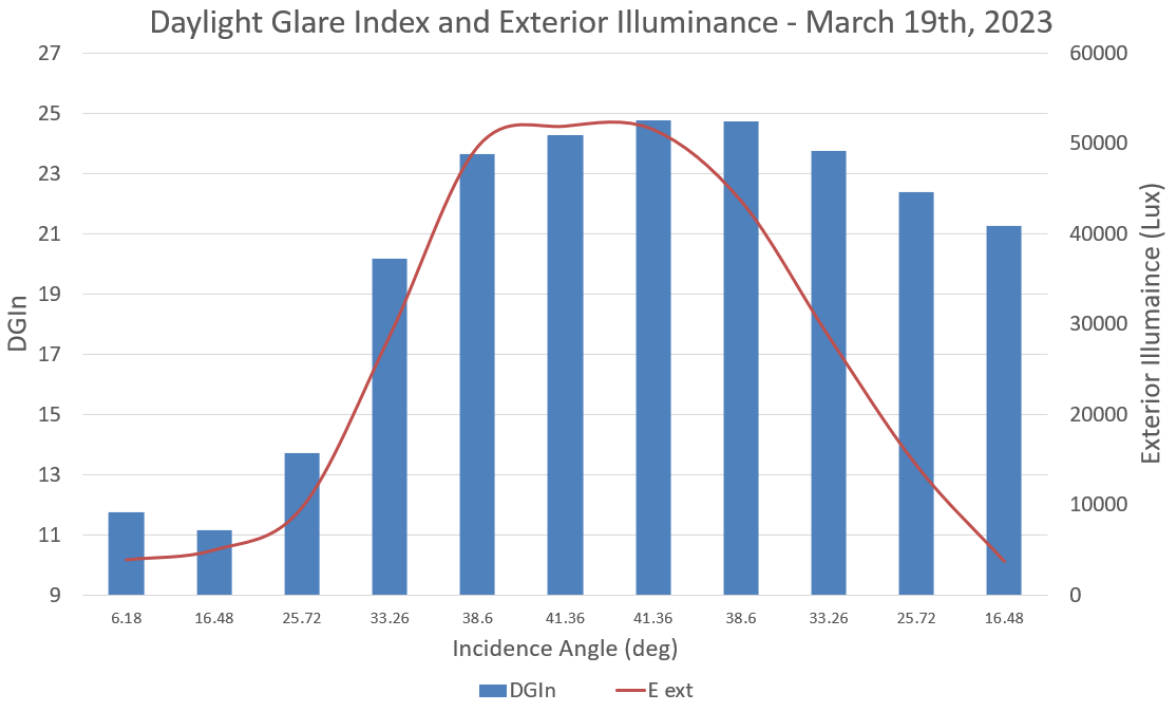

Figure C.5. New Daylight Glare Index and Exterior Illuminance versus the Incidence Angle. March 19th, 2023.

The following table from chapter 2 is repeated for clarity, which is the glare perception scale based on the DGI value:

Table C.2. Glare Perception Scale with Daylight Glare Index.

DGI	Glare Criterion	DGI	Glare Criterion	DGI	Glare Criterion
<16	Imperceptible	**20**	Just Acceptable	**26**	Uncomfortable
16	Just Perceptible	**22**	Acceptable	**28**	Just intolerable
18	Perceptible	**24**	Just Uncomfortable	**>28**	Intolerable

These results show that the morning was semi-cloudy, having a slightly lower exterior illuminance, compared to its counterpart incidence angle about solar noon. This had provided a lower DGI_n in the morning, but clearer conditions with low incidence angles in the evening provided higher glare indices. The glare index maintained 'Just Uncomfortable' levels from 12-4PM; in this case shading may be adjusted to improve the occupants' sense of glare. Since this method tests for the 'worst-case' scenario, facing the window and no artificial lighting, the occupant may turn 90 degrees and activate artificial lighting to reduce the glare perception.

C.7. STPV Results

The effect of the STPV window on the BEFI is much greater on clear days and closer to the shoulder seasons. Similarly shown in figure (C.5) is the energy generation on a clear day from testing on February 4th.

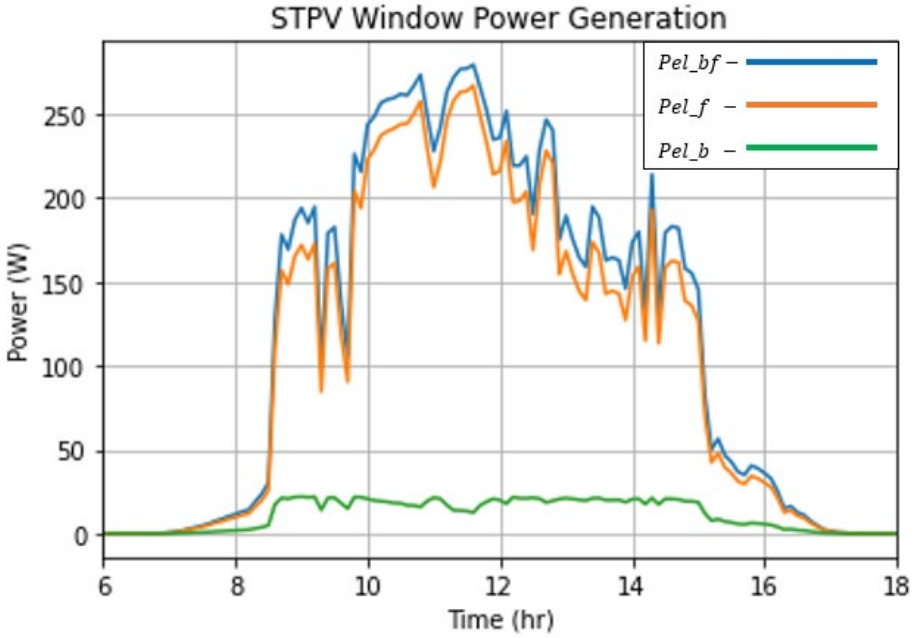

Figure C.6. Power Production from STPV Window on Clear Day – February 4th, 2023.

The daily PV production was simulated to be 1.44 kWh ($0.813\ \mathrm{kWh/m^2}$) for test cell 4. On the February 4th clear day experiment and simulation, the morning peak period resulted in 82.3 Wh of power generation while the evening peak showed 16.4 Wh of power generation. The average increase for clear and cloudy days for different days of the heating season was simulated and shown in table (C.3).

Table C.3. Daily and peak demand period energy generation of bifacial STPV window for different months of the heating season.

Month	Clearness	Daily (kWh)	Daily (kWh/m2)	Increase mono-bi (%)	6-9AM (kWh)	4-8PM (kWh)
Dec. 21st	Cloudy	0.09	0.05	17.0	$3.68 \cdot 10^{-3}$	$1.85 \cdot 10^{-4}$
	Clear	0.62	0.35	15.8	$2.52 \cdot 10^{-2}$	$1.29 \cdot 10^{-3}$
Jan. 13th	Cloudy	0.11	0.06	16.9	$5.14 \cdot 10^{-3}$	$4.67 \cdot 10^{-4}$
	Clear	0.70	0.40	15.1	$3.01 \cdot 10^{-2}$	$2.77 \cdot 10^{-3}$
Feb. 4th	Cloudy	0.25	0.14	16.7	$1.30 \cdot 10^{-2}$	$2.38 \cdot 10^{-3}$
	Clear*	1.44	0.81	13.1	$8.23 \cdot 10^{-2}$	$1.64 \cdot 10^{-2}$
Mar. 2nd	Cloudy*	0.24	0.14	16.6	$9.14 \cdot 10^{-3}$	$2.20 \cdot 10^{-2}$
	Clear	1.27	0.72	14.2	$1.30 \cdot 10^{-2}$	$4.84 \cdot 10^{-2}$

** Real solar radiation data rather than Hottel's Model.*

C.8. Overheating

The following figure shows the potential for overheating when no shading is applied in perimeter zones on clear days. Beji et al. (2020) studied different durations of direct solar radiation on TAB systems and found that above 2 hours of direct solar radiation there is high potential for overheating and thermal discomfort. In figure (C.7) is test cell 4 at the FBL simulated with no shading on a clear and very cold day. High temperature swings are seen, and air temperatures exceed 25 °C for most of the workday. Similarly, the floor surface temperature exceeds that maximum of 29 °C after 10:30 AM for the remainder of the workday. The operative temperature fell within the PMV boundaries of ±1 for only 26.7% of the day.

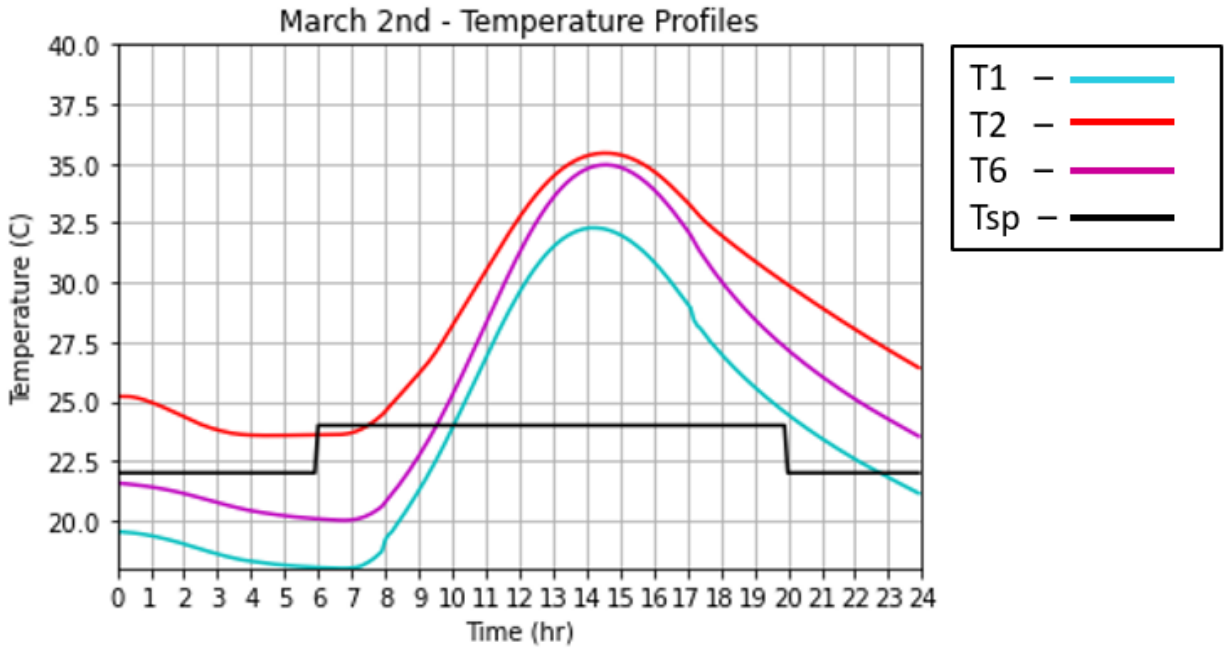

Figure C.7. Overheating due to lack of shading.

Appendix D: Material Properties and Conversions

D.1. Materials

To determine the properties of the concrete for the simulation model we needed to obtain the density, which was assumed to be 1995 $\mathrm{kg/m^3}$, as it is lightweight concrete. This allowed the calculation of the thermal conductivity (k_c) and specific heat capacity (C_p) using the correlations from Zhou & Brooks (2019) and ACI-122 (2002). These resulting values from these correlations are in Table (F.2).

$$k_c = 0.072 \cdot e^{0.00125 \cdot \rho_{con}} \left(\frac{W}{m \cdot K}\right) \tag{D.1}$$

$$C_v = 0.897 \cdot \rho_{con} + 32.58 \left(\frac{kJ}{m^3 K}\right) \tag{D.2}$$

$$C_p = \frac{C_v}{\rho_{con}} \cdot 1000 \frac{J}{kJ} \left(\frac{J}{kg \cdot K}\right) \tag{D.3}$$

Table D.1. Properties of Building materials at the FBL.

Material	Thermal Conductivity (W/mK)	Specific Heat Capacity (kJ/kgK)	Density (kg/m^3)	Length (cm)	Thermal Resistance (RSI)
Gypsum Board	0.16	0.750	800	-	-
Expanded Polystyrene Floor Insulation	0.031-0.038*	1.5*	15-28*	8.89**	1.77**
Concrete	0.872	0.913	1995**	10.16	-
Glass	1	0.84	2.5 (kg/m^2/mm)	-	-
PV Cell	149	0.703	2330	-	-
PEX Pipe	0.41	2.10	0.950	-	-
Copper Pipe	398	0.39	8960	-	-

**Yucel et al., 2003.*
***Manufacturer.*

Table D.2. Properties of Polycrystalline PV cells for Test Cell 4 at the FBL.

Parameter		Methodology	Range
Electrical Efficiency	η_{ref}	0.18	0.062 to 0.221
Temp. Coefficient at Max Power Point	$\mu_{P,mp}$ (%/C)	-0.456	-0.679 to -0.343
-		ASHRAE, 2019	-
Double Glazed BIPV Window	a $(-)$	-2.85	-
	b (s/m)	-0.0351	
	dT (K)	9	
Triple Glazed BIPV Window	a $(-)$	-2.88	
	b (s/m)	-0.0319	
	dT (K)	11	

D.2. Fluids

Table D.3. Fluid Properties of Air and Water for relevant temperatures.

Fluid	Specific Heat Capacity		Density
	kJ/kgK (°C)		kg/m^3 (°C)
Air	1.006	(15)	1.23 (15)
		(25)	1.185 (25)
		(30)	1.165 (30)
Water	4.184 (25)		997.13 (25)
	4.180 (43)		991.05 (43)

D.3. Conversions

Table D.4. Conversions from Imperial to Metric Units.

Parameter	Imperial	Metric	
Flow rate	1 gpm	0.063 kg/s	
Length	1 inch	0.0254 m	
	1 ft	0.304 m	
Area	1 ft^2	0.0929 m^2	
Volume	1 ft^3	0.0283 m^3	
Energy	1 btu	0.293 Wh	1055.6 J
Power	1 hp	745.7 W	
Heat transfer coefficient	1 $\mathrm{btu/(h \cdot ft^2 \cdot °F)}$	5.678 $W/(m^2 \cdot K)$	
Thermal Resistance	1 R	0.1761 RSI	
Temperature	$T(F)$	$T(°C) = (T(°F) - 32) * (5/9)$	
		$T(K) = T(°C) + 273.15$	
Illuminance	1 fc	10.76 Lux	
Pressure	1 psi	6.89 kPa	
	14.696 psi	1 atm	101.325 kPa

- The conversion of daylight to irradiance is 0.0926 ($W/m^2/Lux$; Michael et al., 2020).

Appendix E: Uncertainty of Measurements

Table E.1. Sensors and their Accuracy.

Sensor	Name/model		Accuracy
Thermocouple	Type T		±0.5 °C to ± 1 °C
Thermostat	Watts Tekmar 563		±0.2 °C @ 25 °C
Relative Humidity	Vaisala HMD83D		3% (0-90% RH)
			±0.3 °C @ 20 °C
Flow Rate	Belimo 22PE-5UD		2.22% (1.00 gpm)
			2.14% (1.50 gpm)
			2.09% (2.50 gpm)
-	Model	Calibration	-
Pyranometer	Li-Cor – 200R	-94.76 $W/m^2/mV$	1% (<3000 W/m^2)
		-94.54 $W/m^2/mV$	
Photometer	Li-Cor – 210R	-6.13 kLux/mV	1% (<100 kLux)

General form of uncertainty:

$$\sigma_f = \sqrt{\left(\frac{\partial f}{\partial_{x1}}\right)^2 \cdot \sigma_{x1}^2 + \left(\frac{\partial f}{\partial_{x2}}\right)^2 \cdot \sigma_{x1}^2 + \cdots + \left(\frac{\partial f}{\partial_{xn}}\right)^2 \cdot \sigma_{xn}^2}$$

Uncertainty of heat from hydronic system, the uncertainty of thermocouples is 0.5 °C.

$$\sigma_{\Delta T} = \sqrt{0.5^2 + 0.5^2} = 0.71℃$$

$$\sigma_{Q_{water}} = \sqrt{\left(\dot{m} \cdot C_p \cdot \sigma_{\Delta T}\right)^2 + \left((\Delta T) \cdot C_p \cdot \sigma_{\dot{m}}\right)^2}$$

Uncertainty of Plane Radiant Temperature:

$$\sigma_{Tpr} = \sqrt{0.5^2 + 0.5^2 + 0.5^2 + 0.5^2 + 0.5^2 + 0.5^2} = 1.22\ ℃$$

Uncertainty of Operative Temperature while using the measurements of the Vaisala HMD83D is 0.3 °C:

$$\sigma_{Top} = \sqrt{0.3^2 + {\sigma_{Tpr}}^2} = 1.26\ ℃$$

E.1. Heating Load

The measured heating load was difficult to obtain as there were software issues involved with connecting to the Belimo thermal energy meter. Belimo has an online application for the relevant data with the floor heating system. The flow rate, inlet and outlet temperatures, and applied heating data is collected and plotted. Without connection to the application, the auxiliary heating was calculated with thermocouples applied to the inlet and outlet on the copper pipes and the flow rate provided through the NFC of the Belimo meter.

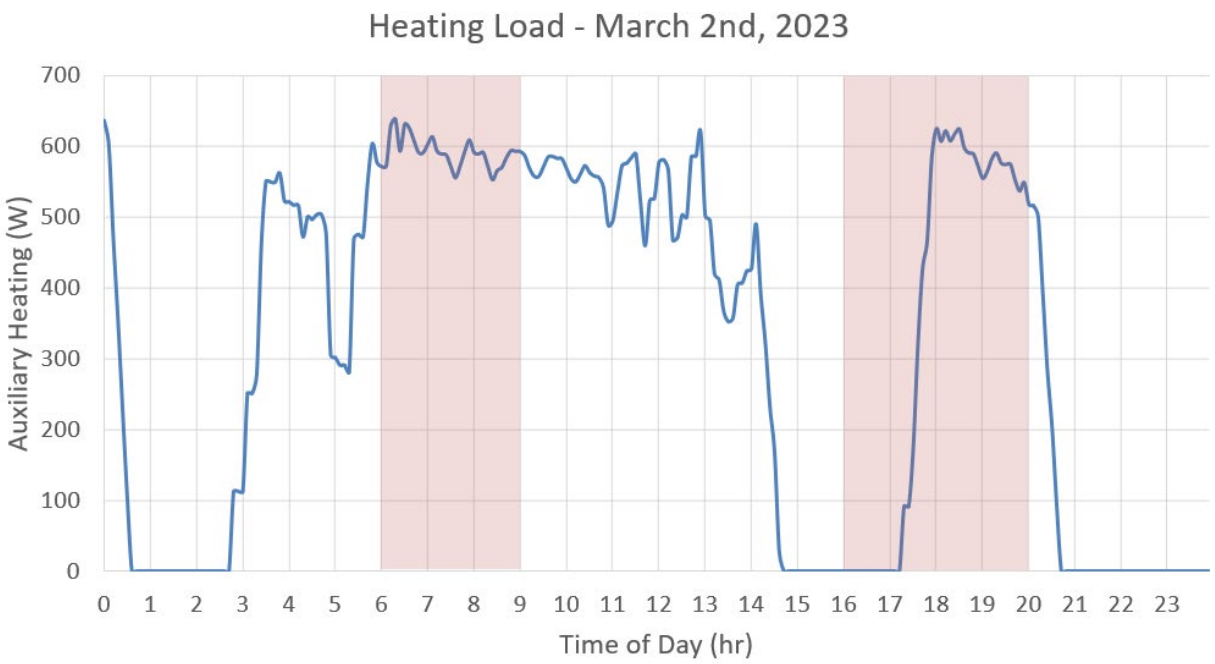

Figure E.1. Measured Heating Load.

Figure (E.1) shows the daily measured heating load and the peak demand periods are highlighted. This curve was developed using equation (3.1). It was assumed that there was no flow when the temperature reading at the pipe-slab junction was below 33 °C, which was based on the sharp decrease seen in temperature after these readings. A 5-point rolling average of the auxiliary heating calculations was completed to compensate for data fluctuations. Figure (E.2) gives a visual of the flow rate and heating assumption.

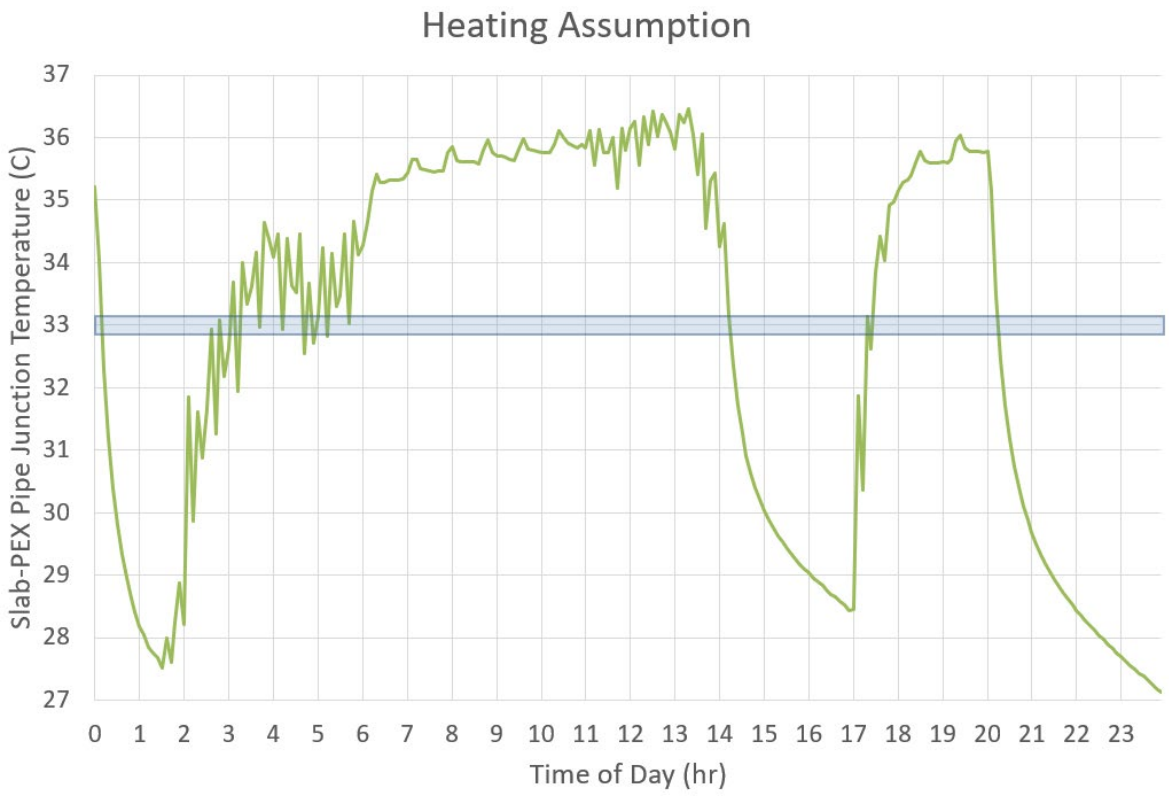

Figure E.2. Assumption of flow rate for heating calculations.

Appendix F: Installation of Floor Heating System

F.1. Simulation Study of Slab Thickness

Preliminary simulations were completed to evaluate four different concrete slab thicknesses and their effect on energy performance and thermal comfort. The four slab thicknesses considered were 5, 8, 10, and 12 cm. Three WWRs were considered at 16, 32, and 48%. These parameters were subjected to setpoint strategies described in Appendix (B) for a very cold and clear day. The reference case in these simulations was a setpoint of 23 °C. Figure (F.1) shows the setpoints used for this simulation study.

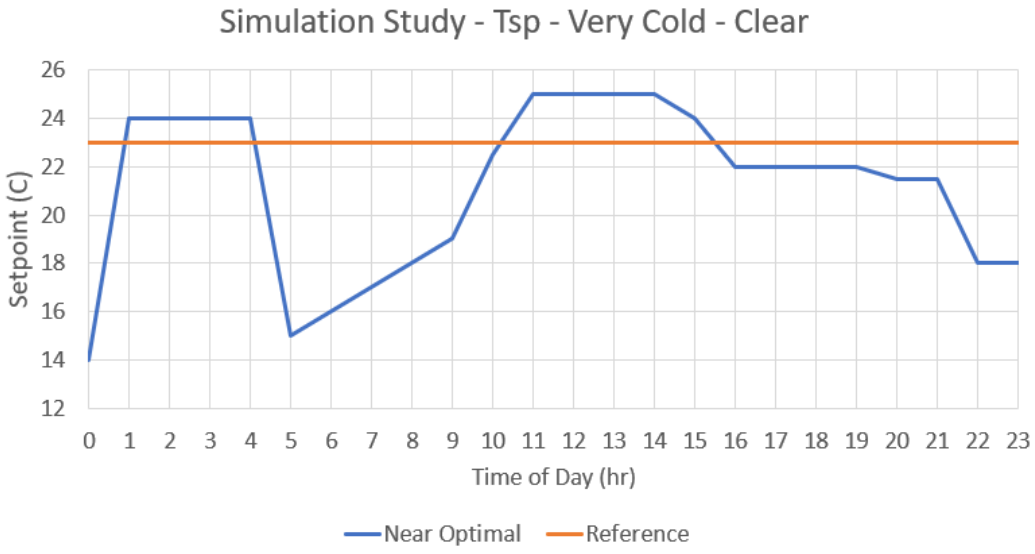

Figure F.1. Temperature setpoint strategies used for simulation study.

The final decision for the installations were based on performance of energy flexibility. A 10.16 cm (4") slab was installed in test cell 4 of the FBL and a 7.62 cm (3") slab was installed in test cell 3.

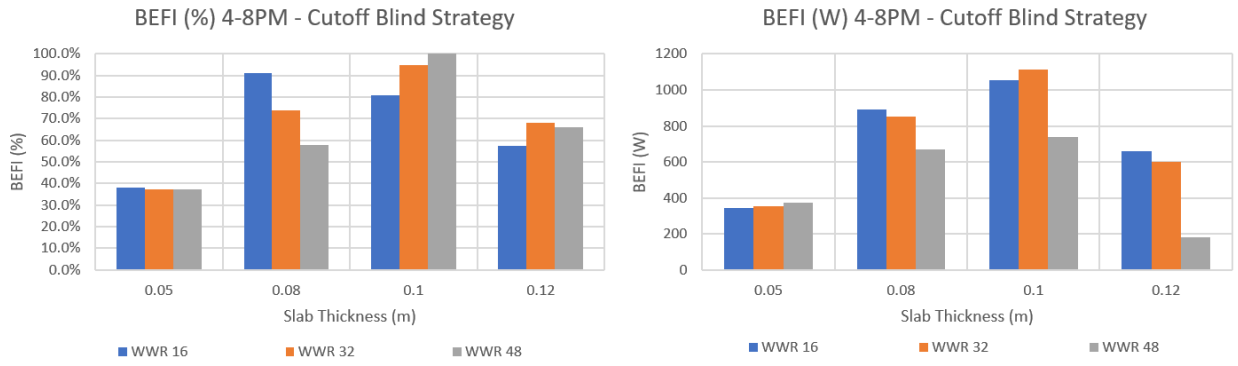

Figure F.2. Parametric Simulation study of different slab thicknesses and WWR and their effect on the BEFI. (Hill & Athienitis, 2023).

F.2. Installation Procedure

The following figures F.1–F.4. show the process of installing a hydronic radiant floor heating system. The installation totalled 6 working days beginning in late-August of 2022 and took over a

month-and-a-half period to complete. After the concrete is poured, 28 days are needed to allow the concrete to cure, therefore, the system setup and connection to the Hot Water Heat Pump was completed in mid-October. Two slabs were installed in two different test cells with different slab thicknesses, 3” (7.62 cm) in Test Cell 3, and 4” (10.16 cm) in Test Cell 4.

Initially, floor insulation was applied in two different test cells, shown below in figure (F.3a). The floor insulation used is ISORAD V2 160 with a thickness of 3 ½” (8.89 cm) and an RSI value of 1.77. In figures (F.3b-d) the PEX hydronic piping, of exterior diameter 5/8” (1.59 cm), is shown in a serpentine pattern. Mounting poles were created to allow thermocouples to be positioned at different depths throughout the slab, shown in figure (F.3c). In figure (F.3d) the PEX pipes are shown at the exit point of the slab, for connection to the hot water heat pump.

Figure F.3. Installation of a.) Floor Insulation, b.) PEX hydronic pipes, c.) Thermocouples for in-slab temperature response, d.) Piping exit from slab.

After two days of installing the floor insulation and PEX pipes, the concrete was able to be poured, shown in Figure (F.4a). The concrete finish is shown in figure (F.4b) at thicknesses of 3” (7.62 cm) in test cell 3 and 4” (10.16 cm) in test cell 4. The concrete had to dry for at least two days and is shown in figure (F.4c).

a.) b.) c.)

Figure F.3. Installation of concrete slab a.) concrete pouring, b.) concrete drying, c.) dried concrete (2 days after pouring).

Figure (F.6) shows the copper piping and connection to the hydronic modules. Shown in figure (F.6a) is the Rheem tank, mixing valve, and its connection to the water pumps. The supply water from the tank is mixed with the cooler return water from the hydronic floor system. The mixing valve is shown in figure (F.6b). The supply and return section to the hydronic floor is shown in (F.6c).

a.) b.) c.)

Figure F.4. a.) Piping connection to Water Heater with water pumps, b.) Hot/Cold water mixing, c.) Connection to Hydronic Modules and copper piping at slab exit.

The hydronic system has an attached thermal energy meter from Belimo, which can measure the flow rate of the water, the temperature difference between the supply and return points, and the power required for the system. This energy meter is not a consumer-based product and requires the alteration of the computer IP address to view the online program. The TAB system has programmable thermostats in each test cell to allow for isolated control, shown in figure (F.6c). Schedules, or T_{sp} strategies, can be programmed for each day of the week and can be updated via a mobile application, 'Watts Home'.

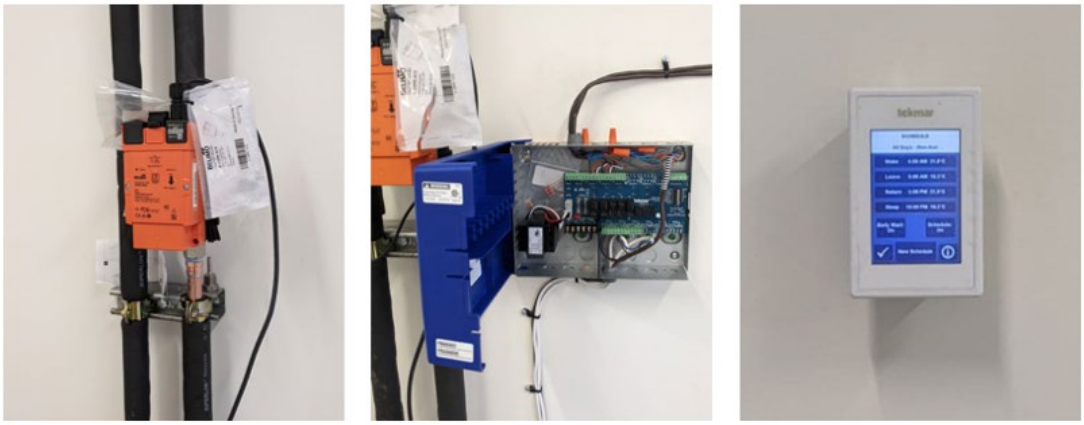

Figure F.6. a.) Thermal Meter, b.) Zone Control, c.) Thermostat.